

Particle Transport in JET and TCV H-Mode Plasmas

THÈSE N° 4450 (2009)

PRÉSENTÉE LE 30 OCTOBRE 2009
À LA FACULTÉ SCIENCES DE BASE
CRPP ASSOCIATION EURATOM
PROGRAMME DOCTORAL EN PHYSIQUE

ÉCOLE POLYTECHNIQUE FÉDÉRALE DE LAUSANNE

POUR L'OBTENTION DU GRADE DE DOCTEUR ÈS SCIENCES

PAR

Mikhail MASLOV

acceptée sur proposition du jury:

Prof. O. Schneider, président du jury
Dr H. Weisen, directeur de thèse
Dr C. Bourdelle, rapporteur
Dr P. Mantica, rapporteur
Dr O. Sauter, rapporteur



ÉCOLE POLYTECHNIQUE
FÉDÉRALE DE LAUSANNE

Suisse
2009

Version abrégée

La compréhension de la physique du transport des particules est d'une grande importance pour le confinement magnétique du plasma et des projets de développement de la fusion nucléaire pour la production d'énergie. Dès les débuts de cette discipline, il y a plus d'un demi-siècle, le problème du transport de la chaleur dans les tokamaks a attiré l'attention des chercheurs. Les phénomènes de transport de particules, cependant, ont été assez largement négligés jusqu'à récemment. A mesure que la compréhension de la physique des tokamaks a progressé, les physiciens se sont rendu compte que le confinement de l'énergie n'est pas le seul problème critique de la fusion contrôlée. Le sujet de cette thèse, le transport des particules dans les plasmas chauds et magnétisés, fait partie de ces questions ouvertes, à laquelle la communauté de la recherche en fusion s'efforce de trouver des réponses.

L'objectif de ce travail de thèse est d'étudier le transport anormal (turbulent) des particules sur la base d'expériences effectuées sur deux installations différentes, JET (Joint European Torus) et TCV (Tokamak à Configuration Variable). Ce travail s'intéresse tout particulièrement aux phénomènes de transport convectifs, qui permettent l'établissement de gradients de densité en l'absence de sources de particules au sein du plasma et qui conduisent à des profils de densité 'piqués', c.à.d. de densité plus élevés au centre qu'au bord du plasma. Le 'piquage' de la densité aura un effet favorable (toutes autres grandeurs étant constantes) pour la production de puissance nucléaire de fusion dans un futur réacteur. Pour cette raison, nous proposons également une extrapolation pour les conditions du futur réacteur nucléaire expérimental international ITER, actuellement en cours de construction en France.

La thèse comporte une partie expérimentale et une partie théorique, à la suite de laquelle les prédictions d'un modèle gyrocinétique sont comparées à l'expérience. Une base de données expérimentale a été créée sur la base des recherches menées sur JET et TCV au cours des ces dernières années, pour des plasmas en mode de confinement amélioré (mode H). La partie expérimentale s'appuie sur les données les plus récentes, récoltées au cours de la thèse et analysées au moyen de méthodes améliorées. Ce travail a ainsi permis de dissiper des doutes ayant pu subsister sur le traitement des données effectué précédemment. Il nous a permis d'établir les dépendances entre les profils de densité et certains paramètres importants du

plasma. Les conclusions principales obtenues précédemment sur le JET et d'autres tokamaks ont généralement été confirmées, avec quelques suppléments

La principale nouveauté de la thèse consiste en des comparaisons systématiques des observations avec des simulations gyrocinétiques linéaires, au moyen du code GS2, du transport induit par une onde de dérive instable, l'ITG (Ion Temperature Gradient), qui semble être l'instabilité principale dans les plasma aux conditions prévalentes dans les plasmas étudiés. Les dépendances des gradient de densité du plasma, observées sur le JET, sont un bon accord avec celles de la simulation sur une large plage de paramètres physiques, ce qui permet de valider cet aspect particulier de la théorie gyrocinétique, qui est actuellement la théorie standard pour expliquer le transport dans les tokamaks. Les simulations réalisées pour le TCV sont en accord partiel avec l'expérience, qui se situe dans un autre domaine paramétrique que JET. Un accord plus complet n'est pas exclu cependant, mais devrait faire appel à une étude plus approfondie que possible dans le cadre de cette thèse et surtout à des mesures non disponibles actuellement sur TCV.

Le bon accord entre l'expérience et les simulations sur JET suggère que l'instabilité ITG est responsable de la majorité de la convection anormale des particules vers l'intérieur, observée dans les tokamaks. Les simulations et les données empiriques permettent d'anticiper un profil piqué de densité dans le plasma d'ITER, au lieu d'un profil plat, comme prévu lors de la conception du projet.

Les mots clés: fusion nucléaire, tokamak, transport des particules, simulations gyrocinétiques linéaires.

Abstract

Understanding particle transport physics is of great importance for magnetically confined plasma devices and for the development of thermonuclear fusion power for energy production. From the beginnings of fusion research, more than half a century ago, the problem of heat transport in tokamaks attracted the attention of researchers, but the particle transport phenomena were largely neglected until fairly recently. As tokamak physics advanced to its present level, the physics community realized that there are many hurdles to the development of fusion power beyond the energy confinement. Particle transport is one of the outstanding issues.

The aim of this thesis work is to study the anomalous (turbulence driven) particle transport in tokamaks on the basis of experiments on two different devices: JET (Joint European Torus) and TCV (Tokamak à Configuration Variable). In particular the physics of particle inward convection (pinch), which causes formation of peaked density profiles, is addressed in this work. Density profile peaking has a direct, favorable effect on fusion power in a reactor, we therefore also propose an extrapolation to the international experimental reactor ITER, which is currently under construction.

To complete the thesis research, a comprehensive experimental database was created on the basis of data collected from on JET and TCV during the duration of the thesis. Improvements of the density profile measurements techniques and careful analysis of the experimental data allowed us to derive the dependencies of density profile shape on the relevant plasma parameters. These improved techniques also allowed us to dispel any doubts that had been voiced about previous results. The major conclusions from previous work on JET and other tokamaks were generally confirmed, with some minor supplements.

The main novelty of the thesis resides in systematic tests of the predictions of linear gyrokinetic simulations of the ITG (Ion Temperature Gradient) mode against the experimental observations. The simulations were performed with the GS2 code. The parameter dependencies of plasma density gradient, as observed on JET, are in a good agreement with those from the simulations over a wide range. The simulations done for the TCV case, which are in a different physics parameter domain, are also in partial agreement with the experiment. Complete agreement is not out of the question, but will remain a goal for the future, when measurements of one of the most important parameters will be available.

The good agreement between the experiment and the simulations suggests that the ITG instability may be responsible for the majority of the anomalous inward particle convection observed in tokamaks. Both the simulations and the empirical data extrapolations predicting a peaked density profile in ITER plasma conditions, instead of a flat one, as was assumed during the concept design period.

Keywords: nuclear fusion, tokamak, particle transport, linear gyrokinetic simulations.

Contents

1. Introduction	1
1.1 Global energy production	1
1.2 The basic principles of fusion power generation	2
1.3 Tokamak	4
1.4 Particle confinement	5
1.5 Outline of the thesis	8
2. Density profile measurements	11
2.1 Introduction	11
2.2 The Thomson scattering diagnostic	11
2.3 Far Infrared interferometry	14
2.4 Inversion techniques	16
2.4.1 The “least regularized” inversion	20
2.5 Consistency in density profile measurements from the LIDAR and the FIR diagnostics on JET	23
3. Experimental data analysis on JET	29
3.1 Introduction	29
3.2 The JET tokamak	30
3.3 JET 2006-2007 experiments and H-mode plasma database	32
3.4 Experimental data analysis	35
3.5 Conclusions and summary	43
4. Plasma microturbulence and linear gyrokinetic simulations	45
4.1 Introduction	45
4.2 Microinstabilities	45
4.3 Gyrokinetics and the GS2 code	49
4.4 Linear simulations for the JET H-mode plasma conditions	51
4.5 Local shear dependence and comparison with the experiments	59

4.6 Summary and discussion	61
5. ECRH heated H-mode experiments on the TCV tokamak	65
5.1 The TCV tokamak	65
5.2 TCV diagnostics	67
5.3 Third harmonic ECRH heated H-mode experiments on TCV	70
6. Overall summary and discussions	81

CHAPTER 1

Introduction

1.1 Global energy production.

As a consequence of rising standards of living in many parts of the world and population growth, the global demand for energy is increasing. Currently the major part of the energy production is from non-renewable fossil fuels (natural gas, oil, coal). Although relatively cheap and simple in production, fossil fuels do not offer an acceptable long term perspective due to inevitable resource depletion and a negative environmental impact, notably resulting from their greenhouse gas emissions.

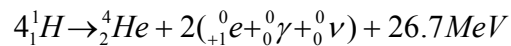
Sooner or later mankind will have to resort to alternative energy sources. Nuclear power from fission reactions may see a renaissance in the medium term, because of essentially negligible greenhouse emissions and potentially very long lasting reserves (assuming the use of breeding technologies) compared to traditional power plants. However fission power still remains controversial because of the risk of an uncontrolled chain reaction resulting in a catastrophic reactor core meltdown and a possible explosion with a subsequent emission of radioactivity into the environment, as well as because of the necessity of long term (tens of thousands years) safe storage of radioactive waste.

Fusion power produced in confined high temperature plasmas offers a potentially attractive alternative because it uses deuterium and lithium as primary fuels, does not produce large amounts of long-lived radioactive waste and has a high degree of inherent safety because of the absence of chain reactions.

Unfortunately, fusion power production in a reliable, controllable and commercially profitable way is a very difficult, as yet unsolved technical problem. Very significant progress has however been achieved in the past 50 years, starting from small, essentially table-top plasma experiments to large machines like the JET tokamak, where a 16 MW release of fusion power was measured in 1996. The next step in this endeavour is the international ITER project currently under construction in France, intended to prove the technical feasibility of fusion power production in a device comparable in size and plasma parameters to that required of a future commercial reactor.

1.2 The basic principles of fusion power generation

Merging of light nuclei into a heavier one is called a nuclear fusion reaction. That is the inverse process of nuclear fission, the driving mechanism for nuclear power plants. Many fusion reactions of low Z number elements are exothermal, i.e. they produce energy. The most abundant in the universe, the proton-proton chain reaction, provides the main source of energy to power the sun and other stars:



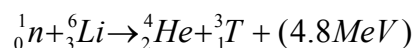
This reaction unfortunately is impossible to achieve on Earth due to its extremely low effective cross-section.

For power generation the reaction between heavier hydrogen isotopes: ^2_1D and ^3_1T is currently considered due to its relatively large cross section at moderate energies:



Deuterium is a stable isotope and can be extracted from water. The content of D among light hydrogen atoms is very low: 0.008% in average, but just one gram of it (extracted from about 100 liters of water) can be used to produce of $1.7 \cdot 10^{12}$ J of heat, which is equivalent to burning of 3.8 tons of gasoline.

Tritium has a half-life time of 12.8 years and therefore does not exist in nature. The only way to produce it for fusion power generation is to breed it directly in the reactor, using fast neutrons from D-T reactions:



Deuterium and Lithium are hence the primary fuels for a fusion reactor. They are both sufficiently abundant on our planet and can be relatively unexpensively extracted from water and from mineral salt deposits.

The main problem for developing a reactor is that for fusion reactions to occur, the repulsive Coulomb force between the positively charged reactants must be overcome by providing them with a very significant energy. To reach the maximum of the thermonuclear fusion reaction rate, a D-T mixture must be heated up to ~ 60 keV. At the temperatures of ~ 10 keV (about 116,000,000°K), the reaction rate drops by nearly order of magnitude. At such temperatures these gases, as well as all light elements, are completely ionized, i.e. they are in the plasma state.

Due to the extreme temperatures, interaction of the D-T plasma with the container walls has to be minimized. The concept of magnetic confinement is based on the fact that plasmas ability to move across magnetic field lines is very limited, thus it can be to some extent restricted to a certain volume, defined by the magnetic field configuration. There are many different types of magnetic confinement devices, such as tokamaks [1-3], stellarators [4, 5], magnetic mirrors (open traps)[6], reversed field pinches[7].

Credibility of a magnetic confinement device for the fusion power generation can be estimated by so-called Lawson criteria [8](derived by J. D. Lawson in 1955). It describes the condition where the energy produced by D-T fusion reactions exceeds the losses from the system, so the power generation becomes justified. The necessary requirement was to attain the minimum value of the $n\tau_E > 0.6 \times 10^{20} \text{m}^{-3}\text{s}$ product, where n is the plasma density and τ_E is the energy confinement time. This condition is also called the *breakeven*, or $Q=1$ condition, where $Q=P_{DT}/P_H$ is the standard labeling for the ratio of produced fusion power and applied heating power.

80% of the energy produced by fusion reaction is carried by neutrons which freely escape the plasma burning zone. The rest 20% of energy is carried by α -particles, which remain confined and transfer their energy to the surrounding thermal D-T plasma. Thus, roughly one fifth the produced fusion energy is retained in plasma, providing self-heating. At high enough reaction rate, the heating by α particles fully compensates energy losses from the system, and plasma reaches so-called *ignition* state – where it does not need any auxiliary heating to maintain its temperature. The $n\tau_E$ required to reach the ignition is a function of temperature with a minimum value equal to $n\tau_E \sim 1.5 \times 10^{20} \text{m}^{-3}\text{s}$ at about $T \sim 30 \text{keV}$. This criteria is not very convenient to use, since τ_E itself depends on T , so the optimum ignition condition will most likely be at temperatures lower than 30keV. Fortunately, the D-T reaction cross-section can be expressed as a linear function of T^2 for $T \sim 10\text{-}20 \text{keV}$ with good precision, and the *triple product* $n_e \tau_E T$ becomes independent of temperature in this range. That brings us to the universal and widely used criteria for the ignition condition: $n_e \tau_E T \geq 3 \times 10^{21} \text{keVm}^{-3}\text{s}$. That value is not yet attained in any present tokamaks, but planned to be barely achieved in the ITER device[9].

1.3 Tokamak

The tokamak concept was invented in the USSR in 1950 [1]. The idea was to confine plasma in a toroidal magnetic field, thus forcing plasma particles to follow closed trajectories inside a toroidal chamber. The strong longitudinal magnetic field inside the chamber is created by multiple toroidal field coils. These coils alone are insufficient to hold the plasma since charged particles will drift vertically to the walls very fast due to inhomogeneity of the magnetic field (B is proportional to $1/R$ in such a configuration, where R is the distance to the torus axis). To compensate this drift, field lines must be twisted in a helical form, using an additional, poloidal (or azimuthal) field such as to create a set of nested closed flux surfaces. In such a configuration the particles follow so called drift orbits, which are slightly deviating from the magnetic field lines.

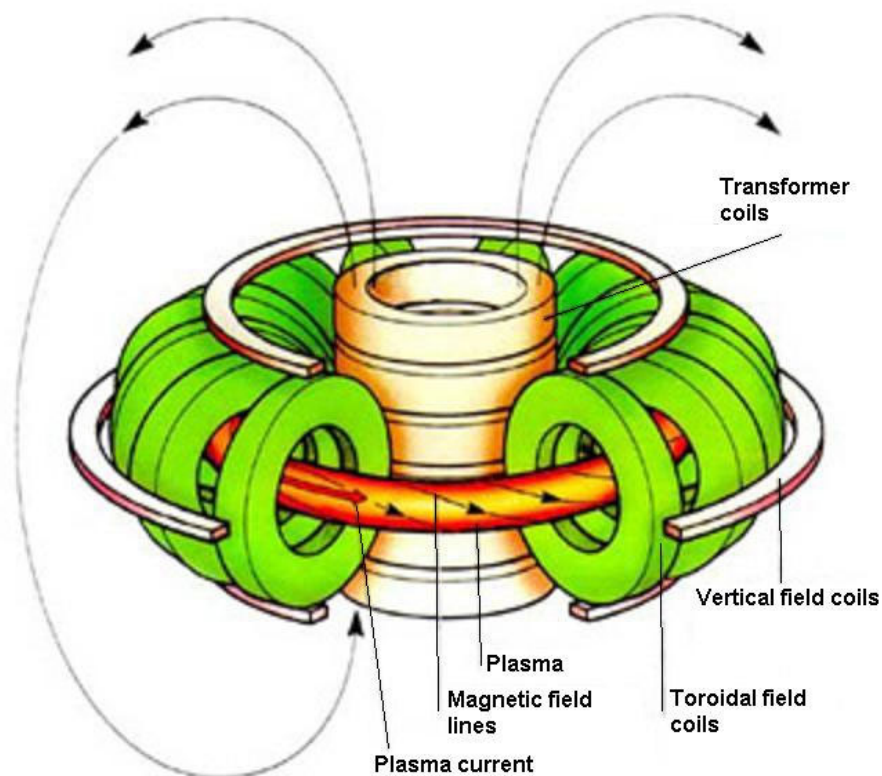


Figure 1.3.1 Schematic view of a Tokamak .

For sufficiently strong poloidal fields, the majority of these orbits are closed within the plasma and approximately symmetrical around the plasma midplane. For such orbits, even though the drift velocity is always in the same (vertical) direction, these particles drift, on average, as much away from the midplane as they drift towards it, i.e. the net vertical drift is zero. To create such a field in a tokamak, a toroidal current is induced inside plasma by

external transformer coils. That current also serves to heat the plasma by the Joule effect ('Ohmic' heating in fusion jargon), albeit only to temperatures which are too low for fusion applications.

As any current loop, plasma will experience an electrodynamic force which is directed outwards (that force is a result of interaction between the current and poloidal magnetic field induced by it). An additional vertical magnetic field, normally provided by a couple of poloidal field coils, must be applied to compensate that force and also serve to control the plasma vertical position. Additional poloidal coils are also used for controlling the plasma shape.

The efficiency of the Ohmic heating by the plasma current decreases rapidly with temperature and cannot be used to achieve the fusion burning conditions. Additional heating systems must be used to attain the desired temperatures. The sustainment of plasma current by electromagnetic induction requires a continuously increasing magnetic flux through the central solenoid, so it is therefore limited in time. To produce sufficiently long plasma pulses or for continuous plasmas, additional current sources must be provided. Most external heating systems are also capable of creating plasma currents non-inductively (current drive). A range of various diagnostics are used for plasma control and for research purposes. These include magnetic diagnostics for plasma positioning, various temperature and density measurements, neutron diagnostics, current profile control and many more.

1.4 Particle confinement.

In a strong homogeneous magnetic field, charged particles are moving freely along the magnetic field lines, but restricted in the perpendicular direction. In fact they are performing so-called cyclotron motion (or gyro motion) in this plane, which is a circular motion with the radius $r_L = \frac{m v_{\perp}}{e B}$, which is also called the Larmor radius. Here m – is the mass of particle, e – its charge, B – magnetic field, c – velocity of light and v_{\perp} - particles velocity in the direction perpendicular to the magnetic field. In the absence of collisions, a particle remains confined to a magnetic field line infinitely long. But if a collision occurs, the velocity direction of the particle can change arbitrary, and effectively the position of the guiding center can move by a step size of the order of r_L . Random collisions with other particles

provide diffusion across the magnetic field of a “random walk” manner. The diffusion coefficient in this case is equal to

$$D_{cl} = \nu \cdot r_L^2, \quad (1.4.1)$$

where ν is the collision frequency.

In real magnetic confinement devices, including tokamaks, the magnetic field is not homogeneous, and the particles' trajectories are more complicated. The model describing particles motion in a general inhomogeneous magnetic field is called the *neoclassical* model [10], to distinguish from the basic, classical model.

In case of tokamak plasma, a particle will experience a vertical drift due to presence of the magnetic field gradient and magnetic field lines curvature. In addition to that, during its motion along the twisted magnetic field lines, a plasma particle will go through the regions of stronger and weaker magnetic field, since $B \sim 1/R$ in tokamak. The total energy

$$E = \frac{m}{2}(v_{\parallel}^2 + v_{\perp}^2) \text{ and the magnetic moment } \mu = \frac{mv_{\perp}^2}{2B}$$

are invariants of the motion, so the particles with $\frac{v_{\parallel}}{v_{\perp}} < \varepsilon^{1/2}$ (ε is the inversed aspect ration, a/R) are not able to move into the

higher field region and will be reflected back. Instead of a doing a circular motion along a magnetic surface, these particles will be trapped at lower field side region and perform a bouncing motion with a banana-shaped trajectory. Even though the percentage of trapped particles is relatively small, they have significantly influence on the tokamak plasma properties and give rise to the most of the neoclassical effects.

The particles neoclassical diffusion coefficient becomes equal to:

$$D_{nc} = \rho_L^2 q^2 \left(\frac{R}{a}\right)^{3/2} \nu \quad (1.4.2)$$

in a low collisionality limit, and

$$D_{nc} = \rho_L^2 (1 + q^2) \nu \quad (1.4.3)$$

at high collisionalities. Here q is the safety factor, $q = d\Phi/d\Psi$, $d\Phi$ - is the increment of the toroidal flux and $d\Psi$ - is the increment of the poloidal flux. If $q=m/n$ is a rational value, then the corresponding magnetic field line will reconnect to itself after completing m toroidal and n poloidal turns. The safety factor value in tokamak is usually around unity in the center and increases up to 3-10 at the periphery. Comparing (1.4.2) and (1.4.3) with (1.4.1), one can see that the neoclassical diffusion in tokamaks is significantly stronger than in the classical case.

Apart from the diffusion transport processes, convective transport phenomena can be also observed in plasma. Convective transport arises as a result of collisions in the presence of temperatures gradients or gradients of the density of other particles (e.g. impurities) in the plasma.

In the neoclassical model one can distinguish two convection processes: the neoclassical thermodiffusion [10] and so-called Ware pinch [11] effects. Neoclassical thermodiffusion pinch appears in the presence of temperature gradients, $V_{th} \sim c_{th} \frac{\nabla T}{T}$ and is negligible in majority of tokamak plasma cases.

The Ware pinch is the result of the toroidal electrical field presence and its effect on the trapped particles. In an electrical field in the toroidal direction (as required for electromagnetic induction of a current), trapped particles do not follow the precisely closed trajectories, but slowly drift towards the plasma core, as it was predicted by Ware[11]. The drift direction does not depend on particles charge or orientation of toroidal and poloidal magnetic fields and can be expressed in a form:

$$\frac{dr}{dt} = V_{ware} = -c \frac{E_{\phi}}{B_{\theta}} \quad (1.4.4)$$

where E_{ϕ} is toroidal electrical field, B_{θ} is the poloidal magnetic field and c is the velocity of light. In the majority of cases, the Ware pinch is much larger than neoclassical thermodiffusion.

After taking into account the diffusion and convection components, the total particle flux in plasma can be expressed in a form:

$$\Gamma = -D_{nc} \frac{dn}{dr} + V_{ware} n \quad (1.4.5)$$

In a steady state case and the absence of core particle sources, total particle flux will be equal to zero, thus

$$D_{nc} \frac{dn}{dr} = V_{ware} n, \text{ or}$$

$$\frac{1}{n} \frac{dn}{dr} = \frac{V_{ware}}{D_{nc}} \quad (1.4.6)$$

We see that in presence of the convective transport, the normalized density gradient in plasma bulk is non-zero even in the absence of particle sources in plasma core, and is equal to the ratio of the convection velocity and diffusion coefficient.

Neoclassical diffusion and convection processes are well understood theoretically, but they are not determining particle transport in most of cases. In general, transport is measured to be much larger than expected from n.c. transport alone. The difference is referred to as anomalous transport. However it is generally also possible to divide anomalous transport into a diffusive and convective part, such that the total transport can be described by the sum of the n.c. and anomalous transport as

$$D=D_{nc}+D_{anomalous}, \quad V=V_{ware}+V_{anomalous}$$

Anomalous heat and particle transport was observed in tokamaks since the very beginning [12], but the existence of particle convection in plasmas has been a matter of dispute until recently. Experiments in TCV [13] and Tore Supra [14] tokamaks have provided an unambiguous demonstration of anomalous particle pinch in fully non-inductive plasmas discharges, showing that the steady state density peaking can be obtained in the absence of the Ware pinch. Transport analysis, done for various JET L-mode plasmas, has also shown that the anomalous inward convection must be present to explain the observed density gradients [15]. Later it was shown that the density peaking in L-mode plasmas on JET is in agreement with the Turbulent EquiPartition (TEP) theories[16], which are stating that the density peaking must be dependent on the q-profile peaking [17-19].

Existence of the anomalous pinch in H-mode plasmas was controversial for a long time, due to generally lower density peaking observed and higher core particle fueling by neutral beams. Although the recent research done on JET, AUG and C-MOD tokamaks [20-24] has shown that the density peaking behaviour in H-mode plasmas for these machines is almost identical and must be attributed to the existence of the anomalous particle pinch

1.5 Outline of the thesis

This thesis describes the work done for investigating the particle transport phenomena in tokamak H-mode plasmas, with a special focus on anomalous convective transport and its effect on density profiles. Chapter 1 briefly introduces the problem of controlled fusion and confinement in a tokamak. Chapter 2 is dedicated to density profile measurement techniques with emphasis on two commonly used diagnostics: Thomson Scattering and Far Infrared Interferometry which were extensively used for completing this research. Discrepancies between these measurements in JET, although little publicised, led to improvements of the

interferometry inversion and were successfully resolved by improvements of the Thomson scattering interpretive software as a part of this work.

Chapter 3 will introduce the JET tokamak and the empirical analysis done on the basis of JET experiments completed during 2006 and 2007. These results will be compared with those previously published.

Chapter 4 will give an introduction to the gyrokinetic theory and gyrokinetic simulations with an example how drift wave microscale instabilities can affect the particle transport and produce inward (up-gradient) particle transport. It will also present the results of gyrokinetic simulations with respect to the particle transport analysis and comparison with empirical data obtained on JET tokamak.

Chapter 5 describes experiments on the TCV tokamak, addressing the differences between these machines and differences in the experimental observations of the density peaking. It will be shown how the TCV empirical observations can be interpreted by linear gyrokinetic simulations.

Chapter 6 will provide the conclusions drawn from this work, discuss the issues and possible consequences for burning plasma reactors.

CHAPTER 2

Density profile measurements.

2.1 Introduction

Reliable density profile measurements are of a fundamental importance for particle transport research. In this chapter, two different density measurement methods will be discussed: Thomson Scattering and Far Infrared Interferometry. The implementation of these two diagnostics on the two tokamaks, JET and TCV, will be highlighted.

On the JET tokamak, an inconsistency between the two diagnostics was observed for a long time: the density peaking measured by the Thomson Scattering was systematically lower than measured by the FIR interferometer. To resolve this issue, the data processing of both diagnostics had to be improved.

2.2 The Thomson scattering diagnostic.

Thomson scattering is a process of electromagnetic radiation scattering by charged particles and was first explained by the British physicist J.J. Thomson (1856-1940). In its simplest form it can be described as a dipole radiation of a charged particle due to its acceleration in the electrical field of an incident electromagnetic wave. The total cross-section is extremely low, for electrons it is equal to $\sigma_T = 6.65 \cdot 10^{-25} \text{ cm}^2$. For protons this value is several orders of magnitude lower due to the higher mass and as a result – much lower susceptibility to oscillations caused by external electromagnetic field. Thomson scattering from protons usually cannot be detected in laboratory conditions.

In the particle rest frame of reference, the reemitted wave has the same frequency as the incident wave. But if the emitting electron is moving, the resulting wavelength is changed by the Doppler effect. Monochromatic light, such as provided by a laser, scattered by an ensemble of electrons is correspondingly broadened, containing information on the velocity distribution of these electrons. A formula describing the scattered light spectrum as a function of electron temperature, taking into account the relativistic effects, was derived by

J. Sheffield [25], and lately refined for higher precision by other authors [26]. An example is presented in figure 2.2.1

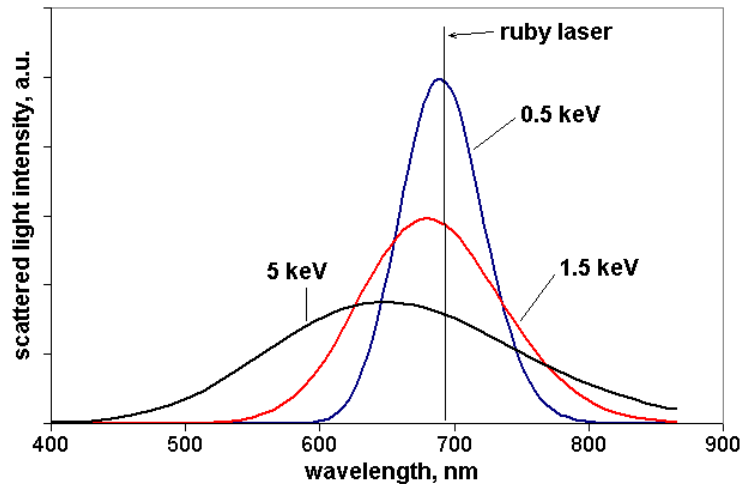


Figure 2.2.1: examples of Thomson scattering spectrum

The total amount of scattered light integrated over the whole spectrum gives information about the electron density at the scattering volume.

Thus Thomson scattering is a universal technique for measuring local electron temperature and density at the same time. In various forms it is used on every existing fusion plasma device. A classical diagnostic layout, as used on TCV, is presented on figure 2.2.2. A powerful pulsed Nd:YAG narrow laser beam is made to pass inside the tokamak chamber. As much as possible of the light scattered by the plasma is collected by viewing optics and directed to a grating spectrometer, or as in the case of TCV and JET, to a set of detectors equipped with pass-band filters. By analyzing the signal ratios in different spectral channels it is possible to derive the electron temperature, and the electron density is calculated from the total amount of detected scattered light. In TCV each of the 25 spatial positions corresponds to a different filter spectrometer.

Another type of Thomson scattering diagnostic called LIDAR (Light Detection And Ranging) is installed on JET tokamak [27,28]. An extremely short laser pulse $\sim 300\text{ps}$, with a repetition rate of 4Hz, is produced by a ruby laser and directed into the tokamak chamber by a set of guiding mirrors. In the torus, the laser pulse propagates nearly parallel to the equatorial plane, providing a scan of the whole plasma cross-section from the edge to the core. Backscattered light is collected through the same input window by the set of mirrors and returned by nearly the same path to a single spectrometer equipped with 6 filters. High bandwidth microchannel photomultipliers are used as detectors, which allow to measure the time evolution of the scattered light in each spectral channel with a time resolution $\sim 0.6\text{ns}$.

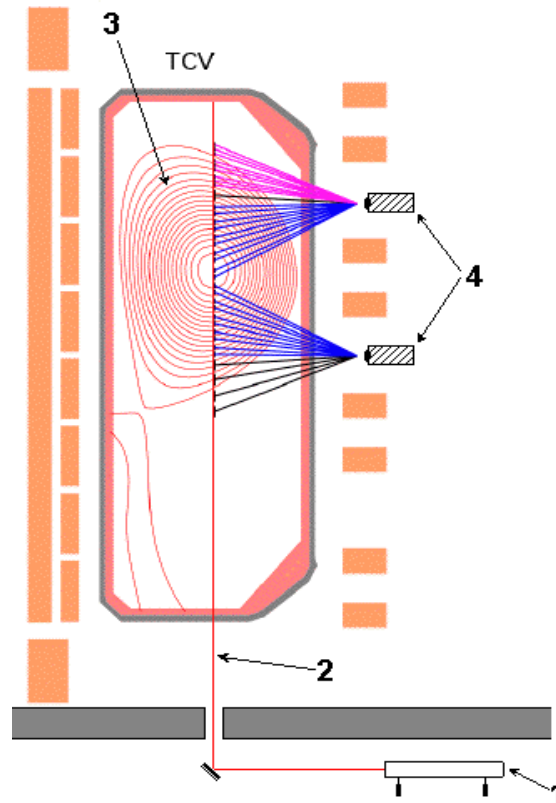


Figure 2.2.2. Thomson scattering diagnostic on TCV

1) High power Nd:YAG lasers. 2) Laser beam path. 3) TCV plasma, 4) Collection optics and detectors.

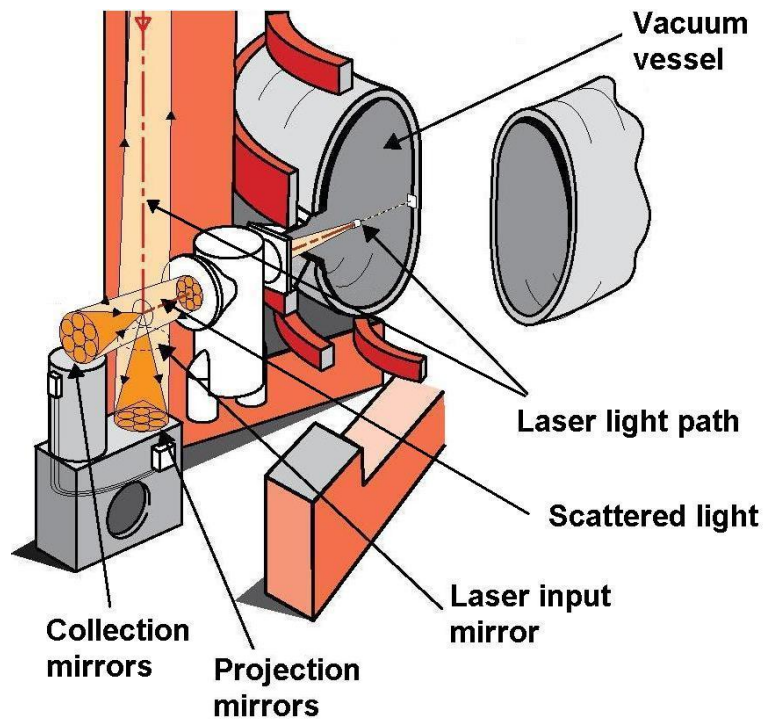


Figure 2.2.3: LIDAR diagnostic on JET

The signal dependence is converted to position based on the velocity of light, thus giving the whole plasma profile with $\sim 12\text{cm}$ resolution.

The LIDAR system has numerous advantages over the classical system like the one used on TCV. It requires minimum access to the vessel (same port for laser input and scattered light collection) and in this backscattering geometry, the signals is only weakly sensitive to laser misalignment. By gating the microchannel plates off for the time prior to the pulse entering the plasma, most of stray light from the components on the beam path can be avoided. The disadvantage is that such a system can be only be used on relatively large machines due to the limitations of the spatial resolution.

2.3 Far Infrared Interferometry.

The plasma refractive index for an electromagnetic wave can be expressed as

$$n^2 = 1 - \frac{\omega_{pe}^2}{\omega^2} \quad (2.3.1)$$

for the ordinary mode (O-mode), and

$$n^2 = 1 - \frac{\omega_{pe}^2}{\omega^2} \left(\frac{1 - \frac{\omega_{pe}^2}{\omega^2}}{1 - \frac{\omega_{ce}^2}{\omega^2} - \frac{\omega_{pe}^2}{\omega^2}} \right) \quad (2.3.2)$$

for the extraordinary mode (X-mode). ω_{pe} is plasma frequency $\omega_{pe} = (4\pi n_e e^2 / m_e)^{1/2}$, and ω_{ce} is the electron gyromotion frequency. In the case of $\omega \gg \omega_{ce}$ and $\omega \gg \omega_{pe}$ the difference between ordinary and extraordinary mode can be neglected and the dispersion equation can be approximated by the single equation (2.3.1). Taking into account that $n = ck/\omega$, we can write:

$$\frac{ck}{\omega} = \sqrt{1 - \frac{\omega_{pe}^2}{\omega^2}} \sim 1 - \frac{1}{2} \frac{\omega_{pe}^2}{\omega^2} \quad (2.3.3)$$

The phase change of the wave propagating through plasma is equal to:

$$\varphi = \int k \cdot dl = \int \left(\frac{\omega}{c} - \frac{\omega_{pe}^2}{2c\omega} \right) dl = \varphi_0 - dl = \varphi_0 - \frac{4\pi e^2}{2c\omega m_e} \int n_e dl \quad (2.3.4)$$

Here φ_0 is the phase of that wave propagating in vacuum. One can see that the phase difference is proportional to the line integrated electron density along the beam path. The principle of interferometric measurements is to determine the phase shift between an

electromagnetic beam passing through the the plasma and a reference beam passing outside the plasma. The heterodyne Mach-Zehnder scheme [29] is the one most commonly used for that purpose (Fig. 2.3.1)

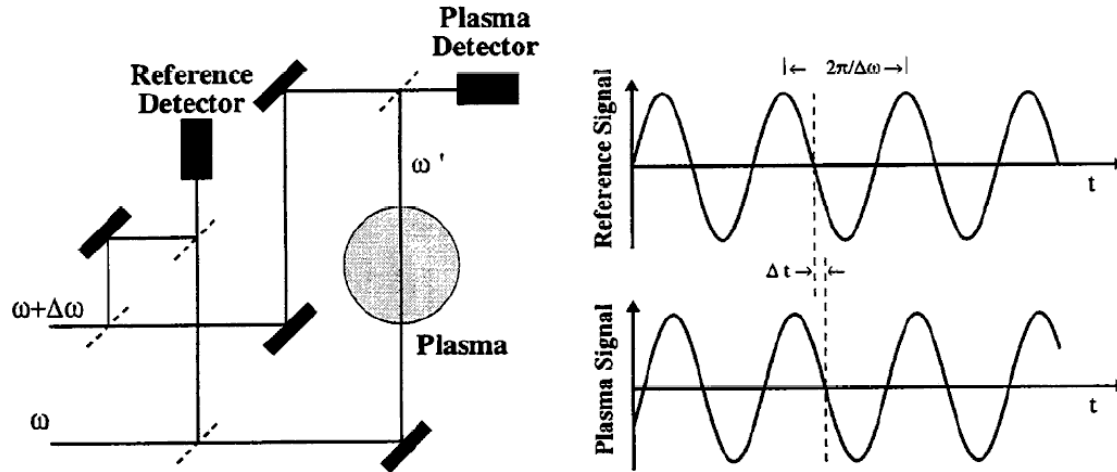


Figure 2.3.1: Schematic representation of a heterodyne Mach-Zehnder Interferometer.

It involves a reference beam shifted in frequency with respect to that passing through the plasma and hence provides a beat signal at the difference frequency, with a phase that depends linearly on the phase shift introduced by the plasma. This phase shift is measured, up to a constant, using mixing electronics with respect to a reference beat signal from an interferometer channel not passing through the plasma. The constant is determined in the absence of the plasma, e.g. prior to the tokamak pulse. By using several laser beams passing through the plasma at different radial positions one can reconstruct the electron density profile by means of inversion techniques, which will be discussed in the next section.

For typical tokamak plasmas, the optimum wavelength is in the far infrared (FIR) because the phase shift is significant (typically several times 2π), without excessive refraction by density gradients. The FIR interferometer is a very reliable measurement which is used for a live feedback control of the plasma density. Contrary to the Thomson scattering measurements, FIR interferometry does not require powerful pulsed lasers and is able to produce the measurements continuously with a good time resolution (usually a few ms or less).

2.4 Inversion techniques.

To calculate the radial density profile from the set of line integrated measurements one must perform a mathematical inversion. That problem is equivalent to solution of a system of equations (the number of equations is equal to the number of line integrated measurements) but in general is not applicable as such to real measurement data and requires some additional stabilization measures.

To perform a discrete inversion one divides the plasma into a set of poloidal flux surfaces assuming that the density between neighboring surfaces is constant. Thus we approximate the density profile by discrete values $X_{1..M}$. For a complete description of the system we must know also the shape of each flux surface and the path of each FIR laser beam used for the measurements. The flux surface geometry is calculated by an equilibrium reconstruction code which runs routinely (that is EFIT[30] on JET and LIUQE[31] on TCV) . The FIR measurement chords are fixed by the diagnostic design, while beam refraction is usually negligible.

Let's assume we have $\{N\}$ line integrated measurements $B_{1..N}$. Then one can write the matrix equation:

$$\begin{bmatrix} A_{11} & \dots & A_{1M} \\ \dots & \dots & \dots \\ A_{N1} & \dots & A_{NM} \end{bmatrix} \times \begin{bmatrix} X_1 \\ \dots \\ X_M \end{bmatrix} = \begin{bmatrix} B_1 \\ \dots \\ B_N \end{bmatrix} \quad (2.4.1)$$

where $X_{1..M}$ are the local values of density on M flux surfaces, $B_{1..N}$ are the line integrated densities on N available lines and $A_{1..N,1..M}$ are the contributions of each flux surface interval to each line integral. $A_{n,m}$ is the total distance along chord $\{n\}$ between the two adjacent flux surfaces $\{m\}$ and $\{m+1\}$, as shown on figure 2.4.1

The system of equations (2.4.1) is usually underdetermined ($M > N$). In order to decrease the number of variables, the methods adopted here use K basis functions with $K \leq N$ to make the equations solvable. There is no universal set of basis functions, for different application one should determine the most appropriate one. In this work two different sets (figure 2.4.2a,b) are used, one is triangular partially overlapping basis functions (the first function is actually a trapezium which makes all possible solutions to be flat in the very center). Another group of basis functions consists of the topos from the singular value decomposition (SVD) [32] of different pre-defined "standard" density profiles. Due to the properties of SVD decomposition, these functions are naturally orthogonal to each other.

We define a matrix $C_{1..K,1..M}$ such that every column $C_{k,1..M}$ will represent each of the K basis functions. The density profile $X_{1..m}$ will be presented as a sum of K basis functions with the coefficients $Y_{1..k}$

$$\begin{bmatrix} X_1 \\ \dots \\ X_M \end{bmatrix} = \begin{bmatrix} C_{11} & \dots & C_{1K} \\ \dots & \dots & \dots \\ C_{M1} & \dots & C_{MK} \end{bmatrix} \times \begin{bmatrix} Y_1 \\ \dots \\ Y_K \end{bmatrix} \quad (2.4.2)$$

Substitution of $X_{1..M}$ from (2.4.2) into (2.4.1) gives us:

$$\begin{bmatrix} A_{11} & \dots & A_{1M} \\ \dots & \dots & \dots \\ A_{N1} & \dots & A_{NM} \end{bmatrix} \times \begin{bmatrix} C_{11} & \dots & C_{1K} \\ \dots & \dots & \dots \\ C_{M1} & \dots & C_{MK} \end{bmatrix} \times \begin{bmatrix} Y_1 \\ \dots \\ Y_K \end{bmatrix} = \begin{bmatrix} B_1 \\ \dots \\ B_N \end{bmatrix} \quad (2.4.3)$$

Replacing the matrix multiplication $[A]_{1..N,1..M} \times [C]_{1..M,1..K}$ by the matrix $[A^*]_{1..N,1..K}$ for simplicity:

$$\begin{bmatrix} A^*_{11} & \dots & A^*_{1K} \\ \dots & \dots & \dots \\ A^*_{N1} & \dots & A^*_{NK} \end{bmatrix} \times \begin{bmatrix} Y_1 \\ \dots \\ Y_K \end{bmatrix} = \begin{bmatrix} B_1 \\ \dots \\ B_N \end{bmatrix} \quad (2.4.4)$$

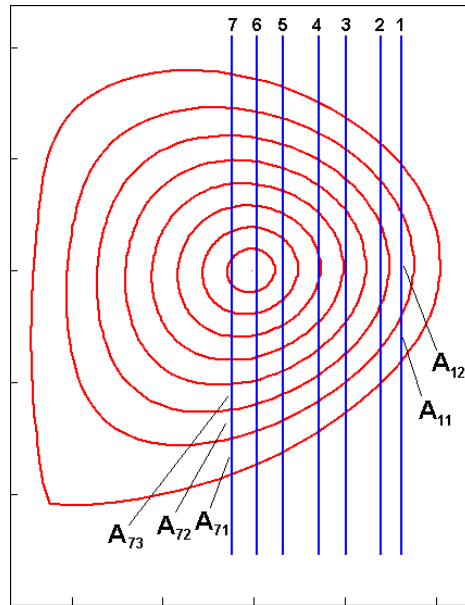


Figure 2.4.1 Calculation of the geometry coefficient A_{nm}

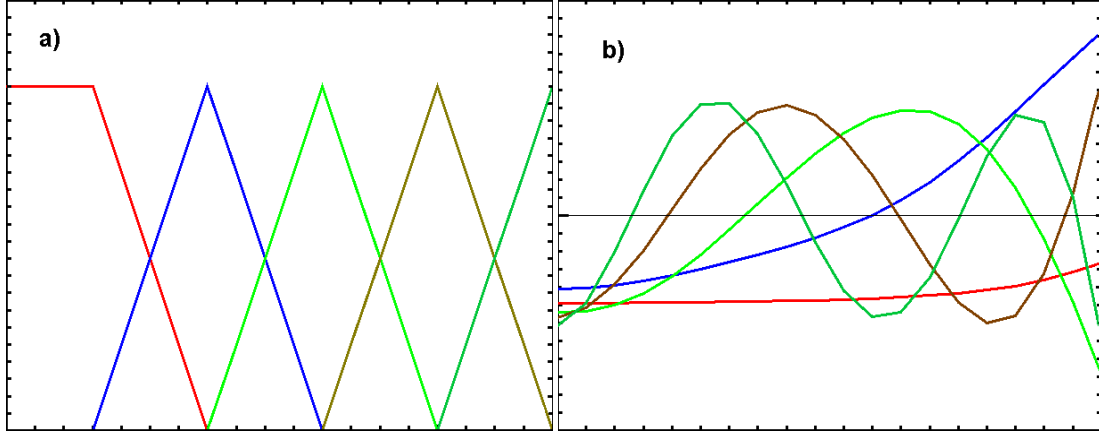


Figure 2.4.2: two sets of 5 basis functions, as they were used for the inversion of FIR measurements on JET, a) simple triangles, b) SVD generated.

For the case of $K=N$ and non-zero rank of the matrix A^* the system of equations (2.4.4) gives a solution for $Y_{1..K}$. In general case $K \leq N$ we have to use the minimum square root fit.

Let's define χ^2 in the following way:

$$\chi^2 = \sum_n \left(\sum_k A_{nk}^* \times Y_k - B_n \right)^2 \quad (2.4.5)$$

To find the best $Y_{1..k}$ solution we have to minimize χ^2 by solving the following system of equations:

$$\chi^2 = \min, \frac{\partial(\chi^2)}{\partial Y_j} = 0, j=1 \dots K \quad (2.4.6)$$

which transforms into the following:

$$\sum_k \left(\sum_n A_{nj}^* A_{nk}^* \right) Y_k = \sum_n A_{nj}^* B_n \quad (2.4.7)$$

This is the system of K equations and K unknown variables $Y_{1..K}$ which has a unique solution as long as the matrix A^* has a rank equal to K . This is normally the case if the line integrated measurements are not duplicating each other. The solution corresponds to the minimum of χ^2 and the density profile calculated by substitution of the $Y_{1..K}$ values into (2.4.2) will produce line integrated values closest possible to the measured ones $B_{1..N}$. In case of $K=N$, χ^2 will be equal to zero and the back-calculated line integrated values will match the measured ones perfectly.

Unfortunately, this technique does not work in real experimental conditions due to the presence of errors [33]. Small variations of the coefficients $A_{1..N,1..M}$ due to imperfect

equilibrium reconstruction or of $B_{1..N}$ due to the error bars in the measurements cause a variations of $X_{1..M}$ which can be very significant.

To illustrate the performance of the inversion we will take a real tokamak plasma geometry (TCV, #29882) with 7 FIR measurements as shown on figure 2.4.1.

Taking a predefined density profile $X_{1..M}$ we can calculate line integrated values for each of the chords using the expression (2.4.1), add a noise of some level to that measurements, run the inversion procedure and compare the result with the initial profile.

On figure 2.4.3a one can see the results of the inversion without adding any noise. Three different initial density profiles are assumed: high peaking (1), low peaking (2) and a hollow (3) one. For all three types of profiles we performed the inversion with both sets of basis functions illustrated on figure 2.4.2. In all cases the inverted profiles are very close to the initially assumed, so the inversion worked very well.

Now we add a random noise of a maximum 0.5% level to the line integrated data, which can still be considered a fairly precise measurement in a real experimental condition. The result is presented on figure 2.4.3b. As we can see, even a trifling disturbance of the measurement causes a dramatic change of the final result. That's why the Abel inversion in the form (2.4.7) is not usable and must be modified to prevent such unstable solutions.

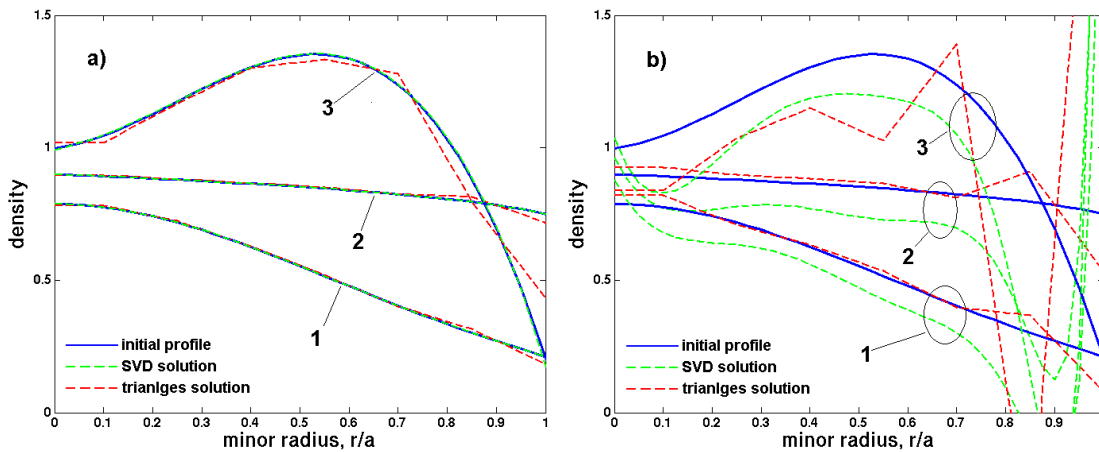


Figure 2.4.3: Abel inversion for 7 basis functions and 7 measurement chords.

(a) – without a noise, perfect reconstruction, (b) 0.5% noise level to line integrated data.

There are different methods to stabilize the inversion, such as using a SVD-I inversion [34] of density profiles from other diagnostic (e.g. Thomson scattering) as basis functions or so-called minimum Fisher method [35].

The method used in this work will be described in the following section. It resembles the minimum Fisher method in some aspects, but uses a flexibly adjusted regularization coefficient which provides 100% stability.

2.4.1 The “least regularized” inversion

Solutions on figure 2.4.3b are not reasonable from a physical point of view. Although they produce line integrated densities very close to the measured ones, the profiles themselves contain unphysical variations of density gradients and negative density values.

The second derivative of the density profile $X_{1..M}$ can be approximated as:

$$\begin{aligned} \frac{d^2 X_m}{dr^2} &= X_{m-1} - 2X_m + X_{m+1} = \sum_k C_{m-1,k} Y_k - 2\sum_k C_{m,k} Y_k + \sum_k C_{m+1,k} Y_k = \\ &= \sum_k (C_{m-1,k} - 2C_{m,k} + C_{m+1,k}) Y_k \end{aligned} \quad (2.4.1.1)$$

Let's define δ^2 as following:

$$\delta^2 = \sum_m \left(\frac{d^2 X}{dr^2} \right)^2 = \sum_{m=2..M-1} \left(\sum_k (C_{m-1,k} - 2C_{m,k} + C_{m+1,k}) Y_k \right)^2 \quad (2.4.1.2)$$

This value represents the “curvature” of the density profile and we will include it into the minimization of χ^2 (2.4.6).

$$\chi^2 + \alpha * \delta^2 = \min, \frac{\partial(\chi^2 + \alpha * \delta^2)}{\partial Y_j} = 0 \quad , j=1..K \quad (2.4.1.3)$$

The coefficient α is the regularization parameter, $\alpha=0$ will return us to our basic case (2.4.6) without regularization, $\alpha \rightarrow \infty$ will produce a result with zero 2nd derivative (a straight line).

Expression (2.4.1.3) is a system of equations of K unknown variables $Y_{1..K}$ similar to (2.4.7) but now its solution depends on α . The essence of the stabilization method proposed in this work is that χ^2 of the “correct” and “incorrect” solutions (as in figures 2.4.3ab) differs very little whilst δ^2 differs significantly, so for a certain α value the solution of (2.4.1.3) will have small χ^2 , i.e. will be consistent with line integrated measurements, and small δ^2 , i.e. will have a reasonable shape at the same time.

On figure 2.4.1.1 the result of test runs with different α is presented. The initial density profile is shown as a solid blue line on 2.4.1.1b, a noise level of 1% was added to the reconstructed line integrals.

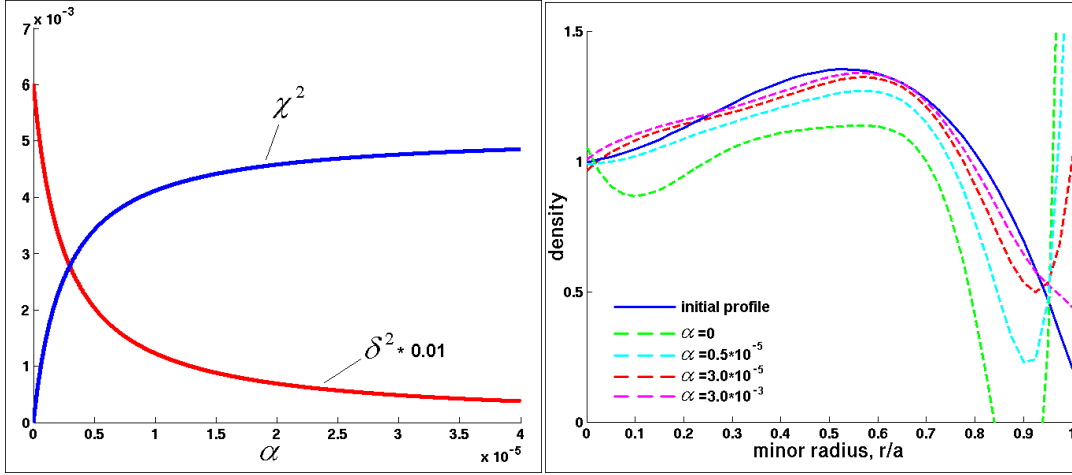


Figure 2.4.1.1 a) χ^2 and δ^2 for different stabilization parameter α
 b) inversion solutions for different α , SVD basis, 1% noise level.

As one can see (Fig. 2.4.1.1a) at $\alpha=0$, the basic Abel inversion case, we have a perfect match with the “measured” line integrals i.e. $\chi^2=0$, but the resulting density profile is very different from the initial one (figure 2.4.1.1b solid blue and dashed light green lines).

With increasing of parameter α , χ^2 increases and saturates around some value which represents the error of line integrated measurements, while δ^2 drops down fast to a value which corresponds to the “curvature” of the real density, and then slowly approaches zero at $\alpha \rightarrow \infty$. Figure 2.4.1.1b shows how increasing α leads to a physically acceptable solution (light green – light blue – red – magenta).

There is no unambiguous way to find the ideal α value for the inversion. Using too high value may result in smoothing some density profile features, using too low value may be not enough to stabilize the inversion and assure its convergency to the realistic density profile. In the minimum Fisher method the regularization coefficient value is derived from the expected errors of the line integrated density measurements.

In this work the principle of successive approaches was used: by recursive solution of the equation (2.4.1.3) the minimum value of α parameter which gives a “satisfactory” result is found. The criteria for the quality of the inversion were that the density profile must be monotonic and central density value must not be lower than the edge density. (This is justified by the fact that we have never in JET seen any evidence for hollow density profiles). So the computer code solves the matrix equation 2.4.1.3 for the initial value of $\alpha=0$, then increases the coefficient if the solution is not monotonic and decreases it if the profile is monotonic already. By continuously decreasing the step size, the minimum value

of α (with some pre-defined accuracy) is found. This profile will be referred as the “least regularized monotonic solution”.

This method guarantees 100% convergency to a monotonic density profile with a peaking factor not less than 1.0. The quality of the inversion can be controlled by checking the final χ^2 parameter, which represents the difference between measured line integrated densities and ones obtained with the output density profile. For the JET data analysis, the limit of 5% inconsistency summarized over all measurement channels (6 are used) was established, to ensure the good quality of the data. Experience shows that this value is easily attainable if the plasma density evolution is not too fast and there is no fringe jump error in the measurements (a 2π phase change which was not resolved by the detection system).

An IDL computer code for the FIR data inversion was developed and used for the JET density profile study described in this thesis. Inversions for both sets of basis functions were calculated alongside and a good match between the results was observed in all the cases of consistent input data.

This inversion method was also implemented for the TCV data (example is on Fig. 2.4.1.2) and used in the particle transport analysis described in further sections.

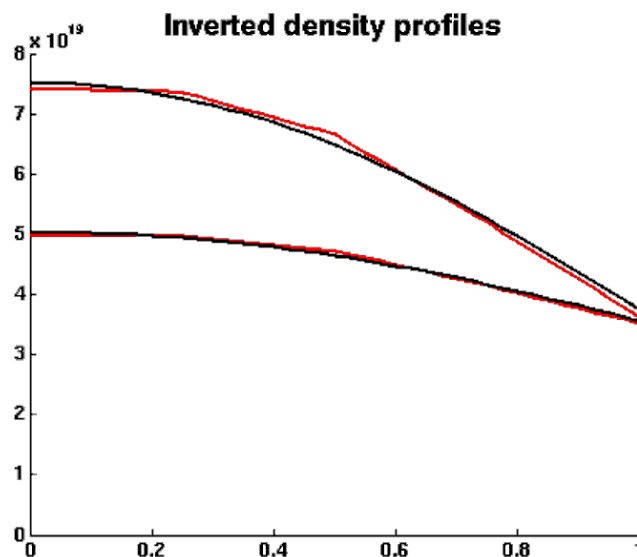


Figure 2.4.1.2: Example of the FIR inversion on TCV #3281, chords 3-8 are used $t=0.8$ and 1.4 s density profile changes from peaked to flat. black – 5 SVD type basis functions (fig 2.4.2b), red – 5 triangle basis functions (fig. 2.4.2a) $\chi \sim 2.5\%$

TCV has 14 measurement chords, all of them vertical, covering both the high and low field sides of the plasma. But the high field side chords also cross the divertor region, hence accumulating a phase shift from the densities which don't belong to the main plasma. For that reason, the measurements used for inversion were limited to 8-9 low field side chords. Since the shape of density profiles, considered in our analysis, is quite simple, using 9 chords and 9 basis functions is more than enough in a general case. On Fig. 2.4.1.3 one can see an example of different inversion done for TCV shot #29882, $t=1.1$ s.

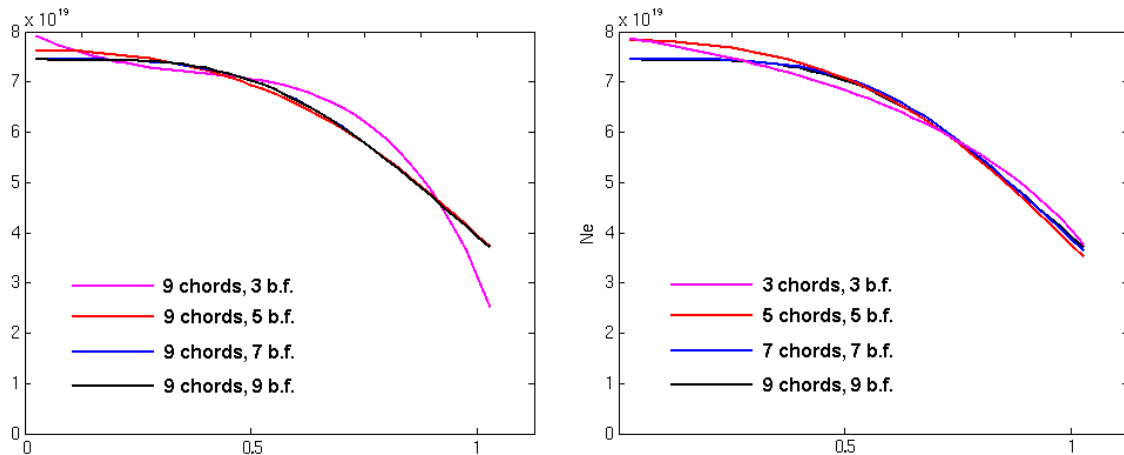


Figure 2.4.1.3: examples of FIR inversions for TCV shot #29882, $t=1.1$ s using different number of measurements and basis functions.

As one can see, the results with different number of basis functions are quite close to each other, and the results with 7 and 9 chords are not distinguishable from each other.

2.5 Consistency in density profile measurements from the LIDAR and the FIR diagnostics on JET.

The problem of consistency for the density profile measurements, which existed on JET [36], was addressed during completion this thesis work and successfully resolved. The core of the problem lied in the LIDAR data processing algorithm, which will be described briefly in this section.

As already discussed in the section 2.2, LIDAR is a time-of-flight measurement. Signal in each of the channels is a time trace, which represents the scattered light intensity at each point of the ~ 300 ps laser pulse flight path. An example of the measurement is presented in figure 2.5.1 The first signal spike at $t \sim 35$ LIDAR clock units (1 c.u. ~ 0.15 ns) corresponds to

the time reference which is used for the spatial position calibration. The signal during $t=70-140$ c.u. is the light scattered from plasma (useful signal) and the spike at the end of the flight corresponds to the light scattered from the wall of the tokamak chamber as it is hit by the beam. The interval $t\sim 45-70$ c.u. corresponds to propagation of the laser pulse in vacuum and is used for determination of the background level.

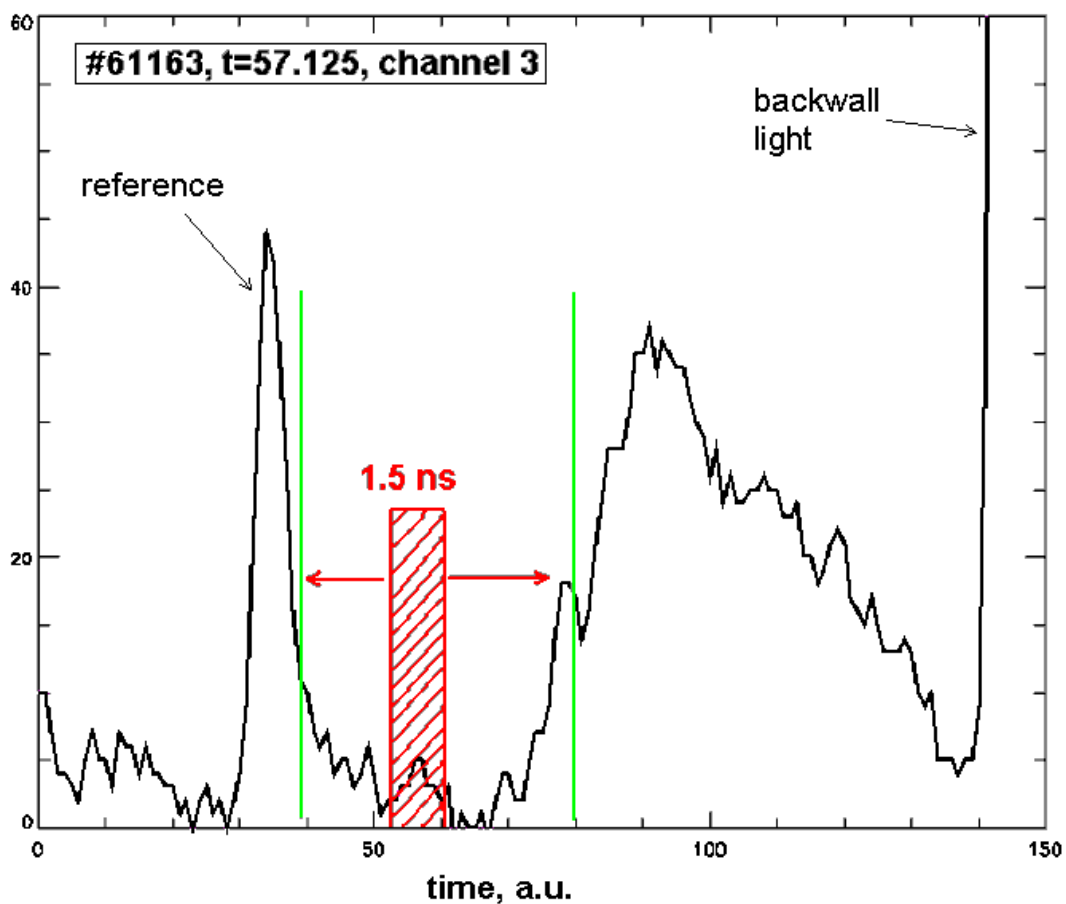


Figure 2.5.1: example of the LIDAR raw measurement data from one of the microchannel plate PMTs.

To avoid the spurious effect of possible stray light spikes, the following algorithm was used for determination of the actual background level. A small window is taken (roughly 20% size of the “clean” zone $t \sim 45-70$ c.u.) and the background signal is defined as an average inside that small zone. That is done for **all** possible positions of that smaller interval inside the safe zone and the lowest value of the background level is chosen as final. In case of appearance of a spurious signal spike inside the $t\sim 45-70$ c.u. zone, this method helps to avoid the inclusion of it into the background value.

The plasma density in each particular position is calculated in the following way (simplified):

$$n_e = (S_{\text{raw}} - S_{\text{back}}) / S_{\text{raman}}$$

where S_{raw} is the measured raw signal, S_{back} is the background level and S_{raman} is the Raman absolute calibration.

The Raman calibration reflects the fraction of light which is acquired by the detection system in each spatial point. It is measured separately by firing the laser into the tokamak chamber filled with N_2 gas. An example of it is given on figure 2.5.2. As one can see, the light collection efficiency is low near the edges of plasma (due to vignetting for the low field side and $1/r^2$ solid angle decrease for the high field side). The highest light collecting efficiency is near the plasma core.

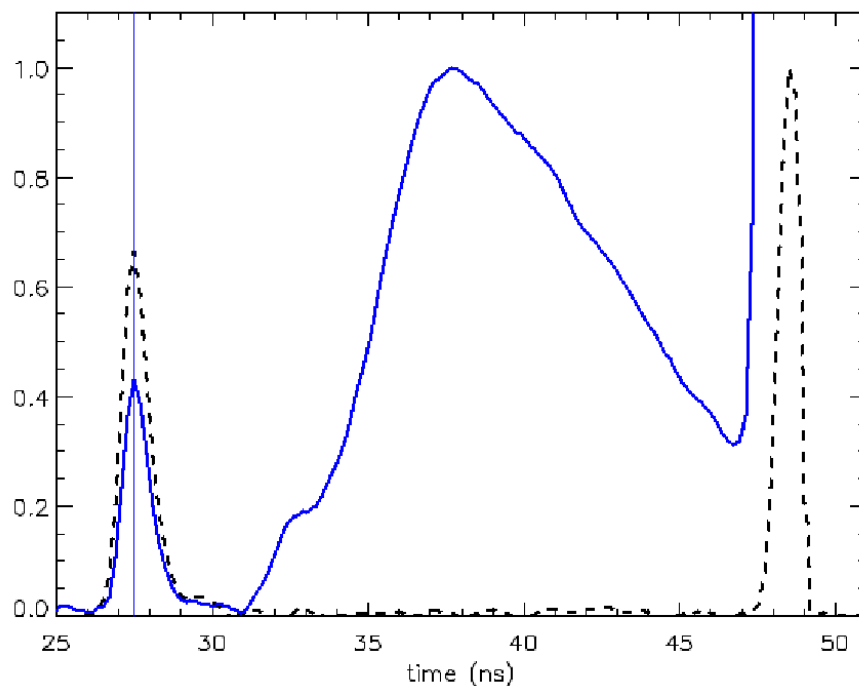


Figure 2.5.2: Raman scattering calibration (solid blue line) together with the backwall position (dashed black line)

In case of an error in the determination of the background signal, an offset (positive or negative) to the measured signal will be produced. That offset will be divided by the peaked Raman calibration curve and will produce an erroneous non-uniform addition of the Raman curve shape (Fig. 2.5.2) to the final density profile and will affect the shape of the profile.

It turned out that the method previously used for estimating the background level (which is described above) led to a systematic underestimate and this was one of the main reasons for the inconsistency between different density measurements observed on JET. A new way of

background level estimation was implemented in the LIDAR processing code, leading to much better agreement.

The new method was called a “two-sigma” method for reference. The principle is following: for the whole interval of the background signal the mean value and the standard deviation value are calculated. After that a single point with maximum difference from the overall mean value is selected. If the difference exceeds the double standard deviation interval – that point is removed from the consideration. That procedure is repeated until all measurement points are inside the double standard deviation interval and the final mean value will be the result.

To check the performance of different methods, the following test was done. An array of 50 random numbers was generated. Those values were set to have zero mean value and a standard deviation equal to unity. This array represented the LIDAR measurement in the background region. Then we applied three different algorithms for the background level determination: the usual mean value, the new “two-sigma” method and the moving window method (window size is 12 points, $\frac{1}{4}$ of the array size) used for the LIDAR before. That was repeated many times for different randomly generated arrays and the results were stored in a database.

In table 2.5.1 one can see the statistics of background level estimations by those methods after completing 1000 tests.

Table 2.5.1: Test results for different background calculation methods. No stray light.

Method:	Usual mean value	Two-sigma	Old LIDAR
Average 1000 runs result:	-0.000478	0.00031	-0.404
Standard deviation:	0.138	0.176	0.1936

As we can see, in the absence of a spurious stray light, the two-sigma method produces a correct result, while the moving window method gives a biased value.

For the second test, we added an artificial stray light rectangular signal with the width of 10 points and amplitude equal to 5 times the standard deviation of the background noise. The averaged value increased by a predictable $5 \cdot 10 / 50 = 1.0$ value, since the stray light spike was just added to the measured background. The two-sigma method filtered out the spurious signal completely and the moving window method shows the same tendency as in the previous test, so we just effectively decreased the window size.

Table 2.5.2: Test results for different background calculation methods. Sharp rectangular stray light.

Method:	Usual mean value	Two-sigma	Old LIDAR
Average 1000 runs result:	1.0998	0.0220	-0.3095
Standard deviation:	0.1377	0.2423	0.2152

For the last test we used a stray light spike of Gaussian form with the same amplitude and 10 points width $A=5*\exp(-(x_0/5)^2)$. Results are in the table 2.5.3

Table 2.5.3: Test results for different background calculation methods. Gaussian stray light.

Method:	Usual mean value	Two-sigma	Old LIDAR
Average 1000 runs result:	0.8905	0.2459	-0.2611
Standard deviation:	0.1423	0.2200	0.2151

As we can see, big part of the stray light spike was suppressed, only the low amplitude wings of Gaussian function were mixed up with the background noise signal and produces a small upward shift of the calculated average. The moving window method still produces an underestimated background.

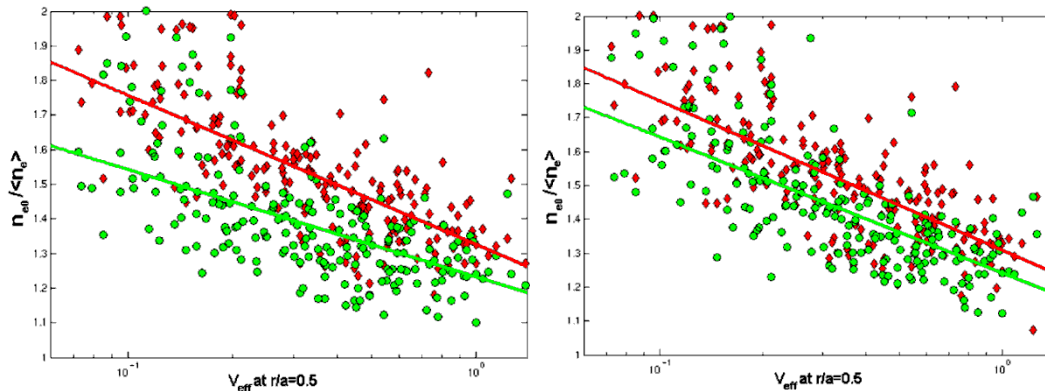


Figure 2.5.3: Density peaking versus effective collisionality measure by LIDAR (green circles) and FIR (red diamonds) during 2000-2004 experiments; left – before LIDAR code correction, right – after.

Following the test results, it was decided to implement the two-sigma filtering algorithm into the actual LIDAR data processing code and recalculate all the experimental data of the 2000-2004 campaigns. As a result the observed discrepancy between the two density profile

diagnostics (LIDAR and FIR inversion) was significantly reduced (Fig 2.5.3). Small inconsistencies between the two diagnostics remain and were observed also in the 2006-2007 data used for this thesis work. In average, FIR inverted profiles have a slightly higher peaking factor, but in comparison with the observations done before the LIDAR code correction, this discrepancy is constant and apparently not dependent on experimental conditions. The most probable reason for the discrepancy is different reconstructions of the edge part of density profiles, where both the core LIDAR diagnostic and the FIR interferometer lack sufficient resolution.

Since the discrepancy remains constant, empirical scaling coefficients of density peaking versus other plasma parameters are independent of the diagnostic is used for the analysis, only the constant offset changes. As a result, all the conclusions on parametric dependences of density profile behavior, which are stated in this work, are valid for both methods of density profile measurements.

CHAPTER 3

Experimental data analysis on JET

3.1 Introduction

Numerous studies of density profile behaviour had been done in 2003-2005, at the time when this thesis work started. An analysis of L-mode plasmas [16] had clearly shown the existence of an anomalous pinch, which appeared to be significantly influenced by the q -profile shape. Fully non-inductive plasma discharges, i.e. with zero Ware pinch, achieved on the TCV [13] and TORE-SUPRA [14] machines had unambiguously demonstrated the existence of anomalous pinches, at least in L-mode plasmas.

However an anomalous pinch in H-mode plasmas was not immediately evident. The L-H transition usually leads to a significant flattening of the density profile, with peaking factor sometimes as low as $n_0/\langle n \rangle = 1.0$, i.e. flat density profiles. (Flat density profiles were taken as an assumption for the ITER H-mode plasma in [51]). When non-zero density gradients were observed H-mode plasma, they were usually accompanied by significant core fuelling produced by NBI heating and were usually attributed to the effects of core fueling. Additionally, systematic inconsistencies in the density measurements produced by the two main JET diagnostics (LIDAR and FIR) fuelled ambiguity.

However careful statistical analyses of many H-mode experiments done on the JET and AUG tokamaks [21-23] have shown that the density peaking in H-mode increases with decreasing electron collisionality and cannot be attributed solely to changes in NBI core fueling. The work done on JET diagnostics has finally removed the inconsistency between them (as described in Chapter 2 of this thesis) and provided additional support to the conclusions derived in [21-23]. But the difference between density peaking behavior observed in L-mode and H-mode plasmas, as well as a mechanism behind the anomalous density peaking was still unclear.

As a part of this thesis work it was decided to make an independent analysis of H-mode plasmas based on the data acquired in JET experiments done during 2006-2007 experimental campaigns. Namely, the goal was to determine, which plasma parameters affect density peaking in H-mode steady state plasmas, to suggest corresponding scaling relations, to extrapolate it to the ITER condition and to compare the results with earlier work.

3.2 The JET tokamak

The Joint European Torus (JET) tokamak is situated at UKAEA Culham science center in the United Kingdom. The first plasma pulse on JET was achieved in 1983 and since that time JET remains the largest functioning magnetic confinement fusion device in the world. In 1991 the world first controlled release of D-T fusion power was produced, and subsequently in 1997 a new record of 16MW [37] fusion power during ~1.4 seconds was set. Since 1999 JET is operated under the EFDA (European Fusion Development Agreement) responsibility with the main focus on supporting the outstanding R&D issues related to the ITER project. The main technical parameters of JET are shown on table 3.2.1

JET is currently equipped with an NBI (neutral beam injection) heating system, an ICRH (ion cyclotron resonance heating) and an LHCD (low hybrid current drive) system. The NBI system [38] consists of 16 (2x8) PINIs (positive ion neutral injector) which operate at 85keV and 120keV beam particle energy.

The ICRH system [39, 40] consists of four antennas able to operate with different phasing and over a wide range of frequencies (23-56MHz). The maximum ICRH power registered in our 2006-2007 database is as high as 9MW, since ELMs (usually an unavoidable attribute of H-mode plasmas) severely reduce the efficiency of the ICRH coupling. The new ITER-like antenna (2007, [41]) has a potential to increase the coupled cyclotron heating power up to 22MW, but during the experimental period covered by this work (C15-C19 campaigns), it was not yet installed.

The LHCD system [42] is capable of launching the power up to 3MW and is used for tailoring of the safety factor (q) profile for achieving hybrid H-modes and advanced scenarios, including internal transport barriers [43].

Various diagnostics are installed on JET to measure different plasma parameters. The two main diagnostics (LIDAR and FIR) for measuring the electron density are described in the previous sections. In addition to the core LIDAR system, JET also uses the edge LIDAR (for measuring the H-mode pedestal parameters) and high frequency high resolution Thomson scattering (commissioned in 2007) [44].

Table 3.2.1: JET's main features, design and maximum attained.

	JET design parameters (1975)	Maximum values achieved separately (2008)
Major and minor radius (m)	2.96 1.25	3.0 1.25
Elongation	1.7	1.8
Magnetic field on axis (T)	3.4	4
Plasma current (MA)	4.8	7
Current plateau duration (s)	10	60 (1 MA)
Modes of operation	L mode	L, H and ELMy H
Plasma contact	Limiter (Divertor possible)	Carbon and beryllium limiters – Pumped Divertor
Neutral Injection Heating (MW)	Initially 10 25 envisaged	24
Coupled ICRH (MW)	0	22
Coupled LHCD (MW)	Possible	7.3
Current Drive (MA)	Not foreseen	3 (LH)
Central electron density (m ⁻³)	$\gg 10^{20}$	2×10^{20}
Electron Temperature (keV)	$\gg 10$	20
Ion Temperature (keV)	$\gg 10$	40
Q value in DT plasma	From 0.1 to 2	0.6 (0.9 net)
Fusion Power (MW)		16
Fusion Energy released in one pulse (MJ)		22 in 4s

Along with the Thomson scattering systems, the electron temperature is measured by 2 different Electron Cyclotron Emission (ECE) diagnostic, a Michelson spectrometer and a heterodyne 48-channel radiometer. Charge exchange recombination spectroscopy (CXRS) is used for measuring the ion temperature and plasma rotation velocity. There is a variety of other diagnostics, such as visible/UV/X-ray passive spectrometers, neutron spectroscopy, bolometers, numerous magnetic coils and many other, more specific diagnostics.

3.3 JET 2006-2007 experiments and H-mode plasmas database.

The experimental campaigns C15-C19 were executed on JET between April 2006 and April 2007 with a few short breaks in between. More than 5000 plasma pulses were produced. For this investigation on particle transport all of those shots were manually analyzed and more than 700 of them were selected, using the following criteria:

- The plasma has an H-mode phase with a plateau period lasting at least ~ 1 s, with a steady state density profile (FIR traces averaged over ELMs period are stable).
- Soft X-ray traces are also stable during that period, indicating there is no significant temperature or impurity composition change.
- There is no significant neoclassical tearing mode (NTM) activity as detected by correlation between signals from Mirnov coils placed in different toroidal positions. NTM activity causes significant heat and particle transport across the plasma which is not related to the physical processes investigated in this work [45]
- Experiments involving an artificial enhancement of the toroidal magnetic field ripple [46] were omitted.

Those shots were included into the database and all available diagnostic data were collected and stored. Relying on the collected measurements data, the following samples were excluded from consideration:

- shots without validated T_i or LIDAR measurements
- shots without manually validated FIR measurements (fringe jumps removed)
- shots without completed NBI particle deposition calculation
- shots with higher than 5% inconsistency between measured and reconstructed line integrated density over the 6 measurement chords (see section 2.4)

After the second stage of sample filtering, the database size was reduced to 269 entries, mostly due to unavailability of validated data from at least 5 FIR chords. The 5% inversion quality threshold was satisfied by 75% of shots, wherever the FIR data was available. All of the finally chosen samples had significant NBI heating, as well as some ICRH heating (in $\sim 50\%$ cases) and LHCD heating/current drive ($\sim 20\%$ cases). The ICRH was used in the minority ion heating scheme or via mode conversion [47], so it produced mostly electron heating, while NBI heating is naturally split between electrons and ions [48].

The combination of those heating methods allowed us to get a variety of T_i/T_e ratio and study its effect on the density profile behaviour. The LHCD current drive, which was used in some of those experiments, provided a variation of the internal inductance l_i – parameter

characterizing the broadness of current density profile (and thus of the q profile). $l_i = \frac{\overline{B_\theta^2}}{B_{\theta a}^2}$,

where $B_{\theta a}$ is the poloidal magnetic field magnitude at the edge, $\overline{B_\theta^2} = \frac{2}{a^2} \int_0^a B_\theta^2 r dr$ - poloidal

magnetic field averaged over the plasma cross-section.

For the density profile measurements, LIDAR and FIR diagnostics were used. FIR inversion was done with the technique described in section 2.4.1.

On figure 3.3.1 the comparison of density peaking and normalized density gradient at the mid-radius (R/L_n) obtained with both diagnostics is shown. We define density peaking as a ratio of the average electron density inside the $r/a=0.2$ surface to the volume averaged density. This is a common definition used in the most of publication and especially useful for the comparison of results obtained on different machines, since it is free of the plasma shape specifications.

The normalized density gradient is harder to define unambiguously, and local gradients are much harder to measure. But this local value (rather than global density peaking) defines the transport processes and must be used in the local simulations presented in chapter 4. We will base our analysis on both those values, defining the density gradient as a slope of linearly fitted part of the density profile between $r/a=0.2-0.8$ at the equatorial plane.

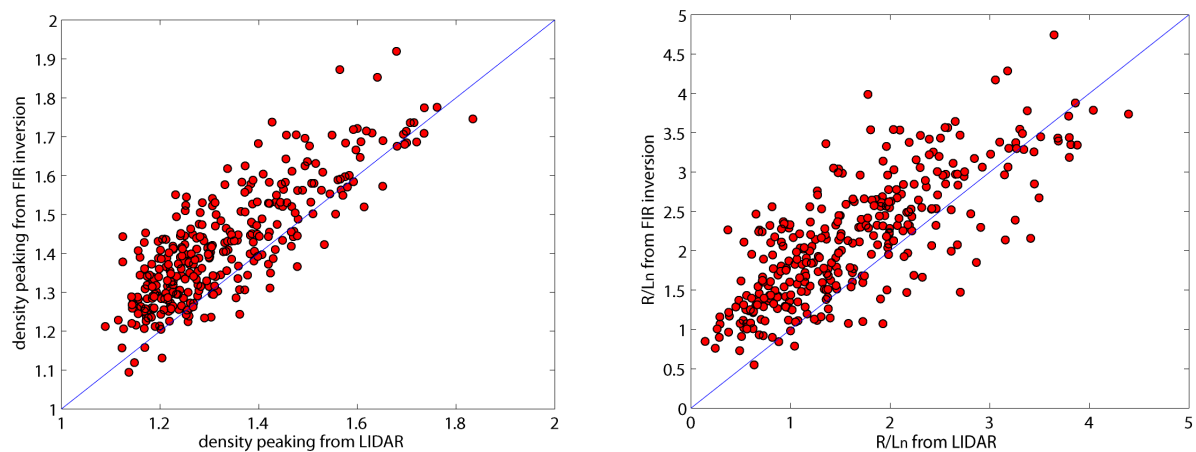


Figure 3.3.1. Comparison between LIDAR and interferometer density profile measurements ($n_{0.2}/\langle n_e \rangle$ for the left one, R/L_n at $r/a=0.5$ for the right one)

As one can see, there is a small discrepancy between two diagnostics for both $n_{0.2}/\langle n \rangle$ and R/L_n and it is similar to the one shown at figure 2.5.3 for the post LIDAR code correction case. The discrepancy remains constant for all types of density profile shape. For the statistical analysis presented in the next section, we will use only the FIR density measurement, keeping in mind that the final real values of peaking and density gradient in our conclusions can have a small systematic deviation, ~ 0.1 for $n_{e0}/\langle n_e \rangle$ and ~ 0.5 for R/L_n , which is however sufficiently smaller than the variation of density profile shape observed in our database. On Fig. 3.3.2 one can find an example of plasmas with high and low density peaking, measured during 2006-2007 campaigns, showing good agreement between the two diagnostics.

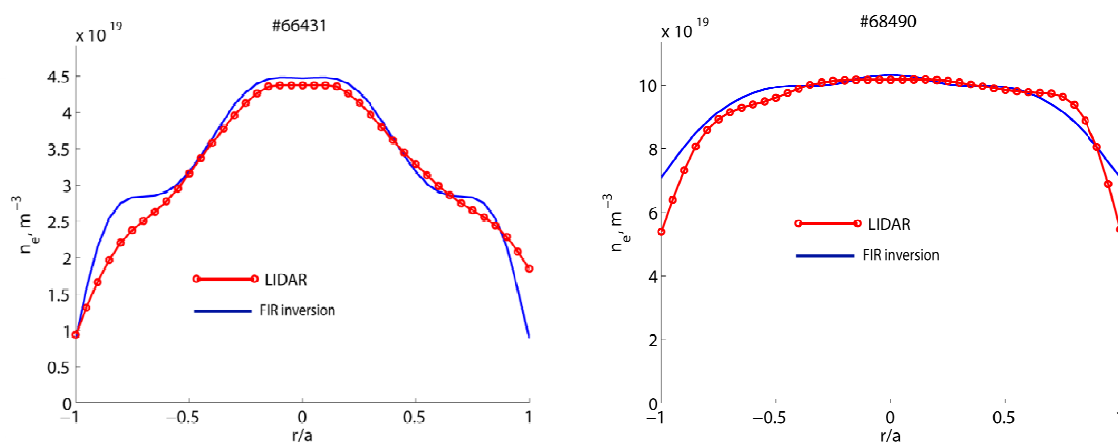


Figure 3.3.2 Examples of high peaking and low peaking density profile in 2 different JET shots, as measured by LIDAR and FIR inversion.

NBI power and particle deposition in the JET plasma core are calculated using the PENCIL code [49]. Calculations are routinely available for every shot, but PENCIL doesn't take into account penetrating edge neutrals nor halo neutrals which are born in the plasma core as a result of charge exchange of beam neutrals and thermal ions. More accurate calculations using TRANSP [50], including edge and halo neutrals, are available only for a limited number of discharges. Comparing the particle sources estimated by TRANSP and PENCIL inside the $r/a=0.5$ surface, we found that the difference does not exceed 20% and for all the existing cases with both code results available, NBI fuelling is significantly higher than penetration of neutrals from the edge to the central plasma region. On Fig. 3.3.3 one can find an example of particle depositions from both sources (this example is an extreme cases, where edge penetration is relatively high). The penetrating neutral's source rate decreases exponentially from the edge to the core, which is why we consider only the $r/a < 0.5$ region.

Nearer to the plasma boundary the contribution of edge neutrals fraction to the total particle source is more significant. For the database we therefore only use the NBI fuelling deposited inside $r/a < 0.5$ and calculated by the routine PENCIL code.

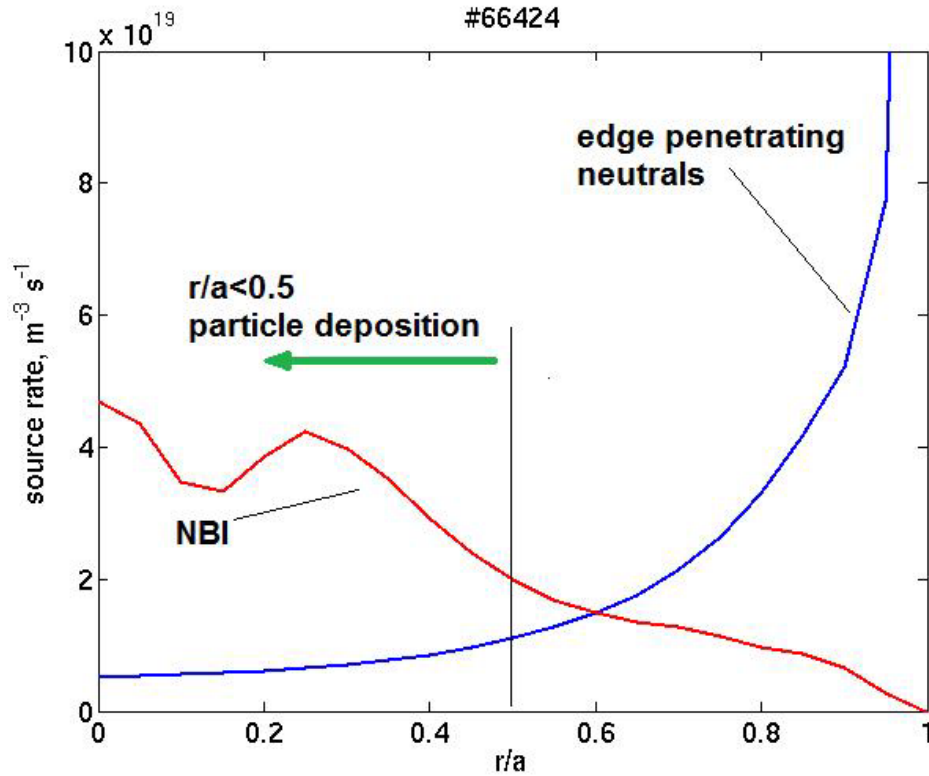


Figure 3.3.3: NBI particle deposition (PENCIL) versus edge penetrating neutrals (TRANSP) for the #66424 JET shot.

3.4 Experimental data analysis.

From previous studies [20-24] we know that the density peaking depends on the effective collisionality, ν_{eff} , which is defined as

$$\nu_{\text{eff}} = \nu_{ei} / \omega_d = \nu_{ei} / 2k_y \rho^* (c_s / R) = 10^{-14} Z_{\text{eff}} R n_e / \langle T_e \rangle^2 \quad (3.4.1)$$

where ν_{ei} is electron collisionality, ω_d is the curvature drift frequency, $\langle n_e \rangle$ and $\langle T_e \rangle$ are volume averaged electron density and temperature. The tendency of increasing peaking with decreasing of collisionality is also observed in the JET 2006-2007 H-mode dataset, as one can see on figure 3.4.1.

A noticeable feature of the collisionality dependence can be seen on figure 3.4.1: collisionality dependence appears to be saturating at some minimum value of density peaking or normalized density gradient R/L_n . There are two possible reasons of this behaviour: the first one is the limited diagnostics resolution for measuring the edge part of the density profile. The second one is a high particle source term near the plasma edge ($r/a > 0.7$) due to chain charge exchange of the neutral atoms coming from the boundary. This particle source helps in maintaining some finite density gradient near the plasma edge and is not allowing the peaking factor to drop below a certain value.

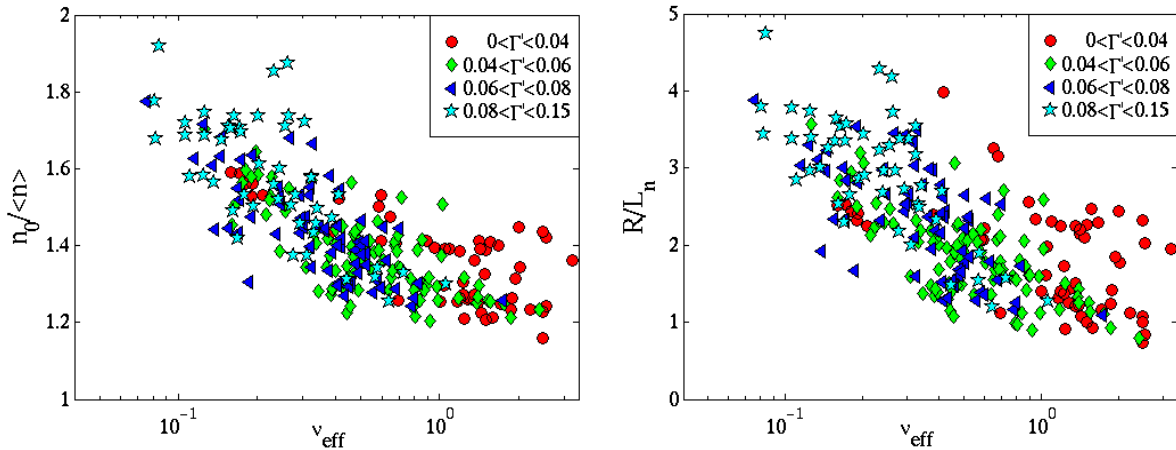


Figure 3.4.1: Density peaking (left) and normalized density gradient (right) as a function of the effective collisionality from interferometer measurements.

It was decided to limit the analysis to the low collisionality branch ($v_{\text{eff}} < 0.5$), which represents the monotonic $v_{\text{eff}}^{1/2}$ dependence. This domain is also relevant for ITER extrapolations, since the ITER plasma is expected to have low effective collisionality $v_{\text{eff}} < 0.2$. The database contains 150 samples in this low collisionality region.

In this work we use the square root of effective collisionality for deriving the empirical scaling laws, instead of $\ln(v_{\text{eff}})$ used in previous publications [20-24]. In the range of collisionalities considered in this work (0.2-0.5), relation between those two parameters is nearly linear, so there is no principal difference which one is used in the scaling. It was also found that $v_{\text{eff}}^{1/2}$ is more suitable for representing the GS2 simulation results, as it will be shown in chapter 4.

To investigate the parametric dependence of density profile shape, we've chosen a set of non-dimensional values which are used commonly for describing tokamak plasmas. The focus was put on the following 11 variables: v_{eff} , Γ' (particle flux normalized by ion heat flux at $r/a=0.5$), M (Toroidal Mach number), ρ^* (the normalized ion Larmor radius), T_i/T_e ,

q_{95} (safety factor at 95% of poloidal flux), β_N , R/L_{Te} , R/L_{Ti} , l_i (internal inductance obtained from magnetic measurements), and δ (triangularity at the last closed flux surface). Γ' is defined as $\Gamma' = eT_i S / Q_i$, where S ($1/m^2/s$) is the particle flux and Q_i (W/m^2) is the ion heat flux through the $r/a=0.5$ flux surface, e is the electron charge and T_i is the local ion temperature. Electron temperature is measured by LIDAR, and T_i – by the charge exchange diagnostic. For the database, the average values between $r/a=0.3-0.7$ are taken. Temperature gradients are calculated over $r/a=0.2-0.8$, the same manner as density gradient for R/L_n . The definition for Γ' differs from the definition for the dimensionless particle source term used in previous publications [22-23]. The reason of taking this one is that the comparison with the linear gyrokinetic simulations, described in the following chapter 4, becomes easier, since the ITG mode is widely believed to be responsible for the majority of the ion heat transport, while the electron heat may be transported as well through smaller scale instabilities (ETG modes).

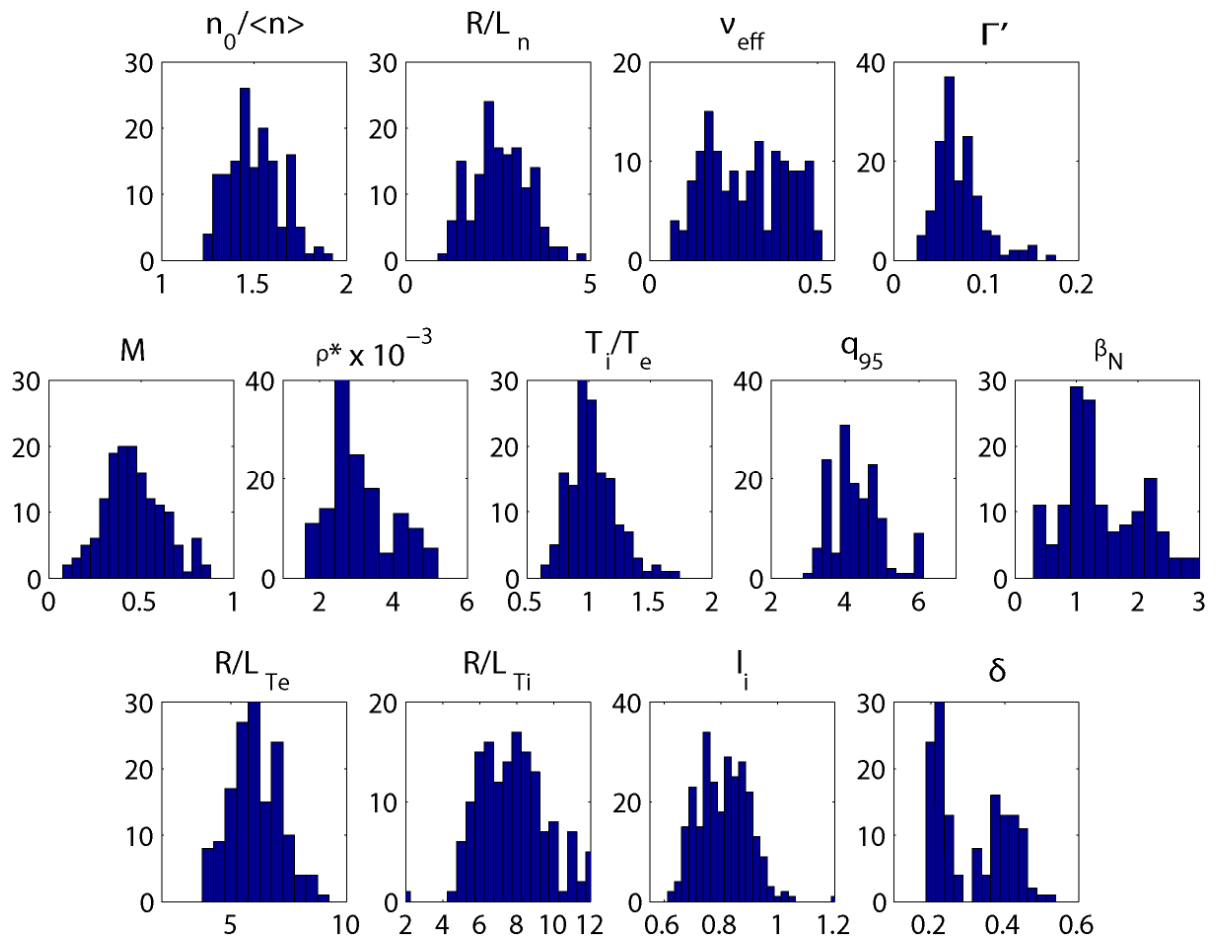


Figure 3.4.2: Number of observations per value for each of the dimensionless parameters in the experimental dataset ($v_{eff} < 0.5$)

On the figure 3.4.2 the variation of each of those parameters in our database is shown as histograms. Thanks to the diversity of the experimental conditions, each of the parameters is varied over a wide range.

To find a relationship between those parameters in our database, we've calculated the cross correlation coefficient between all of them, using the standard formula:

$$coeff = \frac{1}{N-1} \sum_{i=1..N} \frac{(A_i - \langle A \rangle)(B_i - \langle B \rangle)}{\sigma(A)\sigma(B)} \quad (3.4.2)$$

The results can be found on the table 3.4.1.

As it already noted, density peaking is strongly correlated with the effective collisionality (factor -0.71). Parameters Γ' , T_i/T_e and δ show a moderate correlation, β_N and l_i have the lowest (barely visible) correlation with density gradients and the other parameters (q_{95} , ρ^* , M , R/L_{Te} , R/L_{Ti}) are not relevant at all, confirming conclusions from an earlier dataset on JET, composed of 2000-2004 experiments [21-22].

Table 3.4.1: Cross correlation coefficients between various experimental parameters
($v_{eff} < 0.5$)

	$n_{02}/\langle n \rangle$	R/L_n	$v_{eff}^{1/2}$	Γ'	M	ρ^*	T_i/T_e	q_{95}	β_N	R/L_{Te}	R/L_{Ti}	l_i	δ
$n_{02}/\langle n \rangle$	1	0.92	-0.71	0.53	0.09	-0.13	0.4	-0.05	-0.36	-0.22	0.09	0.31	-0.52
R/L_n	0.92	1	-0.67	0.54	0.2	0.02	0.41	-0.15	-0.19	-0.08	0.08	0.3	-0.43
$v_{eff}^{1/2}$	-0.71	-0.67	1	-0.42	0.2	0.25	-0.23	0.13	0.5	0.25	-0.04	-0.27	0.69
Γ'	0.53	0.54	-0.42	1	0.56	0.24	0.93	0.05	0.06	-0.01	-0.22	-0.13	-0.16
M	0.09	0.2	0.2	0.56	1	0.64	0.67	0.09	0.61	-0.32	0.35	-0.49	0.4
ρ^*	-0.13	0.02	0.25	0.24	0.64	1	0.4	-0.41	0.88	0.48	-0.28	-0.52	0.58
T_i/T_e	0.4	0.41	-0.23	0.93	0.67	0.4	1	0.04	0.18	0.1	-0.19	-0.27	-0.03
q_{95}	-0.05	-0.15	0.13	0.05	0.09	-0.41	0.04	1	-0.21	-0.32	-0.2	-0.06	-0.06
β_N	-0.36	-0.19	0.5	0.06	0.61	0.88	0.18	-0.21	1	0.44	-0.42	-0.48	0.78
R/L_{Te}	-0.22	-0.08	0.25	-0.01	-0.32	0.48	0.1	-0.32	0.44	1	0.23	-0.01	0.37
R/L_{Ti}	0.09	0.08	-0.04	-0.22	0.35	-0.28	-0.19	-0.2	-0.42	0.23	1	0.54	-0.28
l_i	0.31	0.3	-0.27	-0.13	-0.49	-0.52	-0.27	-0.06	-0.48	-0.01	0.54	1	-0.45
δ	-0.52	-0.43	0.69	-0.16	0.4	0.58	-0.03	-0.06	0.78	0.37	-0.28	-0.45	1

For our research we focus on the parameters which show high and moderate correlation with density peaking. Those will be: $v_{eff}^{1/2}$, Γ' , T_i/T_e and δ . We also keep the internal inductance (l_i) in our analysis despite of the small correlation factor, since it was reported to be significant in L-mode plasmas [16].

Table 3.4.2: Mean values and standard deviations of scaling parameters.

	$v_{eff}^{1/2}$	Γ'	T_i/T_e	δ	l_i
$\langle \diamond \rangle$, mean value	0.53	0.071	1.03	0.30	0.79
σ , standard deviation	0.13	0.026	0.19	0.10	0.088

To investigate the relative impact of each of those values on the density profile shape we will construct multivariable regression fits of density peaking for all possible 2, 3 and 4 considered parameters combinations.

We use the linear fit in the form $Y=c+\sum((a_j\pm\sigma(a_j))\cdot X_j)$, where Y is the regressed variable, X_j are the regression variables (those listed in the table above), a_j are the regression coefficients and $\sigma(a_j)$ are the standard deviations of a_j and correspond to a 66% confidence interval. The results are shown on table 3.4.3. ‘‘RMS’’ represents the root mean square deviation between the fit values and database values. The single parameter fit with the lowest RMS error and the most significant regression variable ($a_j/\sigma(a_j)$) is $n_{0,2}/\langle n_e \rangle = (1.96 \pm 0.04) - (0.88 \pm 0.07)v_{\text{eff}}^{1/2}$. Two parameter fits with combinations of $\{v_{\text{eff}}^{1/2}; \Gamma'\}$ and $\{v_{\text{eff}}^{1/2}; T_i/T_e\}$ produce regressions of similar quality.

Table 3.4.3. Results of the linear regression fits for the density peaking.

One parameter fits for density peaking:

const	$(v_{\text{eff}})^{1/2}$	Γ'	T_i/T_e	δ	l_i	RMS
1.96±0.04	-0.88±0.07					0.100
1.29±0.02		2.93±0.38				0.121
1.20±0.06			0.30±0.05			0.131
1.74±0.03				-0.78±0.1		0.122
1.11±0.10					0.50±0.12	0.136

Two parameters fits for density peaking:

const	$(v_{\text{eff}})^{1/2}$	Γ'	T_i/T_e	δ	l_i	RMS
1.78±0.05	-0.74±0.07	1.58±0.32				0.093
1.74±0.05	-0.81±0.07		0.18±0.04			0.094
1.96±0.04	-0.85±0.10			-0.04±0.12		0.100
1.79±0.09	-0.84±0.07				0.19±0.09	0.099
1.58±0.08		6.67±1.01	-0.53±0.13			0.115
1.53±0.04		2.54±0.33		-0.67±0.09		0.103
0.79±0.09		3.2±0.34			0.62±0.1	0.108
1.44±0.06			0.28±0.05	-0.76±0.09		0.109
0.53±0.11			0.39±0.05		0.73±0.11	0.115
1.61±0.12				-0.72±0.12	0.15±0.12	0.121

Three parameters fits for density peaking:

const	$(v_{\text{eff}})^{1/2}$	Γ'	T_i/T_e	δ	l_i	RMS
1.78±0.07	-0.73±0.08	1.78±0.98	-0.03±0.12			0.093
1.77±0.05	-0.63±0.10	1.68±0.32		-0.16±0.11		0.092
1.43±0.10	-0.63±0.07	1.92±0.32			0.34±0.09	0.089
1.64±0.07		4.43±0.96	-0.26±0.13	-0.61±0.09		0.102
0.98±0.14		4.84±1.02	-0.24±0.14		0.53±0.11	0.107
1.73±0.06	-0.72±0.10		0.19±0.04	-0.15±0.11		0.093
1.00±0.13			0.34±0.05	-0.58±0.10	0.42±0.11	0.104
1.78±0.10	-0.87±0.10			0.05±0.13	0.21±0.1	0.099
1.31±0.12	-0.70±0.07		0.25±0.04		0.39±0.09	0.089
1.00±0.13			0.34±0.05	-0.58±0.10	0.42±0.11	0.104

Four parameters fits for density peaking:

const	$(v_{\text{eff}})^{1/2}$	Γ'	T_i/T_e	δ	l_i	RMS
1.29±0.15		3.78±0.97	-0.14±0.13	-0.50±0.10	0.31±0.11	0.100
1.30±0.12	-0.71±0.09		0.25±0.04	0.01±0.12	0.40±0.10	0.089
1.44±0.11	-0.62±0.10	1.91±0.32		-0.02±0.12	0.33±0.09	0.089
1.35±0.13	-0.66±0.08	0.93±0.96	0.13±0.12		0.37±0.09	0.089
1.77±0.07	-0.63±0.11	1.87±0.98	-0.03±0.12	-0.16±0.11		0.092

This can be understood from the high degree of correlation between Γ' and T_i/T_e observed (a coefficient of 0.93 in the table 3.4.1, the highest number obtained). The reason of such a high correlation is in the properties of electron and ion heating produced by thermalizing NBI injected particles.

In our definition, $\Gamma' = S/Q_i T_i$, S represents the total particle flux and Q_i is the total ion heat flux through the $r/a=0.5$ surface. For all cases considered in our database, the majority of particles delivered inside the $r/a=0.5$ surface are produced by neutral beams, and the ion heating is provided mainly by NBI. Although the equipartition heat flux between electrons and ions is taken into account for calculating Q_i , it is less than 20% of the NBI ion heating for all the cases in our database except very few which do not affect the overall statistics significantly. So, according to [48], we can write:

$$\frac{Q_i}{S} \sim \frac{Q_i}{(Q_i + Q_e)} = \frac{E_{\text{crit}}}{E_{\text{beam}}} \int_0^{E_{\text{beam}}/E_{\text{crit}}} \frac{dy}{1+y^{3/2}} \quad (3.4.3)$$

where E_{beam} is the energy of the neutral beam particles and E_{crit} is so called critical energy:

$$E_{crit} = 14.8 T_e \left[\frac{A^{3/2}}{n_e} \sum \frac{n_j Z_j^2}{A_j} \right]^{2/3} \sim 20 \cdot T_e \quad (3.4.4)$$

Beam particles energy can be estimated as 100keV (there are two types of injectors, 85keV and 120keV). The particle source term Γ' turns into:

$$\Gamma' = \frac{S}{Q_i} T_i \sim \frac{Q_i + Q_e}{Q_i} T_i \sim (1 + 0.45 \frac{E_{beam}}{E_{crit}}) T_i \sim T_i + 2.25 \frac{T_i}{T_e}, \quad T_i \text{ is in keV} \quad (3.4.5)$$

In our database, T_i/T_e itself is moderately correlated with T_i :

$$T_i (keV) \approx -2.1 + 4.4 \frac{T_i}{T_e}, \quad \text{RMS} \sim 25\% \quad (3.4.6)$$

The sum of moderately correlated T_i and T_i/T_e produces a value (which is Γ') with a very high correlation with T_i/T_e (RMS~5%)

As a consequence, regressions which include T_i/T_e and Γ' together in this dataset are not relevant, since one of these parameters (or both) loses its statistical significance. Including only one of the two generally increases the quality of the fit. We conclude that at least one of these parameters is important for the density peaking, but it's impossible to decorrelate them in this particular database, since one would need discharges with dominant electron heating (or ion heating of other than NBI nature). For the experiments considered in this work, there are no such data, unfortunately.

In spite of a relatively high correlation between density peaking and plasma triangularity (δ), inclusion of it together with collisionality zeroes the statistical significance of the former in all of the 2, 3 and 4 parameter fits. We can conclude that the correlation between δ and $n_0/\langle n \rangle$ is mainly due to the correlation between δ and the effective collisionality (factor 0.69 in table 3.4.1). This correlation comes from the plasma operational scenario specifications, since high triangularity plasma shape was often used for high density and high collisionality cases, while low triangularity shapes were giving access to lower densities and, as a consequence, higher temperatures and lower collisionality plasmas. Thus in this work we exclude plasma shaping from the consideration.

Among the three-parameter fits the best ones combine $\{v_{eff}^{1/2}, \Gamma', l_i\}$ and $\{v_{eff}^{1/2}, T_i/T_e, l_i\}$. The internal inductance is statistically significant in all cases with a regression coefficient in the range ~0.3-0.4. We can conclude that in our dataset l_i does have a modest effect on density peaking.

All four-parameter combination fits contain either the $v_{\text{eff}}^{1/2} - \delta$ or the $\Gamma' - T_i/T_e$ pairs, so in each of those cases at least one of the parameters has low statistical significance. For that reason we will not be considering four-parameter regression fits.

Finally we only retain the following five scaling expressions for the density peaking:

$$\begin{aligned}
 n_{0,2}/\langle n_e \rangle &= 1.96 \pm 0.04 - (0.88 \pm 0.07) v_{\text{eff}}^{1/2} \\
 n_{0,2}/\langle n_e \rangle &= 1.78 \pm 0.05 - (0.74 \pm 0.07) v_{\text{eff}}^{1/2} + (1.58 \pm 0.32) \Gamma' \\
 n_{0,2}/\langle n_e \rangle &= 1.74 \pm 0.05 - (0.81 \pm 0.07) v_{\text{eff}}^{1/2} + (0.18 \pm 0.04) T_i/T_e \\
 n_{0,2}/\langle n_e \rangle &= 1.43 \pm 0.10 - (0.63 \pm 0.07) v_{\text{eff}}^{1/2} + (1.92 \pm 0.32) \Gamma' + (0.34 \pm 0.09) l_i \\
 n_{0,2}/\langle n_e \rangle &= 1.31 \pm 0.12 - (0.70 \pm 0.07) v_{\text{eff}}^{1/2} + (0.25 \pm 0.04) T_i/T_e + (0.39 \pm 0.09) l_i
 \end{aligned} \tag{3.4.7}$$

Doing the same regression exercise for the normalized density gradient gives us:

$$\begin{aligned}
 R/L_n &= 4.59 \pm 0.21 - (3.95 \pm 0.38) v_{\text{eff}}^{1/2} \\
 R/L_n &= 3.33 \pm 0.27 - (2.99 \pm 0.38) v_{\text{eff}}^{1/2} + (10.6 \pm 1.7) \Gamma' \\
 R/L_n &= 3.07 \pm 0.33 - (3.47 \pm 0.36) v_{\text{eff}}^{1/2} + (1.23 \pm 0.21) T_i/T_e \\
 R/L_n &= 2.32 \pm 0.56 - (2.69 \pm 0.40) v_{\text{eff}}^{1/2} + (11.59 \pm 1.75) \Gamma' + (0.99 \pm 0.49) l_i \\
 R/L_n &= 1.67 \pm 0.64 - (3.12 \pm 0.38) v_{\text{eff}}^{1/2} + (1.44 \pm 0.23) T_i/T_e + (1.28 \pm 0.51) l_i
 \end{aligned} \tag{3.4.8}$$

As it was already stated in the previous section 3.3, statistical analysis of the JET data was done using only interferometer data, keeping in mind that independent LIDAR measurements of density profile is in general agreement with FIR inversion (Fig 3.3.1). As an independent check of this statement, we reproduce regression fit (3.4.8), using only LIDAR measurements of density gradient.

$$\begin{aligned}
 R/L_n &= 4.52 \pm 0.23 - (4.47 \pm 0.42) v_{\text{eff}}^{1/2} \\
 R/L_n &= 3.19 \pm 0.30 - (3.46 \pm 0.41) v_{\text{eff}}^{1/2} + (11.6 \pm 1.9) \Gamma' \\
 R/L_n &= 2.09 \pm 0.36 - (3.97 \pm 0.40) v_{\text{eff}}^{1/2} + (1.30 \pm 0.23) T_i/T_e \\
 R/L_n &= 1.31 \pm 0.60 - (2.90 \pm 0.43) v_{\text{eff}}^{1/2} + (13.03 \pm 1.87) \Gamma' + (1.85 \pm 0.52) l_i \\
 R/L_n &= 0.48 \pm 0.68 - (3.37 \pm 0.40) v_{\text{eff}}^{1/2} + (1.66 \pm 0.24) T_i/T_e + (2.20 \pm 0.53) l_i
 \end{aligned} \tag{3.4.9}$$

We can see that the general conclusion expressed in previous section is basically confirmed. Confidence intervals of the fit with LIDAR data are slightly higher, due to somewhat higher error bars on density profile measurements, and the resulted gradients are a bit lower, as can be seen on Fig. 3.3.1 and Fig 2.5.3. Although the fit coefficients for all regression parameters are reproduced within their confidence intervals, which leaves our main conclusions

untouched. For future references, only the fit (3.4.8), produced with the interferometer data, will be used.

3.5 Conclusions and summary.

In this empirical study we've confirmed most of the observations reported in previous investigations [22-23]: effective collisionality has the strongest effect on density profile shape, Γ' and/or T_i/T_e have a minor effect and the parameters ρ^* , q_{95} , M , R/L_{Te} , R/L_{Ti} , and β_N , have no significant effect on the density peaking.

For the first time a small but consistent effect of the internal inductance was found in H-mode plasmas.

The influence of the particle source and temperature ratio on the density peaking must be treated with care, keeping in mind their strong cross-dependence, which can be described by the following fits:

$$\Gamma' = - (0.027 \pm 0.008) - (0.045 \pm 0.009) v_{\text{eff}}^{1/2} + (0.118 \pm 0.006) T_i/T_e \quad (3.5.1)$$

$$T_i/T_e = (0.34 \pm 0.06) + (0.30 \pm 0.08) v_{\text{eff}}^{1/2} + (7.58 \pm 0.36) \Gamma'$$

Using our derived scaling expressions, we can make a prediction for the ITER plasma condition. This condition is usually described as $\Gamma'=0$, i.e. no particles penetrate into the core due to the machine size, and $T_i/T_e=1$, i.e. electrons and ions are thermally equilibrated as a result of relatively high plasma density and machine size. Electron density and temperature were estimated by different models and for different operating scenarios in [51]. We will use $\langle n_e \rangle = 10^{20} \text{ m}^{-3}$, $\langle T_e \rangle = 8 \text{ keV}$, which is representative for the inductive baseline scenario. That gives us $v_{\text{eff}}(\text{ITER}) \sim 0.19$ leading to the extrapolations: $n_{0,2}/\langle n_e \rangle(\text{ITER})$ in the range 1.42 – 1.55, $R/L_n(\text{ITER})$ in the range 2.0 – 2.8, depending which of the derived scaling expressions is used. As one can see, the empirical analysis of the JET data suggests a moderately peaked density profile in ITER, even without a core particle sources.

The expected density peaking factor for the ITER plasma is also in agreement with the observations done on other machines and earlier on JET 2000-2004 database [20-24]. Predicted R/L_n value in this thesis work is although lower. The reason for that most probably lies in the definition of the density gradient, which is not unambiguous as it was stated already at the beginning of this chapter. Density profiles in tokamaks are usually not monotonic, and defining the averaging range for the gradient calculation should affect the result. In this work we used a linear fit over a relatively wide range of the density profile

($r/a=0.2-0.8$), which is often overlapping with the central relatively flat region. So in average, the density gradient calculated that way can be lower than one calculated over a shorter stretch, as in [22].

CHAPTER 4

Plasma microturbulence and linear gyrokinetic simulations, comparison with the experiment.

4.1 Introduction.

As already mentioned in the introductory chapter, transport processes in tokamak plasma cannot be described by means of the neoclassical theory only. Neoclassical theory [10] provides a baseline level for the transport coefficients, but turbulent, or anomalous processes usually dominate.

Turbulent processes in plasmas may be broadly divided into two different categories: macroscale and microscale ones. Macroinstabilities are characterized by relatively large scales of plasma displacements (much larger than ion Larmor radius) and usually can be described by fluid models, for example very widely used the magnetohydrodynamic (MHD) model. They include many different types of ideal and resistive MHD instabilities which can be found in tokamaks (ballooning, tearing and kink modes for example [3]).

The most common macroinstabilities in tokamaks are sawteeth oscillations [52], ELMs (Edge Localized Modes [53]) and magnetic islands or (neoclassical) tearing modes [45].

The sawtooth instability is a periodic redistribution of plasma current and loss of plasma energy from inside $q=1$ surface, which is characterized by very distinctive ECE and X-ray emission traces. ELMs are periodic disruptions of the edge transport barrier in H-mode plasmas. Tearing modes are responsible for the formation of so-called magnetic islands on rational magnetic surfaces. When neighboring magnetic islands are large enough to overlap, they may lead to local stochastisation of the magnetic flux surfaces and increased transport.

4.2 Microinstabilities.

Microinstabilities are characterized by spatial scales comparable to the ion Larmor radius. In this work we shall investigate the role of the most important type of microinstabilities – drift wave instabilities [54,55] on the particle transport. Contrary to the macroscale turbulence, these instabilities do not cause a significant distortion of magnetic field configuration. Even

neglecting the small fluctuations of the magnetic field at all preserves the most important features of these instabilities. Such an approximation is called electrostatic.

Transport of particles and energy in drift modes is caused by the $\mathbf{E} \times \mathbf{B}$ local drift vortices, where \mathbf{B} is the confining magnetic field, and \mathbf{E} is the perturbed electrical field. A simple visualization of a drift wave mode is shown on figure 4.2.1.

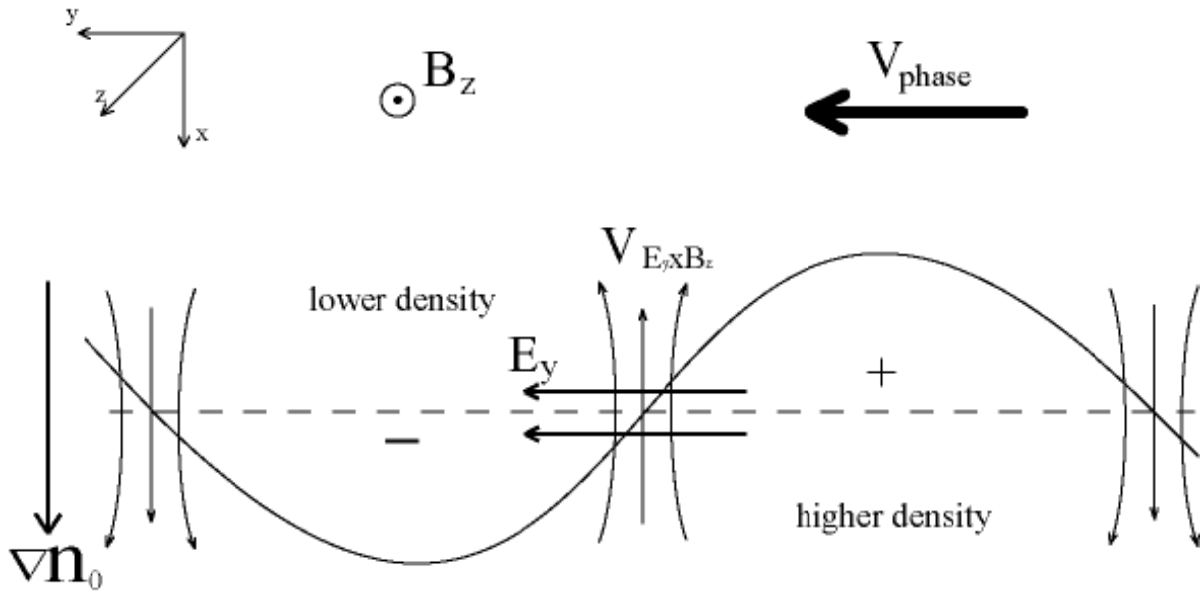


Figure 4.2.1: Drift wave in the presence of a density gradient.

Let's assume we have plasma in a strong magnetic field $\mathbf{B} \cdot \mathbf{z}$, with a density gradient in the x direction. We consider a density perturbation in a form of a plane wave $\delta n \sim \exp(ik_y \cdot y)$ along the y axis. Any deviation of the ion density from the mean value is compensated by the electrons moving along the magnetic field lines in the z direction, thus the principle of *quasineutrality* applies: $Z_i n_i \sim n_e$, which is valid up to the order of $(\lambda_D / \delta x)^2$, where $\lambda_D = (T / 4\pi m e^2)^{1/2}$ is the Debye length, and δx – characteristic spatial scale. The small residual difference in electron and ion density produces a local potential, which in our conditions is connected with the density fluctuations by the Boltzman distribution function:

$$Z_i n_i \sim n_e = n_0 \exp\left(\frac{e\tilde{\phi}}{T_e}\right) \quad (4.2.1)$$

where n_0 is the unperturbed density. So, fluctuations of the ion density produce corresponding fluctuations of the electrostatic potential. The successive positive and negative potential fluctuations along the y axis are responsible for the electrical field \mathbf{E}_y . Together with the strong confining magnetic field \mathbf{B}_z , this produces the $\mathbf{E}_y \times \mathbf{B}_z$ plasma oscillating drift across the magnetic field lines. On figure 4.2.1 this motion is directed

upwards, thus moving higher density plasma into a lower density region. On a fixed flux surface, shown as a dashed line on the figure 4.2.1, this will result in a propagation of the excess density hump, denoted as “+”, to the left, in the direction of the electron diamagnetic drift. The dispersion relation for the drift wave in its simplest form is:

$$\omega \equiv \omega_* = \frac{k_y T_e}{e B_0 l_n} \quad (4.2.2)$$

where $l_n = n / \nabla n$ is the density gradient length, ω_* is the drift frequency.

Equation 4.2.1 is valid in case of an ideal adiabatic electron response. In the reality however the electron motion along magnetic field lines is slightly impeded by the electron-ion collisions and magnetic mirror trapping. This results in a phase shift between density perturbation \tilde{n} and the electrostatic potential $\tilde{\phi}$, in a way that the potential maximum always lags behind the density maximum in their movement along the y axis. Thus at the location of the $\max(\tilde{n})$ there is still a plasma ExB motion in the direction opposite to the density gradient, so that the density fluctuation becomes even higher, causing an increase of the potential fluctuation and amplification of the mode. The drift wave becomes unstable. Such instability in tokamaks is called the Trapped Electron Mode, due to the main reason of the electron response delay.

Now let's take a look into a bit different situation: plasma with zero density gradient and a finite ion temperature gradient.

As before, we consider an ion density perturbation in the form of a plane wave propagating in y direction. By analogy with the previous case, the perturbed density summons up the perturbed potential, which gives rise to the electrical field E_y and plasma drift across magnetic field lines.

$$\vec{v}_\perp = -c \frac{\nabla \tilde{\phi} \times \vec{z}}{B_0} \quad (4.2.3)$$

This motion is incompressible ($\nabla \cdot \vec{v}_\perp = 0$), so it does not change the local density at the central point on figure 4.2.2, since $\nabla n_0 = 0$. But at the same time it brings hotter, i.e. higher pressure plasma there, which will experience a thermal expansion in the z direction, consequently decreasing the local density. Similarly, on the right and left sides of figure 4.2.2, the ExB drift will bring lower pressure plasma to this flux surface, which will experience parallel compression, increasing the local density. The resulting drift wave will be propagating to the right, in the ion diamagnetic drift direction, opposite to the previous TEM case. This type of the drift wave mode, called the Ion Temperature Gradient mode

[56], is unstable intrinsically, due to the inertia of the parallel ion motion, which always causes a lag between the the local density and the parallel ion velocity.

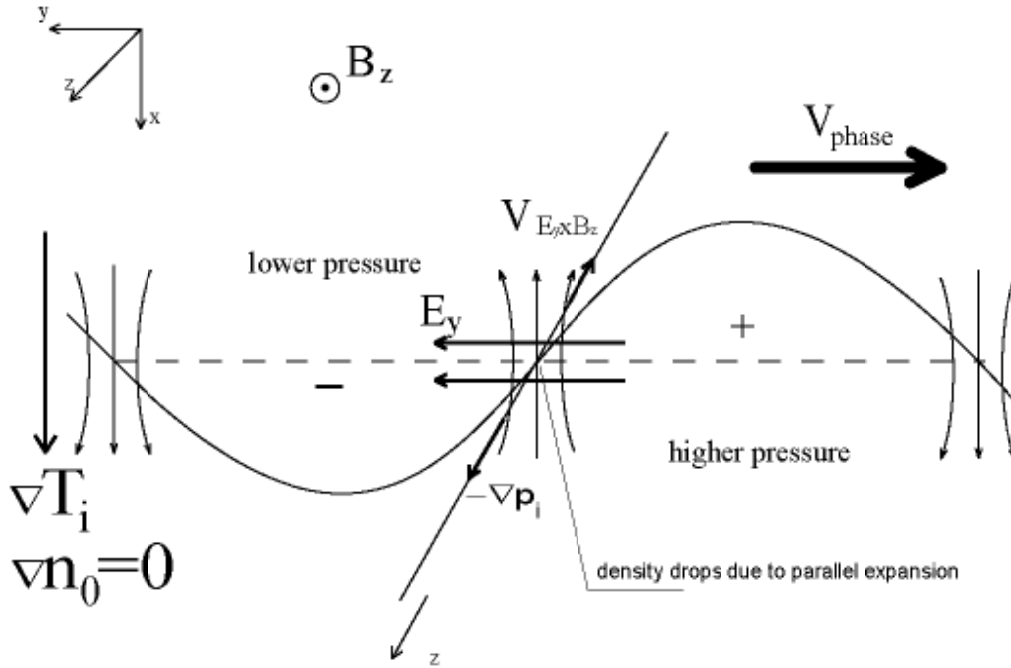


Figure 4.2.2: Drift wave in a plasma with an ion temperature gradient.

In the general case we usually have to deal with both $\nabla T_i > 0$ and $\nabla n_0 > 0$. In such a situation, the type of the instability depends on which of the processes, density change due to parallel compression or due to plasma $\mathbf{E} \times \mathbf{B}$ movement along the density gradient direction, dominates. A rough estimation [55,57] for the ITG stability threshold is given by

$$\eta_i \equiv \frac{d \ln(T_{i0})}{d \ln(n_0)} > \frac{2}{3} \quad (4.2.4)$$

As one can see, drift waves enhance particle and heat diffusivity, since they produce plasma oscillations in the x direction, which are followed by dissipation along the magnetic field lines. In addition to that, as was already stated before, potential fluctuations can lag behind the density fluctuations due to somewhat impeded electron response, giving rise to an additional convective (not directly related to the density gradient value) particle flow $v = \int \tilde{n} \tilde{v}_\perp dS$. Here $\int dS$ denotes an integral over a flux surface, \tilde{n} - density fluctuations, \tilde{v}_\perp - plasma flow across the magnetic field due to potential fluctuations and corresponding $\mathbf{E} \times \mathbf{B}$ drift.

For example, a small delay between the potential maximum and the density maximum in the case of the TEM (figure 4.2.1) causes an outwards shift of the fluctuating density, while in

the ITG case, since the direction of mode propagation changes to the opposite, the overall density shift will be directed inwards, towards the region of higher T_i .

The slab mode examples shown above describe the very basics of the physical processes which occurs in drift wave turbulence. To evaluate the real characteristics of the turbulence, including the diffusive and convective fluxes, one has to solve numerically the full non-linear kinetic equations in the real toroidal geometry conditions.

4.3 Gyrokinetics and the GS2 code.

The behaviour of each plasma species can be described by the Vlasov equation:

$$\frac{\partial f}{\partial t} + \bar{v} \cdot \nabla f + \dot{\bar{v}} \cdot \frac{\partial f}{\partial \bar{v}} = C(f) \quad (4.3.1)$$

where $f = f(\bar{x}, \bar{v})$ is the distribution function, \bar{v} is the particle velocity, $\dot{\bar{v}} = \frac{q}{m} (\bar{E} + \frac{\bar{v} \times \bar{B}}{c})$ is the particle acceleration under the effect of the Lorentz force, $C(f)$ is the collision operator. Solving the Vlasov equation together with Maxwell's equations for the electromagnetic field (the whole system is often referred to as Vlasov-Maxwell equations) will allow us to predict plasma properties in any condition. Unfortunately, a full solution of this system of equations is hardly possible with the current state-of-art accessible computational power, due to the number of variables involved and the large range of time scales of different processes which have to be resolved simultaneously (for example fast electron gyromotion and slow ion drift).

In the plasma conditions of our interest however, this system of equations can be simplified [58-60] by expanding a particle's movement into three components as it shown on figure 4.3.1 and averaging the distribution function over the fast cyclotron motion (rotation of a charged particle in a plane perpendicular to a strong magnetic field). Such an approximation can be used if the following conditions are fulfilled:

$$\frac{\tilde{f}}{f_0} \sim \frac{e\tilde{\phi}}{T} \sim \frac{\tilde{A}_{\parallel}}{B\rho} \sim \frac{\omega}{\Omega} \sim \frac{\rho}{L} \ll 1 \quad (4.3.2)$$

where \tilde{f} is the perturbed distribution function, f_0 is the equilibrium distribution function, B is the equilibrium magnetic field, L is the characteristic scale length of the system, Ω and ρ are the cyclotron frequency and gyroradius of a given particle species, $\tilde{\phi}$ and \tilde{A}_{\parallel} are the perturbed electrostatic and parallel vector potential.

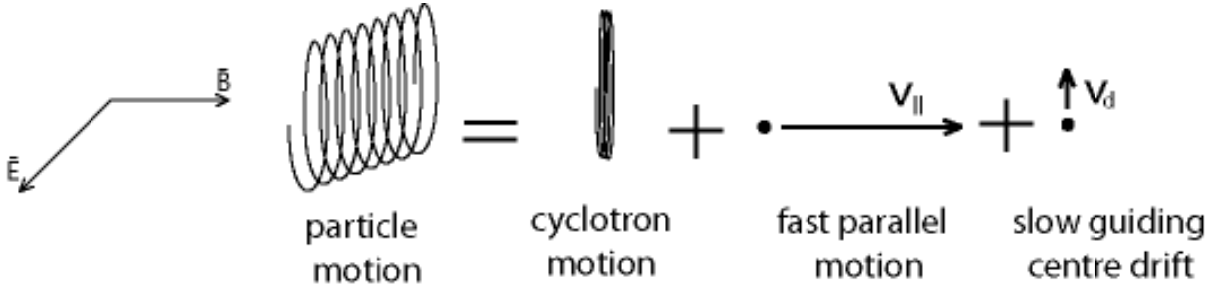


Figure 4.3.1: Three components of a particle motion in a strong magnetic field.

In the gyrokinetic approximation the particle coordinate vector is replaced by the guiding center coordinate vector:

$$\vec{R} = \vec{x} + \frac{1}{\Omega} \vec{v} \times \frac{\vec{B}}{|B|} \quad (4.3.3)$$

and the particle velocity is represented by two components: parallel and perpendicular to the confining magnetic field. v_{\parallel} and v_{\perp} are also can be replaced by kinetic energy and magnetic moment:

$$E = \frac{1}{2} m(v_{\parallel}^2 + v_{\perp}^2), \quad \mu = \frac{mv_{\perp}^2}{2B_0} \quad (4.3.4)$$

The gyrokinetic equations for those new variables were derived in [58, 61] for example. Implementing the gyrokinetic averaging reduces the number of variables to 5, also it removes the necessity to resolve particles' cyclotron motion in numerical calculations, thus allowing a significant increase of the time step size. That reduces the computational power requirements and makes the gyroaveraged Vlasov-Maxwell equations solvable by modern computers in a reasonable time.

As an alternative approach, the GLF (Gyro-Landau-Fluid) model is widely used for simulations of ITG/TEM turbulence in tokamaks. It represents a “half-way” between fully kinetic and fluid descriptions, which from one hand facilitates (and accelerates) numerical calculations through simplifying the task, and at the same time keeps certain kinetic effects (such as Landau damping). The model applies fluid approach to ions and passing electrons, while treating the trapped electrons separately, thus being able to reproduce non-adiabatic response of the electrons and successfully simulate ITG/TEM turbulence in a simpler manner, comparing to kinetic solutions. More detailed description of GLF model and GLF23 code can be found in [97-98].

GLF is widely used for heat transport simulations, but is not ideally suitable for our purposes, since particle transport requires precise kinetic calculations of the parallel response of both electrons and ions, so for the simulations produced in this work we have chosen the fully (gyro)kinetic approach.

There are numerous gyrokinetic codes, linear and non-linear, local and global. For the simulations done here the GS2 code was used.

The GS2 code [62-64] was developed by W. Dorland and M. Kotschenreuther. It calculates the nonlinear evolution of the perturbed distribution function and the electrostatic potential in full electromagnetic approach (keeping δB_{\parallel} and δB_{\perp}) by solving the gyrokinetic Vlasov-Maxwell equations in a local flux-tube geometry. In this work we will not use the full potential of the GS2 code, limiting it to the electrostatic linear mode stability analysis. In such a regime, the amount of the computational power required for a single case analysis is relatively small, so it was affordable to complete a large number of simulations (over one thousand) to investigate the dependencies on a variety of input parameters.

The source code is open for public and can be found online at <http://gs2.sourceforge.net>

4.4 Linear simulations for the JET H-mode plasma conditions.

To elaborate the role of microturbulence in the density profile formation, a set of linear electrostatic GS2 calculations was performed. The primary purpose of the simulations was the investigation of the density gradient response to the following parameters: electron collisionality, ion to electron temperature ratio, particle flux (which represents the core particle sources in experiment) and the local shear value, i.e. the parameters which were found to be important for the density peaking in the empirical analysis of the JET experimental data, discussed in Chapter 3. The dependence on the ion temperature gradient was investigated also, since ITG was the most representative mode in our simulations, and investigation of its dependence on the density gradient separately from the ion temperature gradient would be injudicious.

All the simulations were done for the mid-radius flux surface $r/a=0.5$. The Miller [65] description of the equilibrium was used, with the following parameters:

$$R_{\text{maj}}=1.0, R_{\text{geo}}=0.947, q=1.5, \hat{s}=0.45, \kappa=1.45, \kappa'=0.1, \delta=0.12, \delta'=0.06, \Delta'=-0.21$$

Here R_{maj} is the radius of the flux surface axis, R_{geo} is the magnetic axis position,

$$q = \frac{d\Phi}{d\Psi} \cong \frac{B_{tor}}{B_{pol}} \frac{r}{R} \frac{1}{2} (\kappa^2 + 1) - \text{safety factor}, \quad \hat{s} = \frac{dq}{dr} \frac{r}{q} - \text{local magnetic shear value}, \quad \kappa - \text{the flux}$$

surface elongation, $\kappa' = \frac{d\kappa}{d\rho}$ - elongation derivative (ρ - minor radius), δ - the flux surface

triangularity, $\delta' = \frac{d\delta}{d\rho}$, $\Delta' = \frac{dR_{maj}}{d\rho}$ - Shafranov shift gradient. All the input values are

normalized to a reference length, which can be chosen arbitrarily. In these simulations, the major radius was used as a reference length, that's why $R_{maj}=1.0$ in the input data.

Those geometry parameters were fixed for all of the simulations runs. They do not match any specific experiment, but they are typical of the JET plasma shape. The local shear value was fixed for the first group of simulations, where the effect of T_i/T_e , R/L_n , R/L_{Ti} and collisionality were investigated. Simulations with different local shear values were done separately.

In addition to the shape, the $R/L_{Te}=6.0$ parameter was also kept constant. The other four input parameters were varied in steps:

$T_i = 0.75, 0.85, 1.0, 1.15$ (which is equal to T_i/T_e since in our normalization $T_e=1.0$ always)

$R/L_n = 1.0, 1.8, 2.3, 2.8, 3.2$

$R/L_{Ti} = 6.0, 7.0, 8.0, 9.0$

$\nu_{eff} = 0.04, 0.054, 0.074, 0.095, 0.125, 0.146, 0.173, 0.208, 0.255, 0.32, 0.415, 0.56, 0.797$

The collisionality value ν_{eff} here is the ‘‘effective collisionality’’ which was defined in the chapter 3 as the electron collisionality normalized by the ion drift frequency. In fact the GS2 code uses the normalization to the reference time value, which is equal to the time which takes a reference particle at a reference energy value to pass a reference distance. For the normalizations chosen in these simulations (distance = R , energy= T_e , mass= m_{ion}), the

definition of collisionality in the GS2 frame is $\nu_{GS2} = \nu_{ei} \left(\frac{2T_e}{R^2 m_{ion}} \right)^{-1/2}$. This definition

differs from the ν_{eff} definition by a factor of $\sqrt{0.2}$. Another difference arises from the fact that in the empirical database we used volume averaged $\langle n_e \rangle$ and $\langle T_e \rangle$, while in the simulations we assume the local values at $r/a=0.5$. The local and volume average effective collisionalities in the JET empirical database are very well correlated and differ by a factor of ~ 0.43 : $\nu_{r/a=0.5} \approx 0.43 \nu_{eff}$, which gives the final expression for conversion from GS2 to JET collisionality: $\nu_{GS2} = 0.192 \nu_{eff}$. To avoid confusions, only the values of the effective

collisionality ν_{eff} will be used in this work, the reader should keep in mind that the corresponding collisionality values in the GS2 input are smaller by a factor of $0.43 \cdot \sqrt{0.2} = 0.192$

Independent variation of the above parameters resulted in 1040 separate GS2 runs, which were executed on the EPFL hosted high performance computing cluster PLEIADES2 [66-67]. In each of the runs, calculations for 10 different mode numbers were done: $k_y \rho_s = 0.1, 0.2, \dots, 1.0$, but only the fastest linear growth rate mode was considered. The $\max(\gamma)$ mode number varied between $k_y \rho_s = 0.3$ and 0.6 for different input parameters. Typical spectrum for mode frequency and growth rates can be found of Fig. 4.4.1. With only slight deviations, it is reproduced in all the simulations done in this work for the JET case.

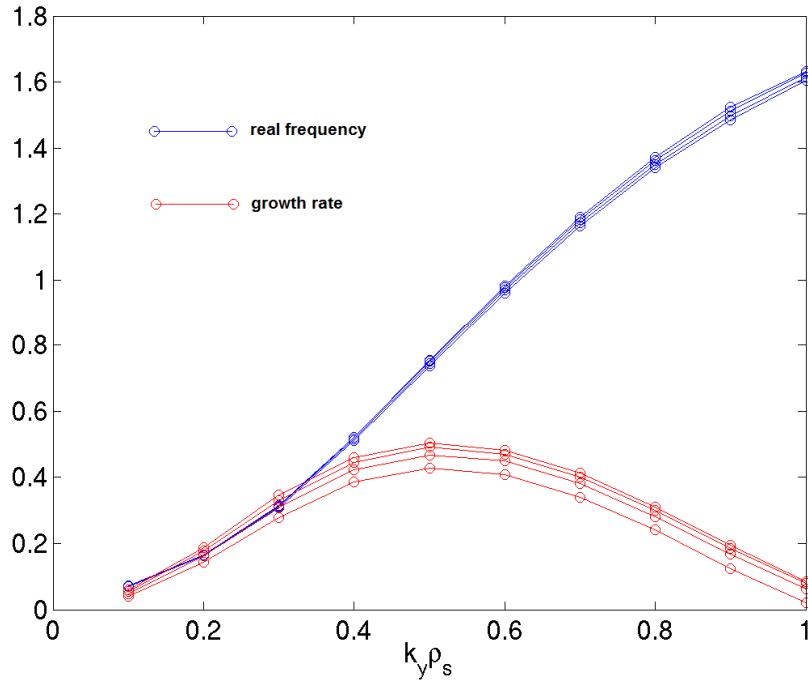


Figure 4.4.1: Typical real frequency $\text{Re}(\omega)$ and linear growth rate $\text{Im}(\omega)$ in GS2 output for the parameters used in the scan. Here $T_i/T_e=1.0$, $R/L_n=2.3$, four different ν_{eff} values (0.15, 0.21, 0.32, 0.56)

Heat and particle fluxes produced by the fastest growing mode were stored in the database of GS2 results. In the linear simulations, the fluxes themselves do not have a physical meaning, since the perturbed electrostatic potential and distribution function grow exponentially and indefinitely, and the final values only depended on the time at which the simulation were stopped (the GS2 code stops simulations automatically if all input wavenumbers were

converged into well established instability modes, or after completing a pre-defined number of timesteps, 2000 in our case).

But the ratio of particle and heat fluxes is determined by the instability structure (phase shifts between \tilde{n} and $\tilde{\phi}$) and for a formed mode remains constant and independent of the final potential and density perturbation amplitudes. The ratio of particle to ion heat flux, normalized by ion temperature, was considered as the result for each of the GS2 runs.

We are interested in prediction of a stationary density gradient as a function of other parameters mentioned above: T_i/T_e , collisionality, R/L_{Ti} and the particle flux. Unfortunately, the GS2 code can only produce the fluxes as a function of other parameters, which define the instability properties. Therefore we had to calculate Γ' for all possible parameter combinations, and then produce an inverse dependence.

After completing all of the 1040 GS2 runs, the result $\Gamma' = \frac{S}{Q_i} \cdot T_i$ of each of the calculation was stored in a database, thus providing a lookup table for the function $\Gamma' = f(R/L_n, T_i/T_e, v_{eff}, R/L_{Ti})$.

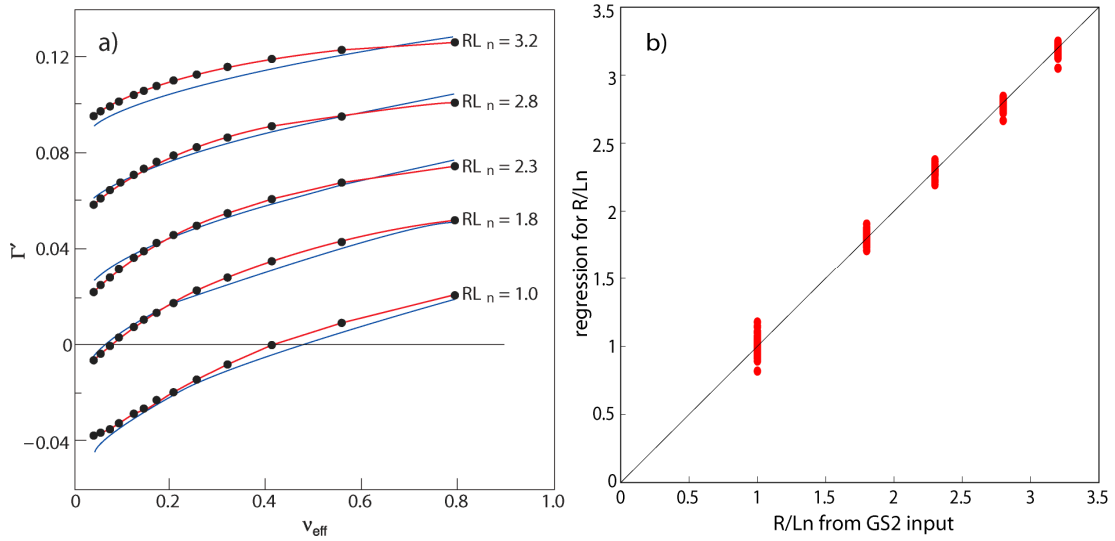


Figure 4.4.2: a) simulation results (Γ' parameter) for fixed $R/L_{Ti}=6.0$ and $T_i/T_e=1.0$. The thin blue line represents the approximation fit by the equation (4.4.1)
b) regressed values (expression 4.4.2) of R/L_n versus those used in GS2 input

To facilitate our analysis, we first removed R/L_{Ti} parameter from the consideration by splitting the database of the GS2 results into 4 groups for each of the input ion temperature gradient values used. In each of those groups now, the particle flux is represented as a table

function of the 3 other parameters: R/L_n , T_i/T_e , v_{eff} . As an example, the $\Gamma'=f(R/L_n, v_{eff})|_{T_i/T_e=1.0}$ dependence can be seen on figure 4.4.2a.

It was found that the Γ' value scales with T_i/T_e , $(v_{eff})^{1/2}$ and $(R/L_n)^{3/2}$. The collisionality dependence varies slightly with R/L_n , as can be seen on figure 4.4.2a (the red lines connecting the fit results are steeper for lower gradient values). We find that introducing the non-linear term $(v_{eff})^{1/2}(R/L_n)^{3/2}$ along with the previous allows us to obtain a satisfactory multiparameter regression for Γ' :

$$\Gamma' = -0.146 + (0.0305 - 0.0081v_{eff}^{1/2})(R/L_n)^{3/2} + 0.1v_{eff}^{1/2} + 0.0524T_i/T_e \quad (4.4.1)$$

This equation for Γ' can be used as an approximation for the table function $\Gamma'=f(R/L_n, T_i/T_e, v_{eff})$ of the real GS2 output flux values for $R/L_{Ti}=6.0$ case. The blue lines on figure 4.4.1a correspond to Γ' obtained from this simple fit.

From the expression (4.4.1) we can extract the inverse function for the density gradient:

$$R/L_n = \left(\frac{0.146 + \Gamma' - 0.0524 \frac{T_i}{T_e} - 0.1\sqrt{v_{eff}}}{0.0305 - 0.0081\sqrt{v_{eff}}} \right)^{2/3} \quad (4.4.2)$$

On figure 4.4.2b one can find the comparison of R/L_n obtained from expression (4.4.2) with the values used as input for GS2. The RMS deviation between real and approximated R/L_n values is ~ 0.066 and the maximum deviation found is 0.23 (at $R/L_n \sim 1.0$)

Now, using the expression (4.4.2), we can compare the simulation results with the experimental data, obtained in our empirical analysis and described in chapter 3.

First, we compare the expression (4.4.2) with the empirical scaling for the stationary density gradient (3.3.8). Beforehand we have to take into account, that the parameters on the right hand side at (4.4.2) cannot be varied independently in the experimental conditions. The correlation between Γ' and T_i/T_e described by the expression (3.5.1) must be taken into account. Substituting $\Gamma=f(v_{eff}, T_i/T_e)$ or $T_i/T_e=f(v_{eff}, \Gamma)$ from (3.5.1) into (4.4.2) gives us

$$R/L_n \sim \left(\frac{0.119 + 0.0656 \frac{T_i}{T_e} - 0.145\sqrt{v_{eff}}}{0.0305 - 0.0081\sqrt{v_{eff}}} \right)^{2/3} \sim \left(\frac{0.1282 + 0.6028\Gamma' - 0.1157\sqrt{v_{eff}}}{0.0305 - 0.0081\sqrt{v_{eff}}} \right)^{2/3} \quad (4.4.3)$$

We use the following approximations to transform (4.4.3) into a linear form:

$$0.0305 - 0.0081\sqrt{v_{eff}} \approx 0.0263, \quad R/L_n^{3/2} \approx 2.106R/L_n - 1.286 \quad (4.4.4)$$

which is satisfactory for the following parameter range: $v_{eff}=0.1-0.5$ and $R/L_n=1.0-3.0$.

Expression (4.4.3) transforms into:

$$R/L_n = 2.76 - 2.62 v_{\text{eff}}^{1/2} + 1.18 T_i/T_e, \text{ and} \quad (4.4.5)$$

$$R/L_n = 2.92 - 2.09 v_{\text{eff}}^{1/2} + 10.83 \Gamma'$$

Comparing (4.4.5) with the empirical scaling (3.4.8) one can see that the parameter dependence predicted by GS2 linear simulations is in good agreement with the experimental observation.

As an alternative simulations-experiments comparison, we calculate the normalized density gradient values obtained from expression (4.4.2) using experimental Γ' , v_{eff} and T_i/T_e values and plot the result on top of the experimentally measured R/L_n (figure 4.4.2). This is the visualization of the agreement between (4.4.5) and (3.4.8).

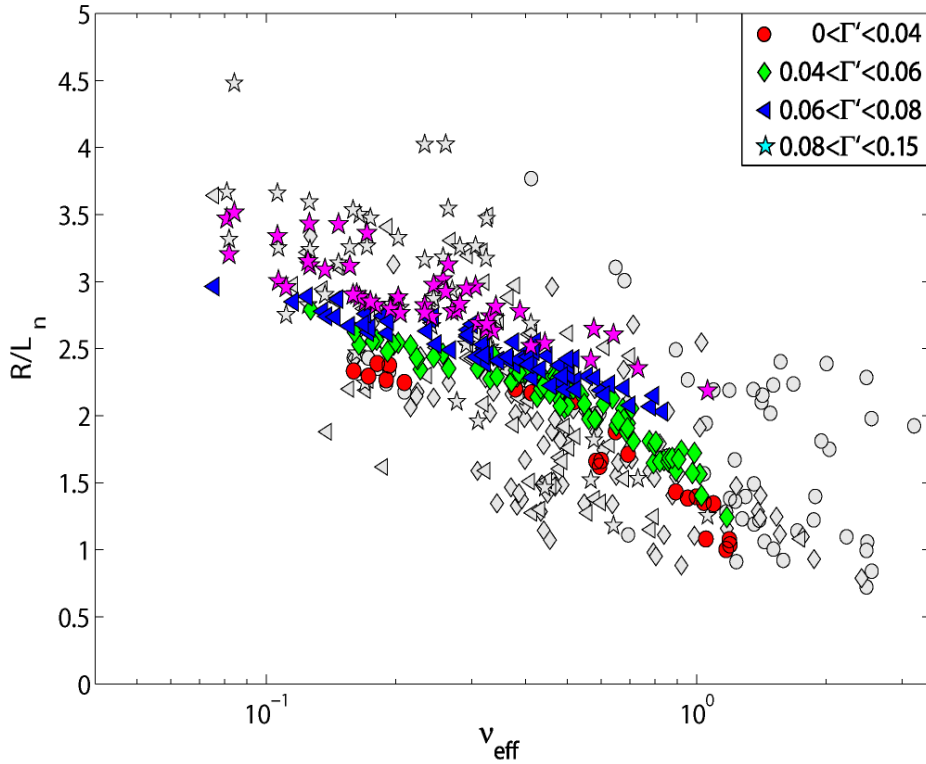


Figure 4.4.3: Comparison of simulation (coloured points) with experimental results (grey points). Different symbols correspond to different Γ' .

So far we considered only the simulations with $R/L_{Ti}=6.0$. On figure 4.4.4 an example of the GS2 output flux for the cases with different ion temperature gradient values is shown. As one can see, the consequences of increasing of the R/L_{Ti} value is quite complex. In general, for higher ion temperature gradient values, the dependence of Γ' on v_{eff} weakens. The dependence of Γ' on R/L_{Ti} is not unambiguous. At low Γ' values it increases with R/L_{Ti} and at intermediate Γ' it changes the sign. In other words, plasmas with high core particle source

increase their density gradient with increasing R/L_{Ti} , while plasmas with low or no core particle sources have the opposite behaviour.

To estimate the effect of different R/L_{Ti} values on the predicted density gradients in experimental conditions, we construct the functions $R/L_n=f(\Gamma', T_i/T_e, v_{eff})$ by analogy with (4.4.2) for the rest of the R/L_{Ti} input values (7.0, 8.0, 9.0).

$R/L_{Ti} = 7.0 :$

$$R/L_n = \left(\frac{0.12 + \Gamma' - 0.0511 \frac{T_i}{T_e} - 0.082 \sqrt{v_{eff}}}{0.0247 - 0.0057 \sqrt{v_{eff}}} \right)^{2/3} \quad \text{RMS}=0.046, \text{MAX}=0.18 \quad (4.4.6)$$

$R/L_{Ti} = 8.0 :$

$$R/L_n = \left(\frac{0.101 + \Gamma' - 0.049 \frac{T_i}{T_e} - 0.0702 \sqrt{v_{eff}}}{0.0208 - 0.0042 \sqrt{v_{eff}}} \right)^{2/3} \quad \text{RMS}=0.045, \text{MAX}=0.21 \quad (4.4.7)$$

$R/L_{Ti} = 9.0 :$

$$R/L_n = \left(\frac{0.087 + \Gamma' - 0.047 \frac{T_i}{T_e} - 0.062 \sqrt{v_{eff}}}{0.018 - 0.0032 \sqrt{v_{eff}}} \right)^{2/3} \quad \text{RMS}=0.05, \text{MAX}=0.23 \quad (4.4.8)$$

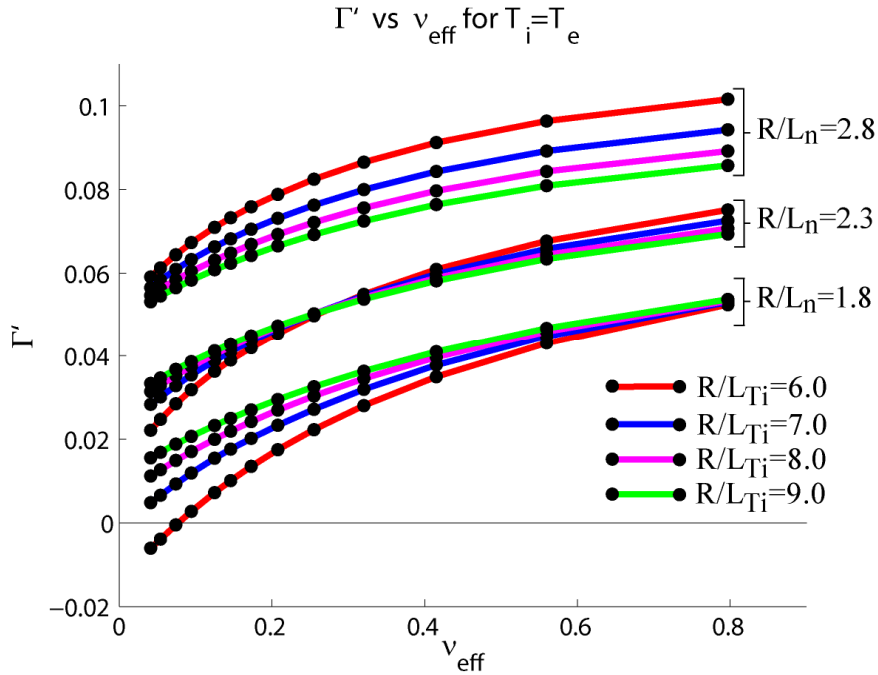


Figure 4.4.4: Simulations results for different R/L_{Ti} values. $T_i/T_e=1.0$ for all the cases shown.

As it was already shown in chapter 3, in JET H-mode experiments the density peaking doesn't depend significantly on R/L_{Ti} . To check whether this is consistent with the simulations, we calculate R/L_n for all 4 R/L_{Ti} values substituting the experimental values of T_i/T_e , Γ' and v_{eff} into the expressions (4.4.2) and (4.4.6-8). On figure 4.4.5 the corresponding values of R/L_n for the $R/L_{Ti} = 7.0, 8.0$ and 9.0 are plotted versus our base case with $R/L_{Ti}=6.0$.

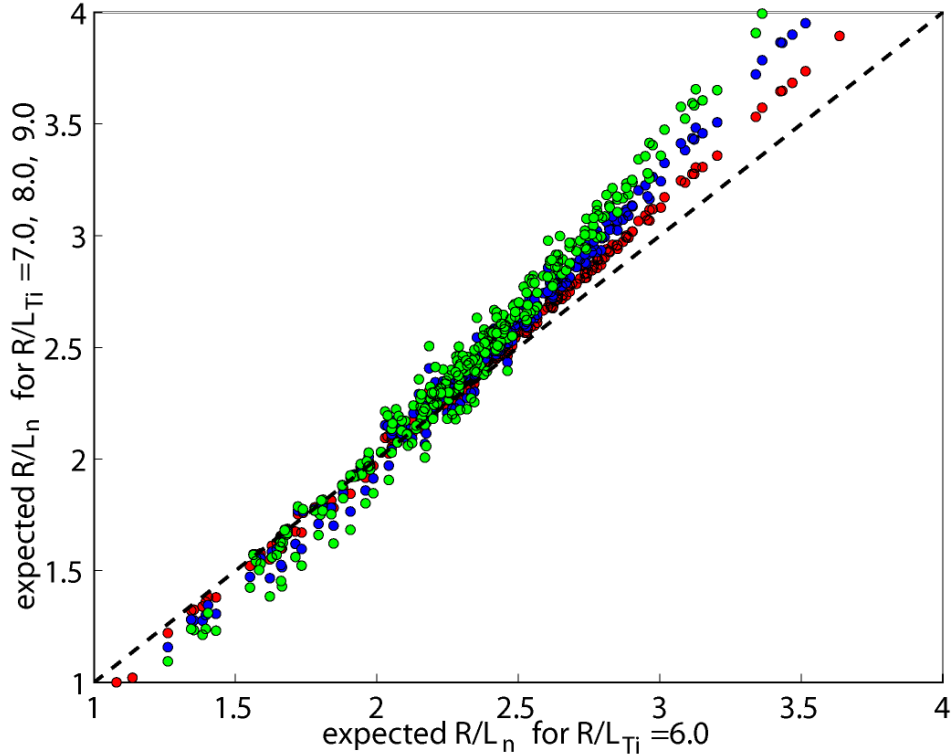


Figure 4.4.5: Expected R/L_n values in JET database for $R/L_{Ti}=7.0, 8.0, 9.0$ with respect to the initial $R/L_{Ti}=6.0$ case.

The difference between all four cases is noticeable at higher density gradients where R/L_n increases with R/L_{Ti} . At intermediate density gradient the R/L_n points for all R/L_{Ti} cases are mixed up (i.e. there is no clear dependence) and at the lowest R/L_n a weak inverse tendency is observed. Cross-correlation coefficient between the R/L_n and corresponding R/L_{Ti} values $6.0 \div 9.0$, calculated by (3.4.2), gives a factor of **0.18** for the cases with $v_{eff} < 0.5$ – low collisionality domain which were used for the empirical analysis. This is small enough to conclude that according to our GS2 simulation results, there is no expected dependence of density peaking on the ion temperature gradient for the JET experimental parameters, which is consistent with the observations.

4.5 Local shear dependence in simulations and comparison with the experiment.

In the empirical scaling (3.4.7-8) we used the internal inductance as a characteristic of the safety factor profile. This is an easily obtainable integral characteristic of the current profile width which can be derived from magnetic measurements. But in the simulations the local values at $r/a=0.5$ can only be used.

Measuring the q profile shape in tokamak plasmas, and especially its local gradient values (which in fact the magnetic shear is) is very challenging. There are diagnostics on JET dedicated to the q profile measurements (polarymetry[68] and MSE diagnostic[69]), but they are not operated routinely and cannot provide a reliable local shear measurement anyway.

In this work, to get the magnetic shear value at $r/a=0.5$, we will use an extrapolation based on EFIT [30] reconstruction for the current profile shape. This is a very basic estimation, but only this one is available on a routine basis.

On figure 4.5.1 we plot the local shear value at $r/a=0.5$ from the EFIT equilibrium code versus the internal inductance for the JET plasma shots stored in the experimental database. As one can see a relationship between those two parameters can be established:

$$\hat{s}(0.5) \approx -0.35 + 0.92 I_i. \quad (4.5.1)$$

To investigate the effect of the local shear, a separate, smaller set of GS2 runs was produced,. Three parameters were varied: R/L_n (1.8, 2.3, 2.8, 3.2), v_{eff} (9 values between 0.03 and 0.8) and \hat{s} (0.0, 0.3, 0.6, 0.9). An example of the simulation results one can see on figure 4.5.2. Higher shear always leads to lower particle fluxes needed to maintain a given density gradient, so higher mid-radius shear and as a consequence higher I_i should lead to stronger peaking.

We obtained the following linear regression fit of R/L_n in the input data of GS2 runs versus collisionality, \hat{s} and the output Γ :

$$R/L_n \approx 1.66 \pm 0.07 - (1.1 \pm 0.1) v_{\text{eff}}^{0.5} + (15.2 \pm 0.6) \Gamma + (0.99 \pm 0.07) \hat{s} \quad (4.5.2)$$

This form of the fit with the RMS of the deviation equal to 0.096 and maximum deviation 0.33 is less accurate than one we used before (4.4.2), but considering the uncertainties in the local shear measurements, it is good enough for our purposes.

From (4.5.2), the GS2 prediction for the local shear effect on the density gradient is:

$$\frac{\partial(R/L_n)}{\partial(\hat{s})} \sim 1.0. \quad (4.5.3)$$

Combining (4.5.3) with the experimentally derived relation (4.5.1) between \hat{s} and l_i we get:

$$\frac{\partial(R/L_n)}{\partial(l_i)} \sim 0.90 \quad (4.5.4)$$

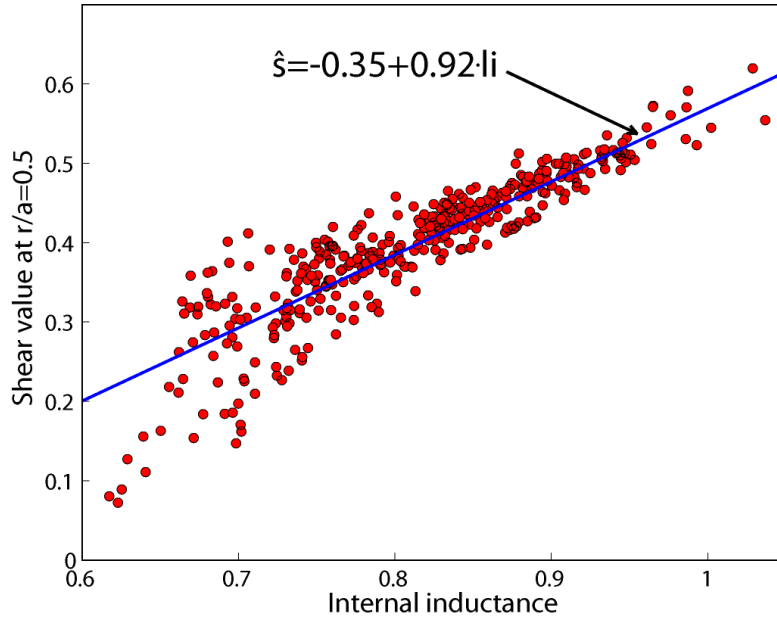


Figure 4.5.1: Relation between the local shear at $r/a=0.5$ and the internal inductance in the JET experimental database.

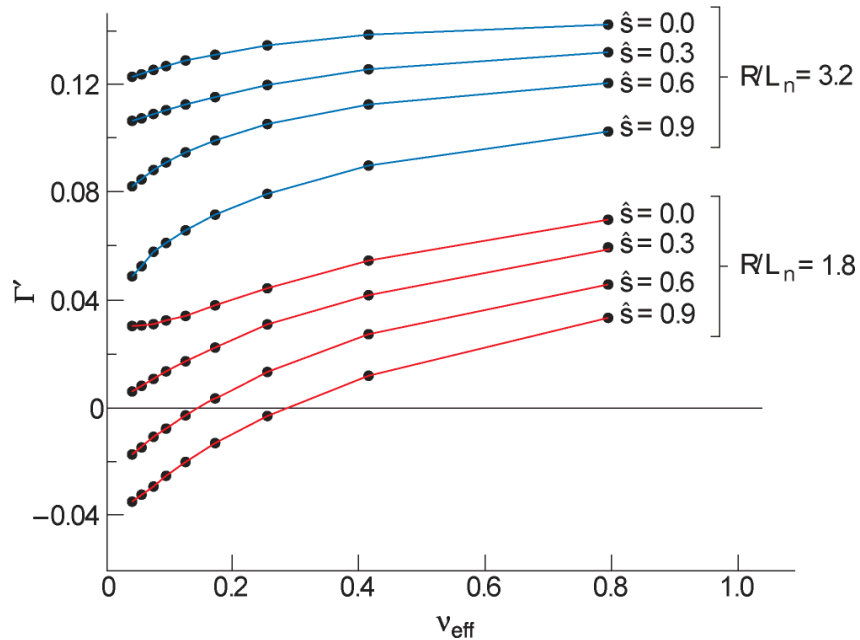


Figure 4.5.2: Γ' from GS2 simulations with different R/L_n and \hat{s} inputs. $T_i/T_e=1$, $R/L_{Ti}=R/L_{Te}=6.0$

In the empirical database (3.3.5) these values are equal to 0.99 ± 0.49 for the $\{\nu_{\text{eff}}^{1/2}; \Gamma'; l_i\}$ fit and 1.28 ± 0.51 for the $\{\nu_{\text{eff}}^{1/2}; T_i/T_e; l_i\}$ fit. We conclude that the GS2 linear simulations and JET observations agree within the error bars on the shear dependence.

4.6 Summary

Due to the presence of a strong magnetic field and pressure gradient, drift waves are ubiquitous in magnetically confined plasmas. They can be unstable in most conditions prevailing in tokamaks and are believed to be the main cause of anomalous transport.

Particle transport caused by such instabilities usually has both diffusive and convective components. The convective part of the flux is caused by correlation between perturbed density and electrostatic potential fluctuations. Depending on the phase shift between them, the overall convective flux can be directed either inwards or outwards.

Using the GS2 code in the linear electrostatic mode, we have modelled the particle fluxes produced by ITG turbulence (which appeared to be ubiquitous in the conditions of JET H-mode plasmas). Several parameters were varied in the code input and the expression (4.4.2) describing a steady-state density gradient was derived.

Good agreement between experiments and simulations was found, over the wide range of each of the parameters involved. Those include: effective collisionality ν_{eff} , electron to ion temperature ratio T_i/T_e , core particle source term Γ' . The ion temperature gradient was predicted to be unimportant for the density peaking in the conditions prevailing in JET, which is also in agreement with observations. The effect of the local magnetic shear value in simulations shows the same tendency as in the experiments, within the error bars.

Using the expression (4.4.2) we can provide an extrapolation of the simulation results to the ITER plasma conditions, taking $\Gamma'=0$ and $T_i/T_e=1.0$ as it was done for the empirical data in section 3.4. Expression (4.4.2) then becomes:

$$R/L_n = \left(\frac{0.0936 - 0.1005\sqrt{\nu_{\text{eff}}}}{0.031 - 0.0081\sqrt{\nu_{\text{eff}}}} \right)^{2/3} \quad (4.6.1)$$

which is shown on the figure 4.6.1.

As one can see, within the range of parameters used in the GS2 input, resulted R/L_n is always positive. At the collisionality values foreseen for the ITER H-mode plasma, the expected density gradient is equal to $R/L_n \sim 1.5$. This is in qualitative agreement with the

empirical observations done in this work and in other publications based on the earlier experiments on JET and on other machines [21-24], which all predict a peaked density profile in such conditions.

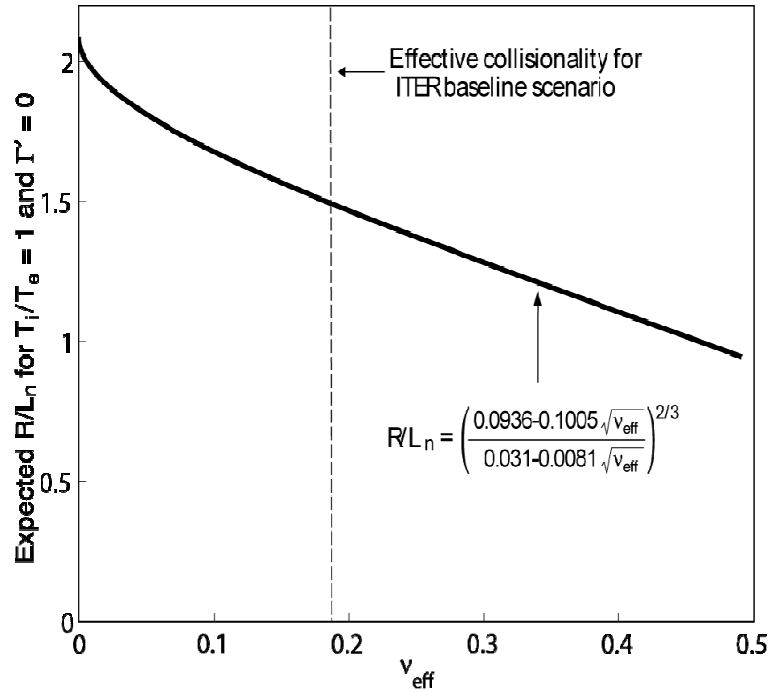


Figure 4.6.1: R/L_n from the GS2 simulations for $T_i/T_e=1.0$ and $\Gamma'=0$ case.

Although, in spite of a good agreement between the empirical (3.4.8) and simulation (4.4.5) scaling laws, there is a quantitative disagreement between the experimental and theoretical predictions ($R/L_n=1.5$ versus 2.0-2.8).

In fact, the empirical scaling (3.4.7-8) was derived on a basis of JET NBI-heated experiments, where the strong relation (3.4.1) between T_i/T_e and Γ' exists. The provisional ITER plasma conditions ($T_i/T_e=1$ and $\Gamma'=0$) do not satisfy the relation (3.5.1), so simple extrapolation of scalings (3.4.7-8) to ITER can be inaccurate, what we actually observe in comparison with the simulations.

The reason of the uncertainty is in the *opposite* effect of T_i/T_e and Γ' parameters on the density peaking in our simulations, on a background of their direct relation described by (3.4.1). This leads to underestimation of their effect on density peaking in empirical analysis and consequently slight overestimation (in comparison with the simulations) of R/L_n for the ITER extrapolated density profile.

Nevertheless, for the generation of modern, relatively big tokamaks, due to the equipartitioning heat flux between electrons and ions, the variation of T_i/T_e parameter is quite limited to produce a huge deviation between different experiments. So the effective collisionality remains the main parameter defining the density peaking in H-mode plasmas, which results in similar observations of density profile behaviour on JET, AUG and C-MOD tokamak with the same principal conclusion about the peakedness of the density profile in ITER plasma conditions.

Although, extrapolation of the common H-mode scaling to smaller tokamaks can be misleading, since the range of possible variations of T_i/T_e ratio increases significantly due to lower electron-ion connection and the observed result may differ from those on bigger machines. That will be discussed in the next chapter, describing H-mode experiments done on the TCV tokamak.

CHAPTER 5

ECRH heated H-mode experiments on the TCV tokamak.

5.1 The TCV tokamak.

The TCV device (Tokamak á Configuration Variable) at CRPP is a medium sized tokamak, with main parameters shown in table 5.1.

Table 5.1: The main parameters of the TCV tokamak

Parameter	Value
Plasma height	Max. 1.44m
Plasma width	Max. 0.48m
Vessel major radius	0.875m
Plasma current	1.2 MA (max)
Plasma elongation	Max. 3
Aspect ratio	3.6
Toroidal magnetic field on the magnetic axis	max. 1.43T
Additional heating (ECRH)	Max. 4.5MW
Transformer flux	3.4Vsec
Loop voltage	Max. 10V
Plasma duration	Max. 5 sec
Vessel width	0.56 m
Vessel height	1.54 m

The TCV tokamak, which came into operation in 1992, was designed specifically for the study of plasma shape effects on stability and confinement. The device has a significantly elongated vacuum vessel, with 90% of the inner surface covered by graphite tiles to withstand a significant power load, and provide flexibility for the positioning of limiter configurations as well as for the divertor strike points when divertor plasmas are produced.

Sixteen independently controlled poloidal magnetic coils with active feedback control allows to achieve an unparalleled range of plasma configurations, including highly elongated shapes, circular plasmas; negative and positive triangularity, rectangular and lozenge shapes shapes, as well as single and double null divertor configurations and doublets [70-72]. Some examples of plasma configurations are shown on figure 5.1.1.

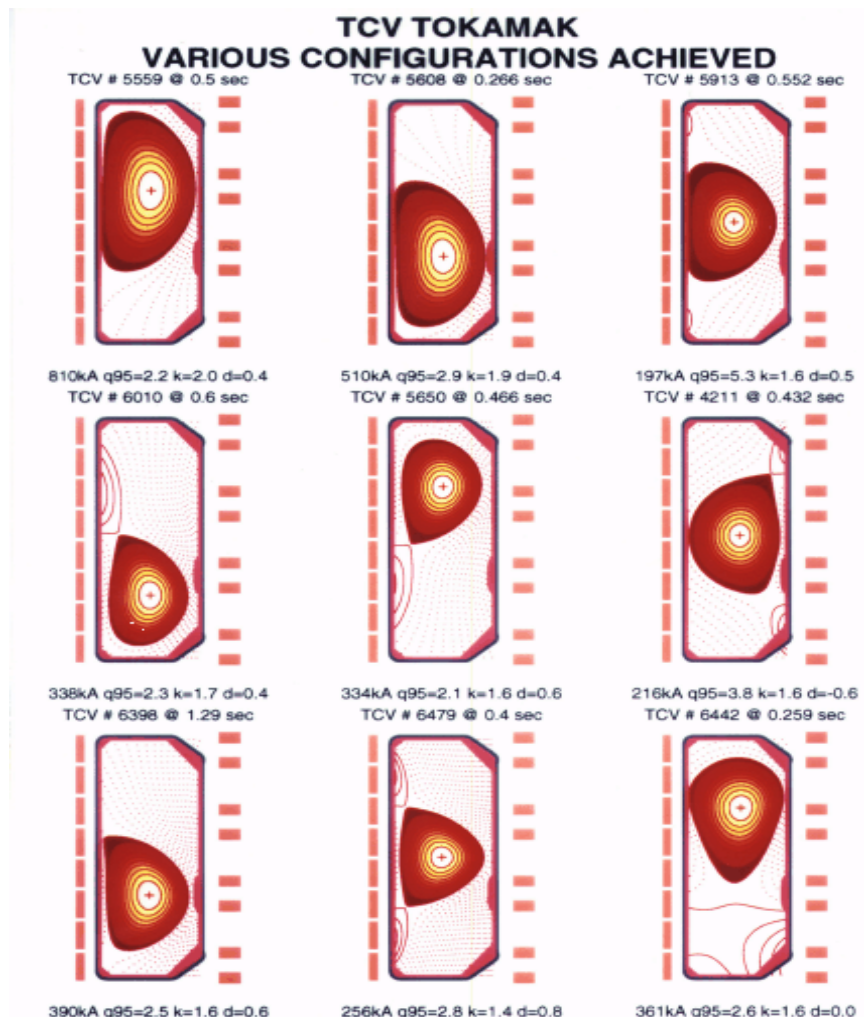


Figure 5.1.1: TCV plasma shapes

Since 1998 the TCV tokamak is equipped with an auxiliary ECRH (Electron Cyclotron Resonance Heating) system [73, 74]. Currently the system consists of six 82.7GHz gyrotrons for heating and current drive at the second harmonic of the electron cyclotron resonance, and three 118GHz gyrotrons for heating at the third harmonic. The EC launcher lines of sight are shown in figure 5.1.2. Second harmonic power is injected from the equatorial and the upper lateral ports. An advanced launcher system with a real time control is used, which provides extreme flexibility in the heating power deposition and ECCD (Electron-Cyclotron Current

Drive). Cut-off and refraction prevent the usage of this system at plasma densities higher than $n_{\max} \sim 4 \cdot 10^{19} \text{ m}^{-3}$, which is below the typical densities of H-mode plasmas in TCV.

The density limit for the third harmonic ECRH heating in X-mode (X3) is $n_{\max} \sim 11.0 \cdot 10^{19} \text{ m}^{-3}$, which is enough to use the system in the H-mode plasmas. Due to relatively low power absorption of electromagnetic waves at the 3rd harmonic, X3 is launched vertically, such as to cross the X3 resonance at a small angle, thereby maximizing the interaction length (see figure 5.1.2). With an optimal launching angle, X3 absorption can reach 85% [75], providing $\sim 1.4 \text{ MW}$ of total heating power when all three gyrotrons are used.

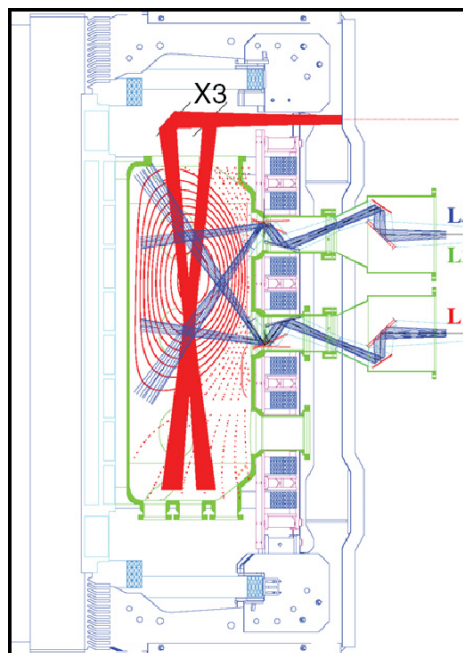


Figure 5.1.2: Poloidal cross-section of the TCV tokamak showing the ECRH launcher positions.

5.2 TCV diagnostics.

TCV is equipped with a comprehensive set of diagnostics covering a large range of plasma parameters. The most important diagnostic systems are magnetic diagnostics, Thomson scattering, a FIR interferometer, X-ray tomography, bolometry (foil and AXUV diodes), Neutral Particle Analyzers, a DNBI (Diagnostic Neutral Beam Injector) for CXRS (Charge eXchange Recombination Spectroscopy) and Electron Cyclotron Emission. Most of the diagnostics are designed to cover the whole elongated vessel cross-section, but some of them are tied to a certain line of sight due to constructional constraints and thus limited to a

specific plasma positioning. The diagnostic systems which are most important for this work are described below.

The Thomson Scattering system layout was already shown in chapter 2 (figure 2.1.2). It is of the “classical” design (not the LIDAR time-of-flight measurement). Three pulsed Q-switch Nd-YAG lasers ($\sim 1.06\mu\text{m}$) placed outside the torus hall, are operated at 20Hz repetition rate and provide approximately 1J of energy per pulse. The trigger timing can be set arbitrary, giving a choice to either increase the repetition rate of the measurements to 60Hz or to effectively triple the energy of a single pulse by simultaneous triggering for measurements at lower plasma density.

The scattered light is collected by 3 high F-number lenses at the equatorial, upper and lower lateral ports to cover the whole elongated cross-section. Then it is transferred by a set of optical fibers to the 25 polychromators, which measure the width of the scattered light spectrum. An absolute calibration is obtained by means of Raman scattering from the nitrogen gas at 0.1bar, let into the vessel.

The FIR interferometer diagnostic uses the heterodyne Mach-Zehnder scheme, as described in the section 2.2. The $213.6\mu\text{m}$ line in CH_2F_2 gas, pumped by a CO_2 laser is used as a source of the infrared radiation. It is divided into 2 beams – one is the reference beam for the heterodyne detection, and the second is expanded by beam-shaping mirrors nearly to a width of the TCV plasma cross-section and launched into the vacuum vessel vertically from the bottom. 14 dielectric waveguides at the top of the vessel define the position of the measurement chords (figure 5.2.1).

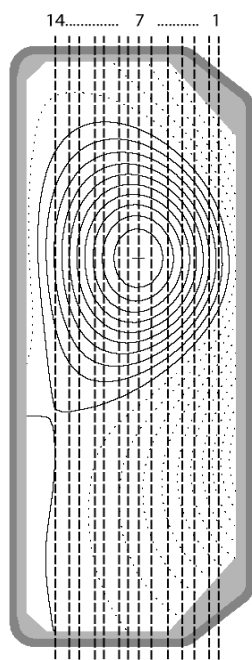


Figure 5.2.1: TCV vessel and 14 FIR chords position.

The FIR channels are covering the whole plasma cross-section, but the chords at the high field side (numbers ~10-14 on the figure 5.2.1) cross the divertor region for the standard plasma H-mode configuration, which is used in the X3 heated experiments described below. The divertor plasma is of low temperature but of relatively high density, and most importantly it is outside of the last closed flux surface. Thus the measured line integrated density from these FIR channels in our case are significantly overestimated, since contain the divertor density. For this reason we restricted usage of the interferometer for density profile reconstruction to the channels 1-9, using the algorithm described in section 2.3. For a single inversion, the line integrated density values were averaged over 100ms time window in order to smooth out the oscillations associated with the ELM relaxations (~20-30ms period) and due to mechanical vibrations. Equilibrium reconstructions were done by the LUIQE [31], code which uses diamagnetic loop measurements, the boundary magnetic probes and flux loops.

There are two different diagnostics capable of measuring the ion temperature in TCV, namely Neutral Particle Analyzers[76], and Charge eXchange Recombination Spectroscopy (CXRS) [77, 78] on the diagnostic neutral beam injector.

The NPA diagnostics measure the energy distribution of the escaping neutrals. Some of these neutrals were born in the plasma core after a recombination or a charge exchange reaction, so they contain information about the ion temperature if the optical thickness of plasma is small enough to let them reach the edge. There are two NPA detectors installed on TCV, one with a vertical line of sight, and with a horizontal line of sight in the equatorial plane. Examples of reconstructed ion temperature profiles have been published [78] for the L-mode plasmas, but unfortunately, measuring the core ion temperature for the H-mode plasmas is not possible due to low neutral penetration rate at such high plasma densities, and periodic ELMs, which induce spurious signals in the measurements.

The charge exchange spectroscopy method is based on measuring the Doppler broadening of the hydrogen-like carbon C^{+5} spectral line on the $n=8 \rightarrow 7$ transition. The C^{+5} ion concentration in plasma core is low, since the temperatures are significantly higher than the ionization potential. A special diagnostic neutral beam injector is used to create C^{+5} ions in plasma by means of the charge exchange reaction: $D^0 + C^{+6} \rightarrow D^{+1} + C^{+5}$. Since the potential well depth for the orbiting electron of the C^{+5} ion is higher than that of D^0 , the electron of the resulted carbon ion appears on high energy level and emits the light on various chain transitions (including the $8 \rightarrow 7$).

TCV is equipped with a diagnostic injector capable of producing a beam of neutral hydrogen of high enough energy (up to 52keV) to penetrate inside the plasma core, but with low enough total power to neglect the influence on plasma conditions. Most importantly, for the most visible charge exchange transition, the maximum cross section is approximately at 50keV.

The diagnostic neutral beam is injected horizontally from the equatorial port and cannot be moved, so its penetration into the plasma core is dependent on the discharge configuration. For the standard H-mode discharges with magnetic axis position at $Z \sim 20\text{cm}$ above the midplane, the ion temperature measurements are available unfortunately only for the outer part of plasma at $r/a > 0.6-0.7$.

5.3 Third harmonic ECRH heated H-mode experiments on TCV.

Transition from low confinement (so called L-mode) to high confinement (H-mode) is observed in tokamaks when a certain heating power threshold value is exceeded. For the moment, there is no universal theory capable of predicting the threshold value and its dependence on plasma parameters. Empirical scalings obtained from different machines gives very approximate results with RMS deviations of up to 30% [80]. The threshold is also known to be strongly dependent on vessel conditions, which are hard to quantify, as well as on the direction of the ion grad-B drift with respect to the x-point and on plasma rotation, as induced by the heating beams.

In large devices, a significant auxiliary heating power is needed for the L-H transition. The estimated threshold power value for the ITER device is $\sim 52\text{MW}$ for deuterium plasma.

TCV can reach the H-mode state only with Ohmic heating. In the ECRH experiments, presented in this chapter, the auxiliary heating power was applied to Ohmic plasmas which had already undergone an L-H transition [75]

At the moment of writing, the database of TCV X3 heated H-mode experiments contains 85 shots. In each of those shots, application of the additional heating causes a switch to a “large” ELMs regime (figure 5.3.1a). The ELM frequency decreases significantly (from $\sim 200\text{Hz}$ to $\sim 40\text{Hz}$) and the energy loss per single disruption increases up to 15% of the total stored energy as measured by the diamagnetic loop. In some cases (for reasons not understood) the plasma transits to a quasi-stationary ELM-free H-mode regime (figure 5.3.1b)

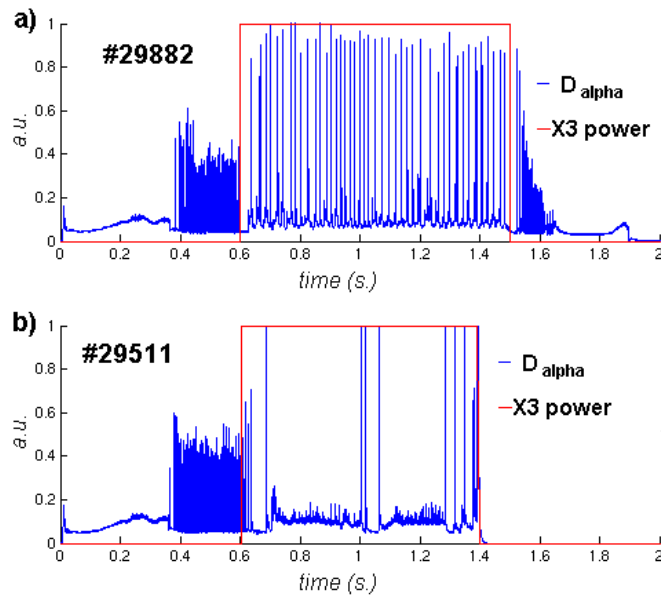


Figure 5.3.1: X3 heated H-mode scenario, a) common giant ELMs case, b) uncommon ELM-free H-mode plasmas

The first X3 heated H-mode plasmas on TCV were achieved in 2005. It has become clear immediately that TCV does not follow the usual scaling for the density peaking, derived from the JET, AUG and C-MOD tokamaks [20-24]. For all of the samples acquired, the density peaking remained on roughly the same level, $n_0/\langle n_e \rangle \sim 1.5$, independently of the X3 heating power, which was varied slightly by changing the launching angle and in some cases by running some of the gyrotrons at a duty cycle. The effective collisionality range for X3 heated plasmas is $\nu_{\text{eff}} \sim 0.5-1.0$. The same peaking factor was observed in the Ohmic H-mode phase as well, which has a much higher effective collisionality ($\nu_{\text{eff}} \sim 3.0$).

Thus, contrary to bigger machines, no evidence for a collisionality dependence was found. Moreover, the peaking was considerably higher than one observed on other tokamaks for the same collisionality values, in spite of the negligibility of the core particle fueling: no NBI heating and edge neutral penetration, as calculated with KN1D code [81,93] in these discharges (figure 5.3.3, courtesy of A. Zabolotsky). The figure shows the flux profile associated with the neutral source from the edge (red curve), obtained from a KN1D simulation, normalized to its value at the edge, since no absolute measure of edge source is available. It also shows the outward flux calculated resulting solely from anomalous diffusion, assuming that D is proportional to the electron heat diffusivity, again normalised to the edge value. The figure shows clearly, that even in TCV, the source and the transport

induced fluxes cannot be matched unless an inward pinch, be it anomalous or neoclassical, is included.

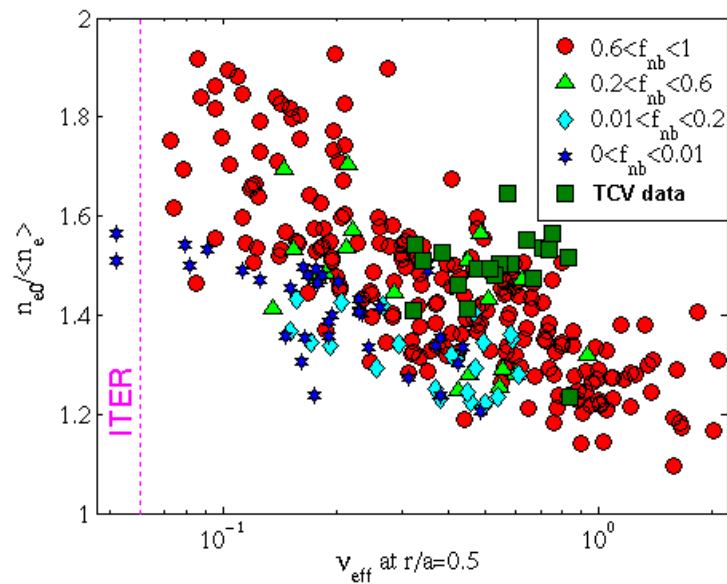


Figure 5.3.2: Density peaking versus effective collisionality at $r/a=0.5$ (not the volume average!), TCV 2005 experiment data points on top of the JET pre-2005 experiments [82].

Green points are the X3 heated plasmas, ohmic cases at $v_{\text{eff}} \sim 3.0$ are not shown.

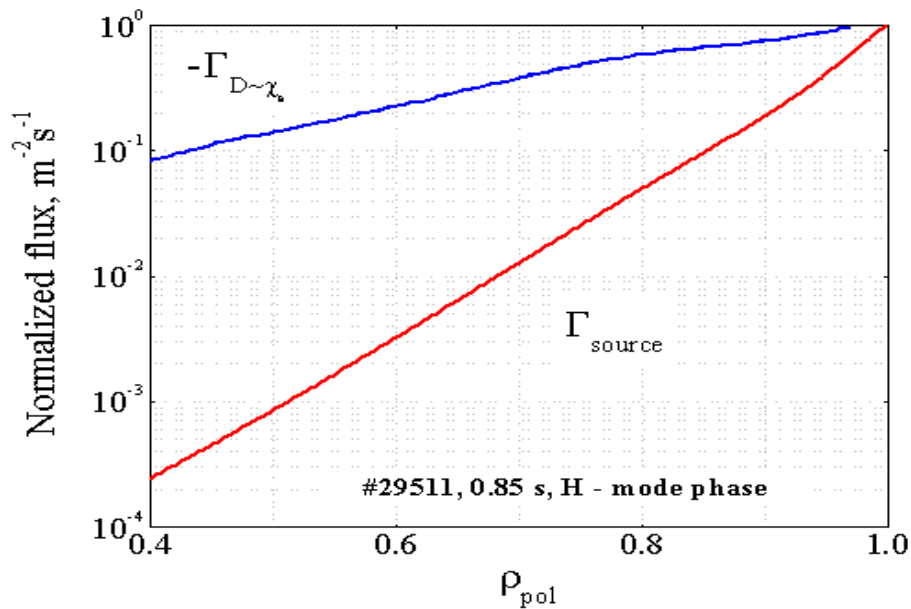


Figure 5.3.3: Kn1D simulation of edge neutral flux and comparison with particle diffusion flux (in assumption $D \sim \chi_e$) for X3 heated H-mode plasma.

Later in 2007 another series of X3 heated H-mode experiments was produced. Only 2 gyrotrons were available at that point. In these experiments however the target plasma density was lower, so the final electron temperature and effective collisionality are in the same range.

On figure 5.3.4 density peaking versus effective collisionality and line integrated density for all TCV X3 heated experiments is shown. By analogy with the density profile inversion for the JET database (see section 3.2), only the samples with less than 3% inconsistency between the measured and reconstructed line integrated densities were considered. This led to 93 remaining samples from 45 different shots. Comparing to the JET databases, which cover a large variety of different H-mode experiments, the TCV experiments' diversity is quite limited. There are basically only two types of experiments represented: high power X3 heating applied to relatively high density plasmas, and reduced power X3 heating in lower density plasma. But even from those experiments we can derive 2 important observations:

- 1) There is no explicit effective collisionality dependence of the density peaking in TCV H-mode experiments. Very high and very low peaking can be observed at the same collisionality values.
- 2) There is some correlation of density peaking with the plasma density. Application of the ECRH heating to less dense plasmas causes a flattening of the density profile, while heating plasma with higher density doesn't. This effect is similar to one observed in the AUG tokamak and described in [83].

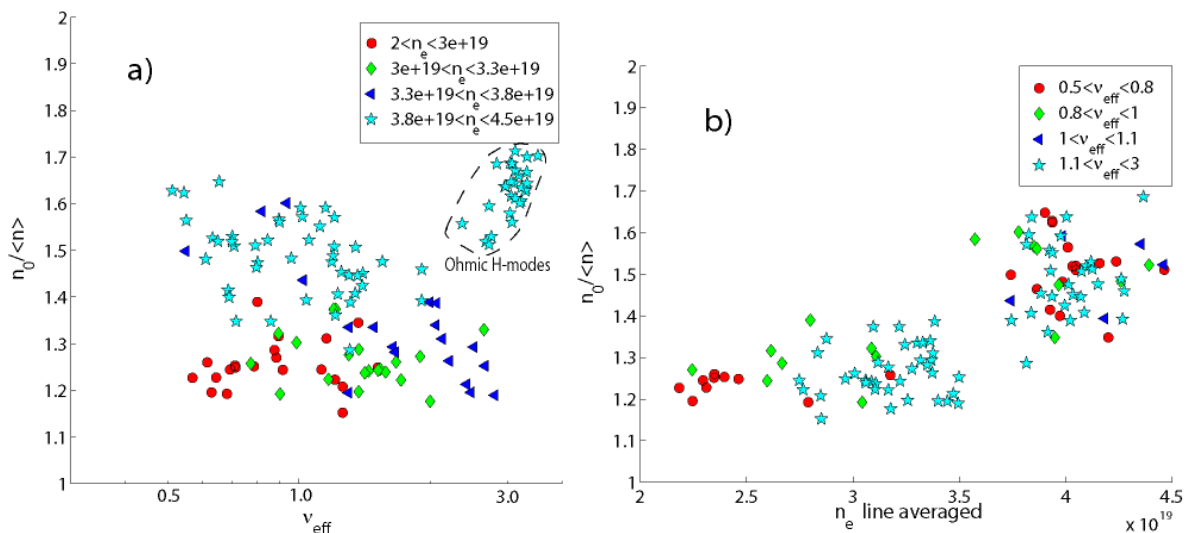


Figure 5.3.4: density peaking in X3 heated H-mode plasmas on TCV, a) versus effective collisionality, grouped by different line integrated density, b) versus line integrated density, grouped by different ν_{eff} .

The TCV density peaking does not agree with the empirical scaling (3.3.7-8), although one should keep in mind that the conditions of TCV H-mode plasmas are different from those on most other machines like JET and AUG, where the common scalings for density peaking were derived [23]. Due to the smaller machine size, the equipartitioning rate τ_E/τ_{ei} (τ_E – energy confinement time, τ_{ei} characteristic energy exchange time between electrons and ions) for TCV is significantly smaller. Without any auxiliary ion heating, the ions are heated only by collisions with the electrons, with the power density:

$$H = \frac{1}{\tau_{ei}} n(T_e - T_i), \text{ where } \tau_{ei} = \frac{3}{2} \frac{m_i}{m_e} (2\pi)^{3/2} \frac{\epsilon_0^2 m_e^{1/2} T_e^{3/2}}{n e^4 \ln \Lambda} \quad (5.3.1)$$

at the same time, the energy loss by the ions can be estimated as:

$$L = \frac{nT_i}{\tau_i}, \quad (5.3.2)$$

where τ_i is the ion energy confinement time. In steady state $L=H$, hence

$$\frac{T_i}{T_e} = \frac{1}{1 + \tau_{ei}/\tau_i} \quad (5.3.3)$$

As we can see, in the case of a large enough machine $\tau_{ei} \ll \tau_i$ and therefore $T_i/T_e \cong 1$, even if the ions are not directly heated. In smaller machines, such as TCV, τ_i can be much smaller than τ_{ei} , resulting in ion temperatures very significantly below the electron temperatures. The ion temperature is very sensitive to plasma parameters, since τ_{ei} itself depends on electron temperature and density as $\sim n^{-1} T_e^{3/2}$.

In the AUG experiments with central ECRH heating, described in [83], the observations were interpreted as follows: the drop of the ion temperature and consequently of R/L_{Ti} for low density plasmas leads to the TEM becoming the dominant instability, which causes a ‘pump-out’ effect (density profile flattening). In contrast, if the auxiliary heating was applied to higher density plasmas, the pump-out was not observed, since the ITG remained the dominant instability.

To check, whether the same explanation is suitable for the TCV X3 heated plasmas, a set of linear GS2 simulations was done, by analogy with the JET case described in section 4.4. As before, the flux surface shape parameters were fixed at some average values:

$$R_{maj}=1.0, R_{geo}=0.947, q=1.2, \hat{s}=0.45, \kappa=1.7, \kappa'=0.1, \delta=0.2, \delta'=0.06, \Delta'=-0.21$$

Simulations were done at $r/a=0.5$, with the electron temperature gradient $R/L_{Te}=6.0$.

The following parameters were varied:

$R/L_{Ti}=3.0, 4.0, 5.0, 6.0$

$T_i/T_e=0.75, 0.5, 0.25$

$v_{eff} = 0.2, 0.28, 0.43, 0.75, 1.65$

$R/L_n = 1.0, 1.5, 2.0$

In total 180 ($4*3*5*3$) simulations were done on the PLEIADES2 parallel computing cluster.

The same linear spectrum as for JET was used, $k_y\rho_s=0.1\dots 1.0$. The ITG mode (positive real frequency) prevails in the TCV simulations as well. The position of the maximum linear growth rate mode shifts towards higher mode numbers with decreasing of the T_i/T_e parameter, from $k_y\rho_s=0.5-0.6$ up to 0.9 (see figure 5.3.5). At the same time the mode frequency decreases with T_i/T_e , so that the fastest growing mode frequency remains roughly the same for all 3 cases.

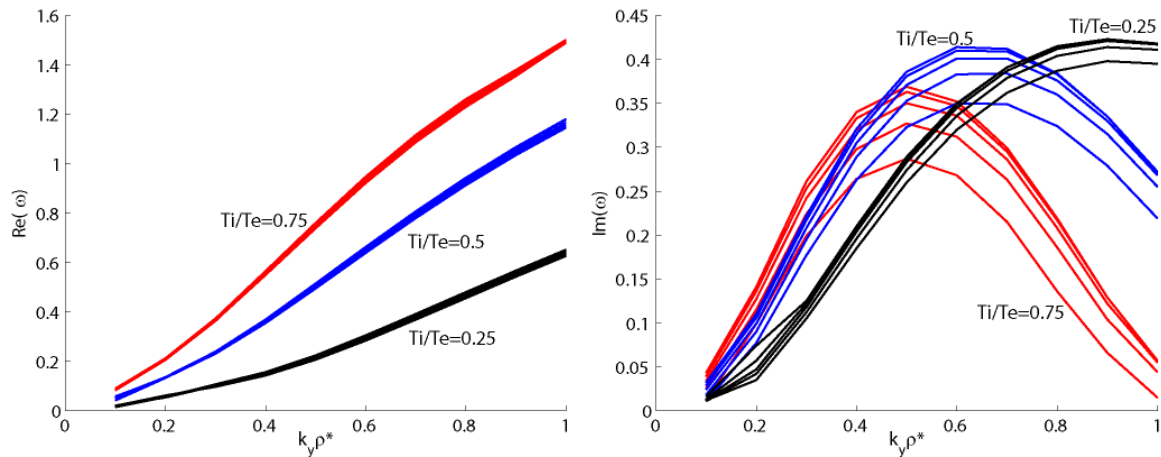


Figure 5.3.5: real and imaginary parts of the mode frequency versus mode number for $T_i/T_e=0.75, 0.5, 0.25$ cases with $R/L_{Ti}=6.0, R/L_n=2.0$,

At the same time, decreasing of the ion temperature gradient leads to decreasing of the linear growth rate, down to the complete mode stabilization at $R/L_{Ti}=3.0$. Contrary to the AUG case [83], no TEM mode was found with these simulation parameters at any of the $k_y\rho_s$ values in the range 0.1-1.0. In case of stabilized ITG, the GS2 simulations just did not converge to any instability. Compared to the AUG simulations described in [83], the TCV simulations had lower R/L_n values, as experimentally observed (1.0-3.0, while $R/L_n \geq 3.0$ for unstable TEM in [83]). These density gradients appear to be too low for destabilizing trapped electron modes.

For the cases with ITG mode activity we calculate the particle flux driven same manner as it was done for the JET case.

Making a linear regression fit for the output Γ' by analogy with (4.4.1) we find:

$$\Gamma' = (-0.124 \pm 0.005) + (0.0138 \pm 0.0014) R/L_n^{3/2} + (0.076 \pm 0.005) T_i/T_e + (0.049 \pm 0.004) v_{\text{eff}}^{1/2} \quad (5.3.4)$$

The 5th non-linear term $v_{\text{eff}}^{1/2} R/L_n^{3/2}$ was found to be ignorable. The coefficient values in (5.3.4) are little different from those found for the JET simulations, but the general tendency is still the same also for the TCV parameter range. Using the approximation $R/L_n^{3/2} \approx 2.106 R/L_n - 1.286$ for $R/L_n = 1.0-3.0$, we find the density gradient for the stationary $\Gamma'=0$ case:

$$R/L_n = 4.9 - 2.62 T_i/T_e - 1.69 v_{\text{eff}}^{1/2} \quad (5.3.5)$$

To compare the simulation prediction (5.3.4) with the experiment, we need ion temperature measurements in TCV H-modes. Unfortunately, only a very few measurements were done in higher density shots (with peaked density profile), and no measurements at all are available for the lower density cases. On figure 5.3.6 an example of T_i measurements in X3 heated plasma is shown. Since the plasma shots were done with the magnetic axis positioned at $Z \sim 20\text{cm}$, the penetration of the DNBI beam ($Z=0\text{cm}$) was very poor, so only the outer part of the plasma was measurable.

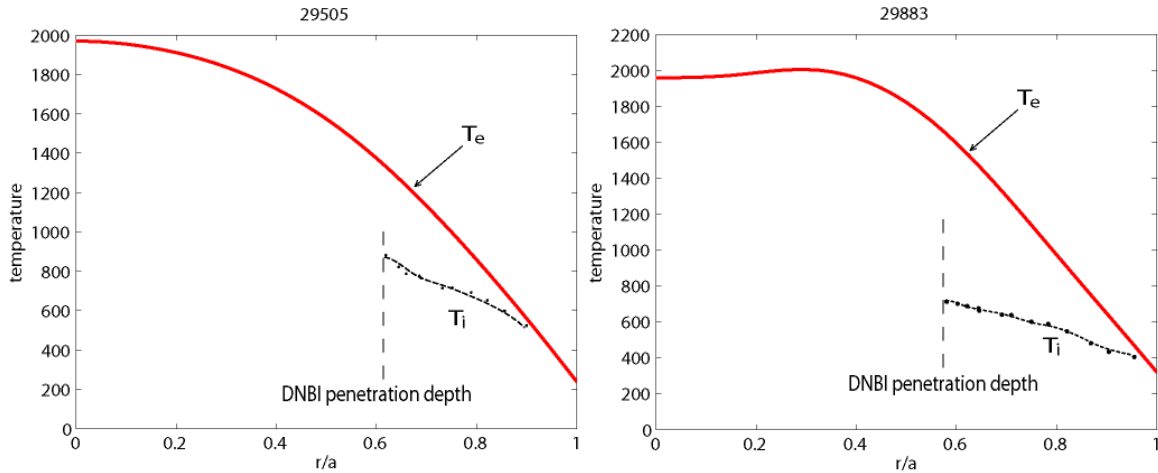


Figure 5.3.6: two examples of T_i measurements in X3 heated H-mode plasma on TCV, shots with higher density and peaked density profile.

From those measurements we can make an estimation of $T_i/T_e \sim 0.5-0.7$ and $R/L_{Ti} \sim 5.0-6.0$. On figure 5.3.7 one can see the curve (5.3.5) for fixed $T_i/T_e = 0.5$ plotted on top of the experimentally measured density gradient.

As one can see, for the low collisionality, GS2 simulations predict peaked density profile for the cases with $R/L_{Ti} \sim 6.0$, $T_i/T_e \sim 0.5$, which is in fair agreement only with part of the experimental data. With increasing of collisionality, the predicted R/L_n drops down to $R/L_n \sim 0.5$ for the Ohmic H-mode cases, while the experimental profile still remains peaked. A significant disagreement exists for the lowest density, low collisionality discharges, for which we still suspect that TEM should be dominant, whereas no TEMs were found within the range of parameters scanned in the GS2 simulations. Future work should explore if these are characterized by even lower T_i/T_e and or larger R/L_{Te} than used in the scan. Finally we note that for TEM modes, it may be necessary to increase the maximum $k_y \rho_s$ in the simulations.

The disagreement for Ohmic H-modes may be of neoclassical origin. So far in this work we didn't consider the neoclassical Ware pinch, since in the low collisionality and hence high conductivity of auxiliary heated H-modes, the toroidal electrical field is modest and the Ware pinch is negligible [22]. This may not be the case for the Ohmic H-modes on TCV.

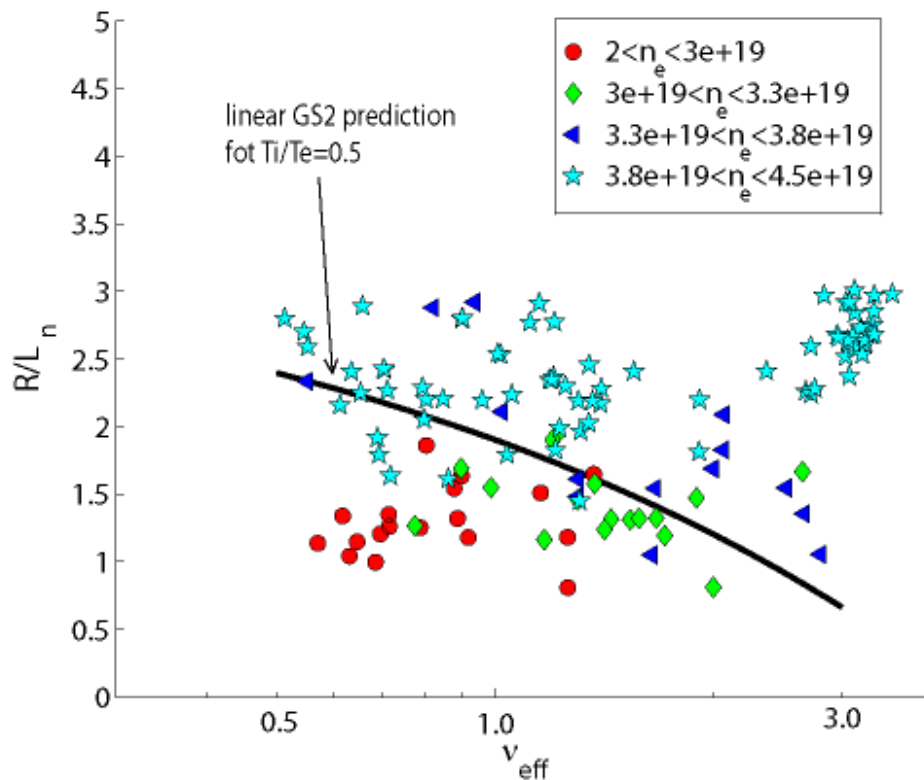


Figure 5.3.7: R/L_n versus effective collisionality for TCV H-modes. GS2 simulation prediction (5.3.5) for $T_i/T_e=0.5$ are drawn on top.

The Ware pinch velocity can be estimated as:

$$\langle v_{ware} \rangle = -\frac{E_{tor}}{B_{pol}} f_{neo} \quad (5.3.6)$$

where f_{neo} is the coefficient which takes into account a number of particles which are participating in the inward drift. In a collisionless circular tokamak plasma case it is approximately equal to the fraction of trapped particles $f_{neo} \sim \epsilon^{1/2} = (r/R)^{1/2}$. In a general collisional case it was calculated in [95] (coefficient L_{31} in the transport matrix [94]). For the TCV aspect ratio, the effect of plasma shape on a trapped particles fraction can be neglected ([94] figure 2). So, taking $f_t \approx \epsilon^{1/2}$, $Z=2$, $n_e=0.85 \cdot 10^{20}$, and $T_e(r/a=0.5)=850\text{eV}$ for the Ohmic H-mode case, $T_e(r/a=0.5)=2150\text{eV}$ for the X3 heated case, and substituting into analytical fits for L_{31} derived in [95], we get $f_{neo}(\text{Ohmic}) \approx 0.26$ and $f_{neo}(\text{Heated}) \approx 0.36$.

B_{pol} can be estimated as

$$B_{pol} = \frac{r}{R} \frac{B_{tor}}{q} \quad (5.3.7)$$

where B_{tor} is the toroidal magnetic field.

$$\langle v_{ware} \rangle = -\frac{RqE_{tor}}{rB_{tor}} \cdot f_{neo} \quad (5.3.8)$$

For the Ohmic H-mode cases, the loop voltage is $V_{loop} \sim 1.2\text{V}$, $q \sim 1.4$ (approx. at the mid-radius), $B_{tor} = 1.45\text{T}$. That gives us the neoclassical pinch estimate for the Ohmic H-mode case: $V_{ware} \sim 0.42\text{m/s}$

According to the power balance calculations [84], thermal electron conductivity in Ohmic H-mode shots is in the range $\chi_e \sim 0.5-0.7\text{m}^2\text{s}^{-1}$, well below typical auxiliary heated conditions. Assuming $D \sim 2\chi_e/3$, as suggested by theory [96], we conclude that the Ware pinch may account for a significant part of the observed density gradient.

With the additional X3 heating, the loop voltage (and consequently the toroidal electrical field) drops down to $V_{loop} \sim 0.6\text{Vm}^{-1}$ and the effect of neoclassical pinch drops by factor of $2 \cdot (0.26/0.36) = 1.44$, taking into account the change in f_{neo} . The additional heating power raises χ_e by a factor of 2-3 [84], leading to an overall reduction of the Ware pinch contribution to R/L_n by a factor 3.0-4.5. In that case the neoclassical Ware pinch is substituted for by the ITG driven one, according to the GS2 simulations results (see figure 5.3.7), so that the density peaking factor remains nearly unchanged.

We can say that linear GS2 predictions cannot be contradicted by the Ohmic H-mode results on TCV, since the Ware pinch may play a significant role.

The cases with flat profiles a low collisionality and low density cannot at present be assessed for lack of ion temperatures. The low density and high electron temperature and consequently low ion heating may have lead to T_i/T_e and/or R/L_{Ti} being at the lower end or even lower than in our parameter scan, stabilizing the ITG mode. However experimentally transport is still anomalous in these discharges, hence it is likely to be due to TEM or ETG modes. ETG modes are characterized by much shorter wavelengths and are thus not covered by our simulations. TEM would be expected to produce the same flattening effect as described in [83]. More work and comprehensive measurements dedicated to particle transport will have to be done on TCV in the future, in order to validate, or invalidate, the GS2 gyrokinetic predictions in the case of strongly electron heated H-modes in TCV.

CHAPTER 6

Overall summary and discussions.

This thesis presents a study of the particle transport in tokamak H-mode plasmas, specifically on the formation of steady-state peaked density profiles. The main part of the thesis content is dedicated to the JET tokamak. Implementation of an innovative density profile inversion technique for the FIR measurements, together with the improvements of the LIDAR diagnostic data processing methods has allowed us to achieve a satisfactory agreement between the two mainstream diagnostics for density measurements.

A database containing a wide variety of H-mode experiments done on JET tokamak during 2006 and 2007 was created and carefully analyzed. With some minor differences, the general conclusions of the previous research done on this topic were confirmed. Namely, the very clear correlation between the density peaking factor $n_0/\langle n_e \rangle$ and the effective collisionality defined as $\nu_{\text{eff}} = 10^{-14} R_{\text{maj}} Z_{\text{eff}} \langle n_e \rangle / \langle T_e \rangle^2$ was reproduced. The particle source term Γ' , the ion and electron temperature ratio T_i/T_e and the internal inductance l_i have been shown to exert a moderate influence on the peaking. No significant effect was found for the other parameters investigated: ρ^* , q_{95} , β_N , R/L_{Te} , R/L_{Ti} .

Extrapolation of the scaling laws, created on the basis of the empirical study, to the ITER plasma condition strongly suggest that the ITER baseline H-mode plasma will have a peaked density profile ($n_0/\langle n_e \rangle = 1.42-1.55$, $R/L_n = 2.0-2.8$), which is also in agreement with previous studies.

It is known ITG microturbulence, which is the prevailing mode in H-mode plasmas, can produce a convective inward particle flux (also called a particle pinch). To evaluate the role of the ITG turbulence in density profile behaviour, observed in JET experiments, the GS2 gyrokinetic code was used. A large amount of linear electrostatic simulations were completed to investigate the response of the resulting particle fluxes to different parameters. The particle to ion heat flux ratio of the most unstable linear modes was used as the simulation output, since it is independent of the final perturbed amplitude in linear simulations. Deliberately, the definition of this value coincides with the definition of the particle source term Γ' used in the empirical analysis to facilitate the comparison of the theoretical predictions with the experiment.

An excellent agreement between the JET experiments and simulations was found. That includes the same dependence, within error bars, on v_{eff} , T_i/T_e , and Γ' over the wide range available in the JET dataset. The dependence on the local shear also has the same character as in the experiment, within the (quite wide) error bars. The normalized ion temperature gradient R/L_{Ti} , for the specific JET experimental parameters range, was found to correlate with the density gradient neither in the experiment, nor in the simulations.

Extrapolation of the GS2 simulation results to the standard ITER H-mode plasma parameters gives a moderately peaked density profile with $R/L_n \sim 1.5$, which is lower than the value obtained from the empirical results only, in spite of a good agreement between the simulation and experimental scaling laws. This is a result of a strong correlation between Γ' and T_i/T_e parameters, caused by the properties of the neutral beam heating. Their effect on density peaking in the experimental data was mutually weakened, so simple extrapolation $\Gamma' \rightarrow 0$ and $T_i/T_e \rightarrow 1.0$ did lead to an overestimated R/L_n prediction. Ideally, the experimental database should be complemented with H-modes with low or no neutral beam fuelling, as expected to be produced at JET in the future, using new ICRH antennae and possibly ECRH. A brief overview of the TCV H-mode experiments with the EC heating was also given in this thesis. The initial results from the X3 experiments on TCV were puzzling, since they were in disagreement with the observation done on other larger machines, i.e. the density peaking factor at the same collisionality values was noticeably higher even without core particle sources.

But the GS2 simulations done by the same manner as for the JET case have shown that the density gradient behavior in TCV H-mode cases with higher density (where no pump-out was observed) is at least not in a contradiction with the ITG instability model, which has shown an agreement with JET experimental results. The absence of collisionality dependence can be explained by the balance of anomalous (ITG induced) and Ware pinch effects.

A proper analysis of the pump-out (density flattening) cases requires ion temperature measurements, which we currently do not possess. The simulations done in this work are suggesting that the ECRH heating of lower density plasma causes decline of ion temperature gradient value and stabilization of the ITG mode, probably leaving the ETG (Electron Temperature Gradient) mode to be the only instability which provides the anomalous electron heat transport, since TEM was stable in our simulations at $k_y \rho_s = 0.1-1.0$ range. The lack of experimental data for this research prevents us from going into a deeper investigation of the matter, leaving this topic for the next generations of PhD students.

In spite of the good agreement between experiments and simulations for the JET plasmas, the quasilinear method used in this work (namely considering the fluxes for a single linear mode with the highest growth rate) is still debated. For a proper analysis of the anomalous pinch behaviour in ITG turbulence, one has to perform non-linear simulations for different plasma parameters, which is too expensive in terms of computational power. So, the only current option available for this kind of research is to use the linear simulations and find a proper way to match the results of the linear runs with what would the non-linear runs produce.

One of the common quasilinear approaches is to run the linear simulations for the mode with the highest mixing length characteristic, $\gamma/\langle k_{\perp} \rangle^2$. This was inspired by observations of the non-linear simulation results of collisionless ITG/TEM turbulence, described in [85], which has shown that the particle and heat transport is peaked around the corresponding $k_y \rho_s^* \sim 0.1-0.2$ values. This is sufficiently lower than the wavenumber of a maximum growth rate mode, which is typically in the $k_y \rho_s = 0.3-0.5$ range (up to 0.9 in our TCV simulations with extremely low T_i). The density peaking analysis based on the low $k_y \rho_s$ number was investigated in [86] and it is in disagreement with the results shown in this work.

To distinguish which of the quasilinear methods is closer to non-linear simulation results, a non-linear run using the GYRO code was done for the plasma conditions close to the standard ITER H-mode case (courtesy of C. Angioni, see figure 6.1). It was shown that for $R/L_n=2$, $T_i/T_e=1$ and the collisionality value corresponding to $\nu_{\text{eff}} \sim 0.2$, the total particle flux produced is close to zero, meaning that the input density gradient parameter will remain stationary. This is in agreement with the linear study based on $\max(\gamma)$ approach, which is supporting the method used in this work. Although, looking at the particle flux spectrum shown in figure 6.1 bottom right, one can understand why this quasilinear approach is still controversial. The non-linear particle flux is not localized around any single mode number. It is distributed over a wide spectrum, where different wavelengths contribute differently: shorter wavelengths produce an inward flux, and longer ones an outward. The total particle flux direction is determined by a balance of lower and higher wavenumber modes, in this case it is close to zero and happens to correspond rather well to the flux produced by the one mode with the highest linear growth rate. Whether this is a single coincidental case or a systematic agreement remains to be investigated in future work. For the moment, apparently, consideration of a single linear mode with the highest growth rate remains the most

reasonable method for systematic studies of particle transport, when large numbers of cases need to be investigated.

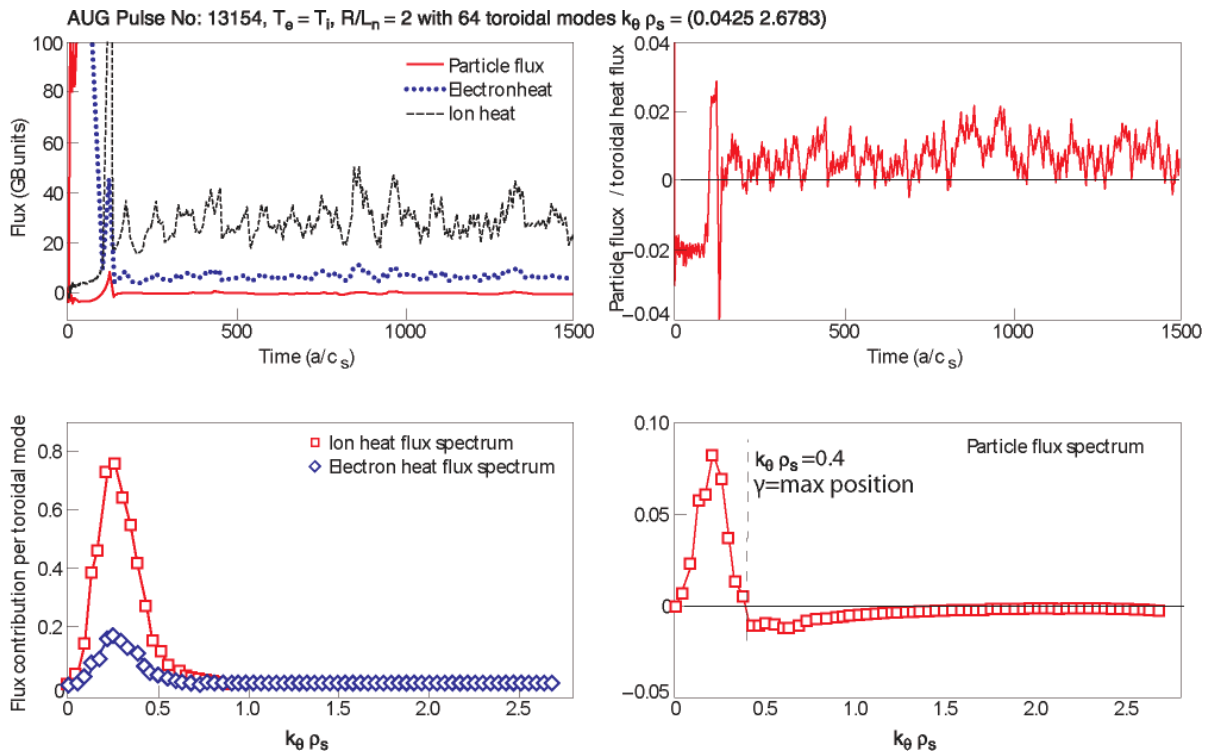


Figure 6.1: Non-linear GYRO simulation results

top-left: heat and particle fluxes vs time.

top-right: particle over heat flux vs time

bottom-left: k_y spectrum for the heat flux

bottom-right: k_y spectrum for the part. flux

As the experimental observations are now backed up with the simulation results, we can state quite confidently that the ITER plasma in the baseline H-mode scenario will have a peaked density profile, rather than a flat one as it was envisaged in earlier studies of the ITER expected performance [51]. The possible consequences of that change can be advantageous and deteriorating.

Plasma density in tokamaks is limited by radiation collapse which is initiating at the edge. The exact value of the limiting density depends on plasma conditions and impurities contamination and is usually normalized to the Greenwald density limit[87], $n_G = I_p / \pi a^2$. ITER is expected to operate at $n = 0.9 n_G$ density. Peaked density profile in plasma allows to reach higher densities in the burning plasma core without overcoming the limiting value. Thus generated fusion power and the reactor efficiency Q are expected to increase in comparison with the baseline scenario [88].

Inductive current in tokamak cannot be driven continuously, so for the steady state operation one must rely on other methods of current generation. The bootstrap current [89] effect was a big fortune for the tokamak concept, since this is the current which is intrinsic in toroidal plasmas and thus provided for free. Up to 50% of the total current in fusion reactors [90] are expected to be contributed by the bootstrap current. Since $J_{BP} \sim dn/d\Psi_p$, this number will be increased in case of a peaked density profile, thus reducing the amount of current to be driven by external means.

One of the concerns associated with density peaking is the possible proneness to impurity accumulations, namely the helium ash (product of D-T burning), possibly carbon as a divertor material and high Z impurities from the first wall. While the carbon profiles are observed to be flat in all conditions [21], behavior of high- Z impurities is still controversial, opposing the accumulation of tungsten and nickel was witnessed in [91,92] and methods of preventing it by central heating were suggested. Intensive research in this field is undergoing.

Bibliography

- [1] L.A. Artcimovich, "Tokamak devices" 1972 *Nucl. Fusion* **12**, 215
- [2] H.P. Furth, "Tokamak research" 1975 *Nucl. Fusion* **15**, 487
- [3] J. Wesson, "Tokamaks" 2004 *Clarendon Press Oxford*, 3rd edition.
- [4] M. Fujiwara et al. 1994 *Proc. 6th Int. Toki Conf. on Plasma Physics and Controlled Nuclear Fusion (Toki, 1994)*, 58
- [5] G. Grieger et al. *Proc. 13th Int. Conf. on Plasma Physics and Controlled Fusion Research (Washington, DC 1990)* **3**, 525
- [6] R.F. Post, "The magnetic mirror approach to fusion" 1987 *Nucl. Fusion* **27**, 1579
- [7] H.A.B. Bodin, W.E. Newton, "Reversed field pinch: Status and trends", 1987 *Plasma Phys. Controlled Fusion* **29**, 1297.
- [8] J.D. Lawson, "Some criteria for a power producing thermonuclear reactor", 1957 *Proc. of the Physical Society* B70, 6
- [9] R. Aymar, P. Barabaschi, Y. Shimomura, "The ITER design", 2002 *Plasma Phys. Control. Fusion* **44** 519-565
- [10] L.M. Kovrizhnykh, "Neoclassical theory of transport processes in toroidal magnetic confinement systems", 1984 *Nucl. Fusion* **24**, 851
- [11] A.A. Ware, "Pinch effect for trapped particles in a tokamak", 1970 *Phys. Rev. Lett.* **25**, 916.
- [12] J.W. Connor, H.R. Wilson, "Survey of theories of anomalous transport", 1994 *Plasma Phys. Contr. Fusion* **36** 719-795.
- [13] I. Furno, H. Weisen and TCV team, "Observation of inward and outward particle convection in the core of electron cyclotron heated and current driven plasmas in the TCV", 2003 *Phys. Plasmas* **10**, 2422.
- [14] G.T. Hoang, C. Bourdelle, B. Pégourie, B. Schunke et al. "Particle pinch with fully noninductive Lower Hybrid Current Drive in Tore Supra", 2003 *Phys. Rev. Lett.*, **90**, 155002
- [15] L. Garzotti, X. Garbet, P. Mantica et al. "Particle Transport and Density Profile Analysis of Different JET plasmas", 2003 *Nucl. Fusion* **43**, 1829
- [16] H. Weisen, A. Zabolotsky et al. "Shear and collisionality dependences of particle pinch in JET L-mode plasmas", 2004 *Plasma Phys. Contr. Fusion* **46**, 751-765

- [17] V.V. Yankov “Commentary on Pastukhov’s paper (Sov. J. Plasma Phys., 1980, vol. 6, no. 5, p.549) and the application on the turbulent equipartition approach to the problem of transport in tokamaks” 1995 *Plasma Phys. Rep.* **21** 719
- [18] J. Nycander, V.V. Yankov, “Anomalous pinch flux in tokamaks driven by the longitudinal adiabatic invariant” 1995 *Phys. Plasmas* **2** 2874
- [19] M.B. Isichenko, A.V. Gruzinov, P.H. Diamond and P.N. Yushmanov, “Anomalous pinch effect and energy exchange in tokamaks”, 1996 *Phys. Plasmas* **3** 1916
- [20] C. Angioni, A.G. Peeters et al, “Density peaking, anomalous pinch and collisionality in tokamak plasmas” 2003 *Phys. Rev. Lett.* **90**, 205003
- [21] H. Weisen, A. Zabolotsky et al, “Collisionality and shear dependences of density peaking in JET and extrapolations to ITER” 2005 *Nucl. Fusion* **45** L1-L4
- [22] H. Weisen, A. Zabolotsky, M. Maslov et al. “Scaling of density peaking in JET H-modes and implications for ITER” 2006 *Plasma Phys. Control. Fusion* **48** A457-A466
- [23] C. Angioni et al. “Scaling of density peaking in H-mode plasmas based on a combined database of AUG and JET observations” 2007 *Nucl. Fusion* **47** 1326-1335
- [24] M. Greenwald, C. Angioni et al, “Density profile peaking in low collisionality H-modes: comparison of Alcator C-Mod data to ASDEX Upgrade/JET scalings” 2007 *Nucl. Fusion* **47** L26-L29
- [25] J. Sheffield, “Plasmas scattering of electromagnetic radiation”, 1975 *Academic Press*
- [26] M. Mattioli, R. Papoular, “Analysis of light scattering data from relativistic plasmas”, 1974 *Plasma Physics* Vol. **17** 165-172
- [27] H. Salzmann, K. Hirsch, “Time-of-flight Thomson backscattering technique for large fusion devices”, 1984 *Rev. Sci. Instruments* **55**, 4
- [28] C.W. Gowers et al. “Recent developments in LIDAR Thomson scattering measurements on JET” 1995 *Rev. Sci. Instruments* **66** 471
- [29] G. Braithwaite et al, “JET polari-interferometer”, 1989 *Rev. Sci. Instruments* **60** 2825
- [30] D. O’Brien et al “Equilibrium analysis of iron core tokamaks using a full domain method” 1992 *Nuclear Fusion* **32** 1351
- [31] F. Hofmann, G. Tonetti “Tokamak equilibrium reconstruction using Faraday rotation measurements” 1988 *Nuclear Fusion* **28** 1871
- [32] J. Stoer, R. Bulirsch, “Introduction to numerical analysis” 1980 *Springer, New York*
- [33] A.T. Ramsey, M. Diesso “Abel inversions: Error propagation and inversion reliability” 1999 *Rev. Sci. Instruments* **70**, 380

- [34] I. Furno et al, "A new method for the inversion of interferometry data using basis functions derived from singular value decomposition of local measurements in tokamak plasmas" 2005 *Plasma Phys. Control. Fusion* **47** 49
- [35] M. Anton, H. Weisen, M.J. Dutch et al, "X-ray tomography on the TCV tokamak" 1996, *Plasma Phys. Contr. Fusion* **38** 1849-1878
- [36] A. Zabolotsky, "Particle transport in tokamak plasmas", 2005, École Polytechnique Fédérale de Lausanne, Thèse N3252
- [37] M. Keilhacker, A. Gibson, C. Gormezano, P.H. Rebut, "The scientific success of JET" 2001 *Nuclear Fusion* **41**, No. 12R
- [38] E. Thompson et al, "The use of neutral beam heating to produce high performance fusion plasmas, including the injection of tritium beams in the Joint European Torus (JET)" 1993 *Phys. Fluids* **B5** 2468
- [39] J. Jacquinot et al, "Preliminary ICRF results from JET" 1985 *Plasma Phys. Control. Fusion* **27** 1379-1390
- [40] D.F.H. Start et al, "Bulk ion heating with ICRF in JET DT plasmas" 1999 *Nucl. Fusion* **39**, 321
- [41] F. Durodie et al, "Main design features and challenges of the ITER-like ICRF antenna for JET" 2005 *Fusion Engineering and Design* **74** 223-228
- [42] M. Pain H. Brinkschulte et al, "The 15MW microwave generator and launcher of the lower hybrid current drive experiment on JET" 1989 *Proc. 13th Symp. on Fusion Engineering, Knoxville, Tennessee, USA*
- [43] C.D. Challis, X. Litaudon, G. Tresset et al, "Influence of the q-profile shape on plasma performance in JET", 2002 *Plasma Phys. Control. Fusion* **44** 1031-1055
- [44] R. Pasqualotto, P. Nielsen, M. Beurskens et al, "High resolution Thomson scattering for Joint European Torus (JET)" 2004 *Rev. Sci. Instruments* **75** 3891
- [45] C.C. Hegna "The physics of neoclassical magnetohydrodynamic tearing modes", 1998 *Phys. Plasmas* **5**, 1767-1774
- [46] G. Saibene, R. Sartori, P. de Vries et al, "Toroidal field ripple effects on H-modes in JET and implications fro ITER" 2007, *Proc. Of the 34th EPS Conference on Plasma Physics, Warsaw, Poland*
- [47] M.J. Mantsinen, M.-L. Mayoral et al, "ICRF mode conversion experiments on JET" 2001 *28th EPS Conference on Contr. Fusion and Plasma Phys.* 18-22 June, 2001
- [48] T.H. Stix, "Heating of toroidal plasmas by neutral injection" 1972 *Plasma Physics* **14**, 367-384

- [49] C.D. Challis et al, “Non-inductively driven currents in JET” 1989 *Nuclear Fusion* **29** 563
- [50] R.J. Goldston, D.C. McCune et al, “New techniques for calculating heat and particle source rates due to neutral beam injection in axisymmetric tokamaks” 1981 *J. Comput. Phys.* **43** 61
- [51] V. Mukhovatov, Y. Shimomura, A. Polevoi et al, “Comparison of ITER performance predicted by semi-empirical and theory-based transport models” 2003 *Nucl. Fusion* **43** 942-948
- [52] A.W. Edwards, D.J. Campbell et al, “Rapid collapse of a plasma sawtooth oscillation in the JET tokamak”, 1986 *Phys. Rev. Lett* **57**, 210-213
- [53] H. Zohm, “Edge Localized Modes (ELMs)”, 1996 *Plasma Phys. Control. Fusion* **38**, 105-128
- [54] W. Horton, “Drift waves and transport”, 1999 *Reviews of Modern Physics* **71**, 735
- [55] J.W. Connor, H.R. Wilson, “Survey of theories of anomalous transport”, 1994 *Plasma Phys. Control. Fusion* **36**, 719-795
- [56] S.C. Cowley, R.M. Kulsrud, R. Sudan, “Considerations of ion-temperature-gradient-driven turbulence” 1991 *Phys. Fluids* **B3**(10)
- [57] S.C. Guo, F. Romanelli, “The linear threshold of the ion-temperature-gradient-driven mode”, 1993 *Phys. Fluids* **B5**(2)
- [58] P.J. Catto, W.M. Tang, “Generalized gyrokinetics” 1981 *Plasma Physics* **23**, no.7 pp. 639-650
- [59] A.J. Brizard, T.S. Hahm, “Foundations of nonlinear gyrokinetic theory”, 2007 *Reviews of Modern Physics*, **79** 421-468.
- [60] F. Jenko, W. Dorland “Nonlinear electromagnetic gyrokinetic simulations of tokamak plasmas”, 2001 *Plasma Phys. Control. Fusion* **43** A141-A150
- [61] T.M. Antonsen Jr, B. Lane, “Kinetic equations for low frequency instabilities in inhomogeneous plasmas” 1980 *Phys. Fluids* **23**(6) 1205-1241
- [62] W. Dorland, <http://gs2.sourceforge.net>
- [63] W. Dorland, F. Jenko, M. Kotschenreuther, B.N. Rogers, “Electron temperature gradient driven turbulence“, 2000 *Physical Review Letters* **85** No.26 5579.
- [64] M. Kotschenreuther, G.W. Rewoldt, W.M. Tang, “Comparison of initial value and eigenvalue codes for kinetic toroidal plasma instabilities”, 1995 *Computer Physics Communications*, 88:128

- [65] R.L. Miller, M.S. Chu, J.M. Greene, Y.R. Lin-Liu, R.E. Waltz, "Noncircular, finite aspect ratio, local equilibrium model", 1998 *Phys. Plasmas* **5**, No.4 973-978
- [66] <http://pleiades.epfl.ch>
- [67] R. Gruber et al, "Application-oriented scheduling for HPC Grids", 2007 CoreGRID Technical Report 0070.
- [68] M. Riva, L. Zabeo et al, "Real time safety factor profile determination in JET", 2003 *Fusion Engineering and Design* **66-68**, 779-784
- [69] N.C. Hawkes, K. Blackler, B. Viaccoz et al, "Design of the Joint European Torus motional stark effect diagnostic", 1999 *Rev. Sci. Instruments* **70** 894
- [70] F. Hofmann et al, "Creation and control of variably shaped plasmas in TCV", 1994 *Plasma Phys. Control. Fusion* **36** B277-B287
- [71] H. Weisen et al, "Effect of plasma shape on confinement and MHD behaviour in the TCV tokamak" 1997 *Nuclear Fusion* **37** No.12
- [72] J-M. Moret, F. Hofmann et al, "ECH physics and new operational regimes on TCV", 2002 *Plasma Phys. Control. Fusion* **44** B85-B97
- [73] M.A. Henderson et al. "Recent results from the electron cyclotron heated plasmas in Tokamak à Configuration Variable (TCV)", 2003 *Phys. Plasmas* **10**, 1796
- [74] J.-P. Hogge, S. Alberti, L. Porte, G. Arnoux "Preliminary results of top launch third harmonic X-mode electron cyclotron heating in the TCV tokamak" 2003 *Nucl. Fusion* **43**, 1353-1360
- [75] L. Porte, S.Coda, S. Alberti et al. "Plasma dynamics with second and third-harmonic ECRH and access to quasi-stationary ELM-free H-mode on TCV" 2007 *Nucl. Fusion* **47** 952-960
- [76] A.N. Karpushov, B.P. Duval et al, "Neutral particle analyzer diagnostics on the TCV tokamak", 2006 *Rev. Sci. Instruments* **77**, 033504
- [77] A.N. Karpushov et al, "Upgrade of the diagnostic neutral beam injector for the TCV tokamak", 2003 *Fusion Engineering and Design* **66-68**, 899-904.
- [78] A. Scarabosio, A. Bortolon, B.P. Duval et al, "Toroidal plasma rotation in the TCV tokamak", 2006 *Plasma Phys. Control. Fusion* **48** 663-683
- [79] Ch. Schlatter, B.P. Duval, A.N. Karpushov, "Reconstruction of ion temperature profiles from single chord NPA measurements on the TCV tokamak", 2006 *Plasma Phys. Control. Fusion* **48**, 1765-1785
- [80] F. Ryter et al. "Progress of the international H-mode power threshold database activity", 2002 *Plasma Phys. Control. Fusion* **44** A415-A421

- [81] B. LaBombard, “Manual of Kn1D code”, 2002
- [82] M. Maslov, H. Weisen et al, “Density peaking in TCV and JET H-modes”, oral presentation O3-005 at 33rd EPS conference, Rome 19-23 June 2006
- [83] C. Angioni, A.G. Peeters, X. Garbet et al, “Density response to central electron heating: theoretical investigations and experimental observations in ASDEX Upgrade”, 2004 *Nuclear Fusion* **44** 827-845
- [84] E. Asp, W. Horton et al. “Transport analysis of multi-phase H-mode shot at TCV”, International Sherwood Fusion Theory Conference, 23-25 Apr. 2007, Annapolis, MD, USA
- [85] F. Jenko, T. Dannert, C. Angioni “Heat and particle transport in a tokamak: advances in nonlinear gyrokinetics” 2005 *Plasma Phys. Control. Fusion* **47** B195-B206
- [86] C. Angioni et al, “Collisionality dependence of density peaking in quasilinear gyrokinetic calculations” 2005, *Physics of Plasmas* **12**, 112310
- [87] M. Greenwald, “Density limits in toroidal plasmas” 2002, *Plasma Phys. Control. Fusion* **44** R27-R80
- [88] H. Weisen, C. Angioni, M. Maslov, A. Zabolotsky et al, “Peaked density profiles in low collisionality H-modes in JET, ASDEX Upgrade and TCV”, 21st IAEA Fusion Energy Conference, Chengdu, China 16-20.10.2006
- [89] A.G. Peeters, “The bootstrap current and its consequences” 2000 *Plasma Phys. Control. Fusion* **42** B231-B242
- [90] EFDA, “A conceptual study of commercial fusion power plants”, 2005. Available at www.efda.org
- [91] C. Giroud et al, “Progress in understanding of impurity transport at JET”, 21st IAEA Fusion Energy Conference, Chengdu, China, 16-22.10.2006
- [92] R. Neu et al, “Tungsten: an option for divertor and main chamber plasma facing components in future fusion devices”, 2005 *Nucl. Fusion* **45**, 209-218.
- [93] A. Zabolotsky, H. Weisen, A. Karpushov, TCV Team and JET EFDA contributors, “Influence of particle sources on electron density peaking in TCV and JET”, 2006 *Nucl. Fusion* **46**, 594-607.
- [94] C. Angioni, O. Sauter, “Neoclassical transport coefficients for general axisymmetric equilibria in the banana regime”, 2000 *Phys. Plasmas* **7(4)**, 1224-1234
- [95] O. Sauter, C. Angioni, Y.R. Lin-Liu, “Neoclassical conductivity and bootstrap current formulas for general axisymmetric equilibria and arbitrary collisionality regime”
- [96] X. Garbet, P. Mantica et al. “Physics of transport in tokamaks”, 2004 *Plasma Phys. Control. Fusion*, **46** B557-B574

- [97] R. E. Waltz et al., “A gyro-Landau-fluid transport model“, 1997, *Phys. Plasmas* **2**, 2408
- [98] G. W. Hammett and F. W. Perkins, “Fluid moment models for Landau damping with application to the ion-temperature-gradient instability”, 1990, *Phys. Rev. Lett.* **64** 3019-3022

Acknowledgements

First of all, I would like to thank my thesis director Dr. Henri Weisen for the superb guidance through the labyrinths of plasma science and the enormous amount of help and support during the whole period of this thesis work.

I am very grateful to the CRPP directors: Prof. M.Q. Tran, Prof. A. Fasoli, Dr. K. Appert for giving me an opportunity to work here and making this PhD project possible.

A sincere acknowledgement to the CRPP scientific staff: O. Sauter, R. Behn, A. Pochelon, L. Villard, J.-M. Moret, S. Alberti, S. Coda and many others, who all have contributed to this work in one way or another. I would like to regard separately the CRPP secretary staff for their help in crawling through numerous administrative procedures.

I would like to give a special respect to Dr. Clemente Angioni for his tremendous help in plasma theory scope and GS2 code usage. Without him this thesis work would no be possible.

I'm very grateful to the JET staff and the Associate Leader Dr. F. Romanelli for letting me to stay there for a few very exciting months. The Tank Force Transport group, led by P. Mantica, T. Tala, N. Volker for their support in theoretical side of this work. The Task Force Diagnostics, led by A. Murari, and the Electron Kinetic Group, especially its leader M. Walsh and the LIDAR Responsible Officer M. Beurskens for the great expertise in plasma diagnostics, especially the density measurements.

Finally, I would like to cheer all my friends and my family for supporting me during the doctoral studies. Thank You!

Curriculum vitae

NAME: Mikhail Maslov

DATE OF BIRTH: 18.10.1979

PLACE OF BIRTH: Volgodonsk, Russia.

EDUCATION:

1986-1996 Primary and secondary school, Volgodonsk, Russia

September 1996-
July 2000 Moscow Institute of Physics and Technology,
Russia
Bachelor in applied mathematics and physics.

September 2000-
July 2002 Moscow Institute of Physics and Technology,
Russia
Master in applied mathematics and physics.

July 2002 -
November 2004 Nuclear Fusion Institute, RRC « Kurchatov
Institute »
Engineer, PhD student

November 2004-present Centre de Recherches en Physique des Plasmas
Ecole Polytechnique Fédérale de Lausanne,
Switzerland
Assistant-doctorant

Publications :

M. Maslov, K. Razumova, A.J.H. Donne et al,
“Reduced plasma transport in the core of T-10 and TEXTOR plasmas after off-axis ECRH
switch-off”
EC-13 joint workshop on electron cyclotron emission and electron cyclotron resonance
heating, Nijniy Novgorod, May 2004.

H. Weisen, A Zabolotsky, **M Maslov** et al
“Scaling of density peaking in JET H-modes and implications for ITER”
2006 *Plasma Phys. Control. Fusion* **48** A457-66

M. Maslov, H. Weisen, A. Zabolotsky, L. Porte, C. Angioni, M. Beurskens, TCV team and
JET-EFDA contributors,
“Density peaking in TCV and JET H-modes”, oral at “33rd European Physical society
Conference on Plasma”, 19-23 June 2006, Rome, Italy.

M. Maslov, H. Weisen, C. Angioni et al. “Density profile behavior on JET and extrapolations to ITER”, poster at 49th Annual Meeting of the Division of Plasma Physics (DPP), Orlando, USA 12-16 Nov 2007.

M. Maslov, H. Weisen. C. Angioni et al. “Density profile behavior in JET H-mode plasmas”, EX/P5-20, IAEA FEC-2008, Geneva.

M. Maslov, H. Weisen. C. Angioni et al. “Density profile behavior in JET H-mode plasmas: experiments versus linear gyrokinetic predictions”, 2009, Nuclear Fusion.